FLUORESCENCE OPTOFLUIDIC MICROSCOPY AND FLUORESCENCE MICROSCOPY BASED ON THE TALBOT EFFECT

Thesis by
Shuo Pang

In Partial Fulfillment of the Requirements for the Degree
of
Doctor of Philosophy

CALIFORNIA INSTITUTE OF TECHNOLOGY
Pasadena, California
2013
(Defended April 2, 2013)

ACKNOWLEDGEMENTS

First of all, I would like to express my gratitude to my advisor, Professor Changhuei Yang. His passion for research inspired me throughout my PhD study. He can always come up with very innovative ideas and his research vision is unique. I am not sure if creativity is something that can be learned, yet Dr. Yang's enthusiasm for research is contagious. From him I also learned to treat the problem solving as the part of the fun in research. Dr. Yang is also one of the most encouraging professors I have met. The resource of the lab is great and Dr. Yang gave us the freedom and support for us to develop our own ideas.

I would like to express my thanks to Professor Paul W. Sternberg. I have always been amazed by the depth and broadness of his knowledge. I am also very inspired by his optimistic attitude towards research. Whenever I interacted with him, he was always engaged in the conversation and provided me excellent advice and generous help. His lab members have been of immense help to our research.

I would also like to thank Professor Yu-Chong Tai, Professor Azita Emami-Neyestanak, and Professor Hyuck Choo for being my thesis committee and my candidacy committee, and providing me their valuable suggestions. They are the amazing professors whom I admire.

I have enjoyed working in the diligent and creative group of Biophotonics at Caltech, including Dr. Xiquan Cui, Dr. Jigang Wu, Dr. Lap Man Lee, Dr. Jian Ren, Dr. Guoan Zheng, Ying Min Wang, Dr. Benjamin Judkewitz, Seung Ah Lee, Mooseok Jang, Xiaoze Ou, Roarke Horstmeyer, and Haojiang Zhou. Dr. Xiquan Cui was the first graduate student I worked with in the group, he helped me to quickly become involved in the lab when I first came to Caltech. On the Opto-fluidic Microscope projects I worked closely with Dr. Lap Man Lee, Chao Han, Dr. Guoan Zheng, and Seung Ah Lee. I am grateful for their knowledge in optics and microfluidics and their generous help and discussions.

I would like to specially thank Chao Han, my close teammate for Fluorescence OFM and Fluorescence Talbot Microscope projects. Though we graduated from the same undergraduate program, our research background is quite different. I learned biology from him and hopefully he has benefitted from our discussion in optics. I enjoyed working with him for the last three years.

Thanks to our collaborators especially from Professor Sternberg's lab and Professor Fraser's lab. John Demodena taught me how to grow and maintain the *C. elegans* strain. I would like to specially thank Dr. Mihoko Kato, who helped us with sample preparations for the Talbot microscope projects. I would also like to thank Danielle Brown from Professor Fraser's lab. She helped us with infecting multiple cell lines and with debugging the problems with fluorescence antibody labeling.

I would also like to express my thanks to Anne Sullivan, our awesome lab manager. She takes care of every detail from ordering lab equipment to arranging our conference travels. Because of her, the lab feels like a home to me.

I was very fortunate to have a group of friends in Pasadena, who helped me grow as a person and were willing to share their own experience to provide me guidance in many aspects of life. Morgan Putnam, Thomas Clement, Alan Chapman, Ernst Jan Vesseur, Erin Burkett, Andrea Rentmeister, Markus Hauschild, Scott Chaney, Nicole Czakon, Andrew Darcy, Ricardo Bermejo de Val, Evelyn Stuwe, and of course the members of the biophotonics group.

Finally I would like to thank my family, especially my father and mother. I can always feel their tremendous support during my years in graduate school. Their patience and unconditional love give me the courage and determination to pursue goals that seemed "unreasonable" or even "impossible".

ABSTRACT

Light microscopy has been one of the most common tools in biological research, because of its high resolution and non-invasive nature of the light. Due to its high sensitivity and specificity, fluorescence is one of the most important readout modes of light microscopy. This thesis presents two new fluorescence microscopic imaging techniques: fluorescence optofluidic microscopy and fluorescent Talbot microscopy. The designs of the two systems are fundamentally different from conventional microscopy, which makes compact and portable devices possible. The components of the devices are suitable for mass-production, making the microscopic imaging system more affordable for biological research and clinical diagnostics.

Fluorescence optofluidic microscopy (FOFM) is capable of imaging fluorescent samples in fluid media. The FOFM employs an array of Fresnel zone plates (FZP) to generate an array of focused light spots within a microfluidic channel. As a sample flows through the channel and across the array of focused light spots, a filter-coated CMOS sensor collects the fluorescence emissions. The collected data can then be processed to render a fluorescence microscopic image. The resolution, which is determined by the focused light spot size, is experimentally measured to be 0.65 μm.

Fluorescence Talbot microscopy (FTM) is a fluorescence chip-scale microscopy technique that enables large field-of-view (FOV) and high-resolution imaging. The FTM method utilizes the Talbot effect to project a grid of focused excitation light spots onto the sample. The sample is placed on a filter-coated CMOS sensor chip. The fluorescence emissions associated with each focal spot are collected by the sensor chip and are composed into a sparsely sampled fluorescence image. By raster scanning the Talbot focal spot grid across the sample and collecting a sequence of sparse images, a filled-in high-resolution fluorescence image can be reconstructed. In contrast to a conventional microscope, a collection efficiency, resolution, and FOV are not tied to each other for this technique. The FOV of FTM is directly scalable. Our FTM prototype has demonstrated a resolution of 1.2 μm, and the collection efficiency equivalent to a conventional microscope objective with a 0.70 N.A. The FOV is 3.9×3.5 mm^2, which is 100 times larger than that of a 20X/0.40 N.A. conventional microscope objective. Due to its large FOV, high collection efficiency, compactness, and its potential for integration with other on-chip devices, FTM is suitable for diverse applications, such as point-of-care diagnostics, large-scale functional screens, and long-term automated imaging.

TABLE OF CONTENTS

LIST OF ILLUSTRATIONS AND/OR TABLES

Page

LIST OF FREQUENTLY USED ACRONYMS

Acronym	**Full name**
Al	Aluminium
C. elegans	*Caenorhabditis elegans*
CMOS	Complementary metal–oxide–semiconductor
CPT	Camptothecin
DTC	Distal tip cell
EFL	Effective focal length
FIB	Focused ion beam
FOV	Field of view
FOFM	Fluorescence optofluidic microscope
FTM	Fluorescence Talbot microscope
FWHM	Full-width at half maximum
FZP	Fresnel zone plate
HEK293 cell	Human embryonic kidney 293 cell
HER2	Human epidermal growth factor receptor-2
N.A.	Numerical aperture
OD	Optical density
OFM	Optofluicid microscope
PSF	Point spread function

C h a p t e r 1

INTRODUCTION

Due to its high resolution and the non-invasive nature of optical wavelength, optical microscopy has been one of the most significant tools in biology research since its invention in the late 16th century. On one hand various new microscopy techniques have been invented, leading to new discoveries in biology; on the other hand, as a rapidly evolving quest, biology research continuously requires microscopes with higher performance, better contrast, and even new imaging methods. Current microscopy technique has been constantly challenged by new findings in neuroscience, system biology, development biology, and point-of-care diagnosis. Not only is it an exciting time for biologist and clinicians who use microscopes as an imaging tool, it is a thrilling time for engineers, applied physicists, and chemists who work on microscopy development as well.

This chapter is the introduction to the thesis. In the beginning, we will first review the image formation principle and basic concept in a conventional optical microscope. Then we will discuss some of novel microscopy techniques enabling better resolution and higher contrast. Next, we will focus the discussion on chip-scale microscopy. Chip-scale microscopes have been designed with the aim of producing portable and mass-producible imaging devices. In the final section of the chapter, we will define the scope of this thesis and outline the structure.

1.1 Conventional microscope

Though Robert Hooke and Antonie van Leeuwenhoek are usually credited for the invention of the microscope and the observation of the microscopic biological structures, the origin of the microscope can be dated back to 1595. Mentioned in the letters by the Dutch ambassador William Borel, the inventors of the first microscope are Hans Jansen, a Dutch spectacle-maker, and his son Zacharias. The microscope they invented consists of two lenses inside a tube. The magnification can be adjusted by changing the distance between the lenses. This design is not much different from the microscope that most biology labs use today. In this section we will talk about the principles of conventional light microscope and discuss some key improvements in microscope performance.

1.1.1 Imaging principle of the conventional microscope

In the conventional microscope, one or more refractive lenses form an optical system, which can direct the light from the object to form a magnified image. The central part of the microscope is its objective. The objective forms the magnified real image. Figure 1.1(b) shows microcope imaging geometry with a finite optical system. The objective is attached to a body tube and then connected to a light detector such as camera film or imaging sensor at the image plane. If we would like to observe the sample with our eyes, the light detector built by Mother Nature, a pair of eyepieces is attached to the end of the body tube to form a virtual image. The microscope design has essentially remained the same since the early days of Robert Hooke [1].

Over the past decade, the major microscope manufacturers have largely migrated to infinite optical systems, as shown in Figure 1.1 (a). In infinite optical systems, the object is placed at the front focal plane of the objective, so the image distance is set to infinity, and a tube lens is placed within the body tube to produce the intermediate image [2].

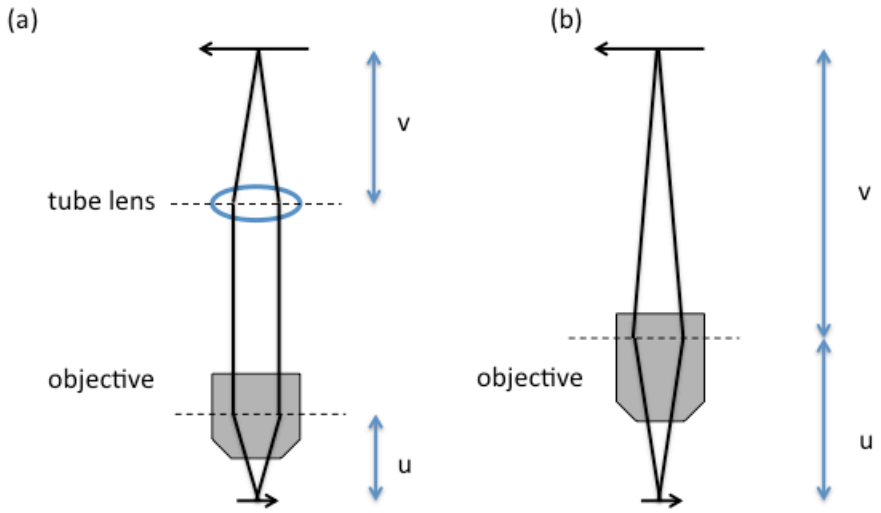

Figure 1.1. The basic setup for conventional microscopes. (a) The setup for a microscope with infinite optical system. (b) The setup for a microscope with finite optical system

In both infinite and finite optical system, the magnification, *M*, is determined by the ratio between the object distance and the image distance,

$$M = \frac{u}{v}, \tag{1.1}$$

where u is the object distance, and v is the image distance. In the finite optical system, the object distance is defined as the distance between the object and the front principle plane of the objective, and the image distance is defined as the distance between the image and the back principle plane of the objective. In the infinite optical system, the object distance has the same definition as that of the finite system, while the image distance is the distance between the image and the back principle plane of the tube lens. As the object is placed in the front focal plane of the objective, and the image is formed on the back focal plane of the tube lens, the magnification of the infinite system is the ratio of the effective focal length (EFL) of the tube lens and the EFL of the objective. For example, an infinite corrected microscope objective manufactured by Nikon has an EFL of 10 mm. The EFL of a tube lens is 200 mm. Then the magnification is 200mm/10mm = 20. From these numbers we can see that the whole optical path length is on the order of tens of centimeters. This determines the size of the microscope body. In practice, an objective lens requires sophisticated design to correct for optical aberrations, and precise adjustments are needed during the assembly process. This is the reason why microscope systems are complicated and expensive.

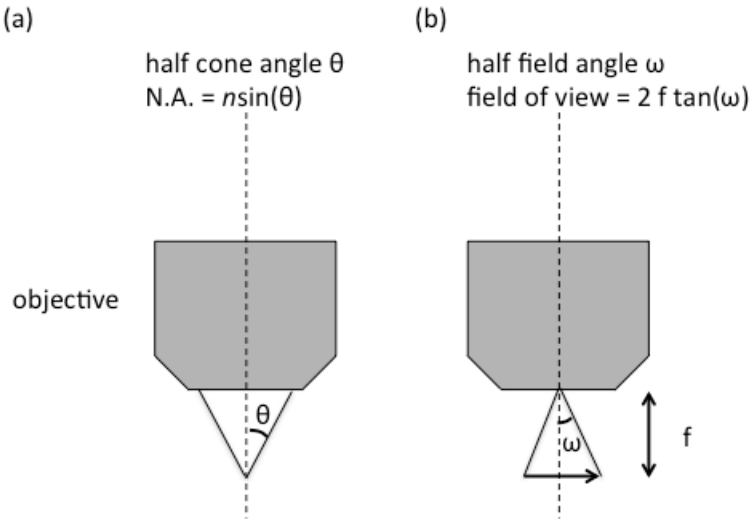

Figure 1.2. Illustration of numerical aperture and field of view of a microscope objective

The amount of light that can be collected by a microscope objective is limited by its physical diameter. The microscope can only accept information carried by light within a certain collection cone, and the collection range is described by the half cone angle θ. In microscopy, numerical aperture (N.A.) is more common in quantify is angle. The N.A. is defined by

$$N.A. = n\sin\theta \,, \tag{1.2}$$

where n is the refractive index of the imaging medium. The N.A. of a conventional microscope usually ranges from 0.05 to 1.3. Another important angle is the half field angle, ω, which describe the field of view (FOV) of the microscope objective. The relation between ω and the FOV is described as

$$FOV = 2f\tan\omega \,, \tag{1.3}$$

where f is the EFL of the microscope objective. The half field angle of the objective is usually about 0-3°. The EFL of microscope objective is usually in the millimeter range. The common FOV of the microscope is no greater than 1 mm.

1.1.2 Improvements in resolution and contrast through novel microscopy techniques

In this section, we will discuss the resolution limits and the contrast mechanism of the conventional microscope. In recent years, the resolution and contrast has been greatly improved by new microscopy techniques. We will also briefly review some of these key improvements.

Resolution

In an aberration-free microscope system, the optical resolution is only limited by the diffraction. Based on Abbe's equation [3], the diffraction-limited resolution, r, of a microscope is determined by,

$$r = \frac{0.61\lambda}{N.A.} \,, \tag{1.4}$$

where *r* is defined as the smallest resolvable distance between two objects. We can see that the resolution of the microscope is limited by the N.A. of the objective, and the wavelength. For

example, for a microscope objective with 20X magnification, 0.4 N.A., the sample is illuminated with 488 nm blue light. The diffraction-limited resolution is 0.74 μm.

Recently, many optical microscopy methods have been developed to to break this diffraction limit. One of the early attempts was near field optical scanning microscopy (NSOM) [4, 5]. Recent super resolution microscopy methods aim to achieve higher resolution in the far field.

Structured illumination microscopy (SIM) [6] and 4Pi microscopy consider this diffraction limit in the spatial frequency space [7]. By using interference illumination, the two methods effectively increase the detectable frequency range in both lateral and axial directions. The lateral resolution can be doubled, and the axial resolution can be improved ~5 times.

Photo-activated localization microscopy (PALM) [8] and stochastic optical reconstruction microscopy (STORM) [9] take advantage of the photo-switchable fluorophores to selectively switch on individual fluorescent molecules and estimate the location of the molecule. The precision of the location estimation is much higher than the diffraction-limited resolution. By building a map of the locations of single emitters, a super-resolution image can be acquired. Stimulated emission depletion (STED) microscopy [10] introduces a depletion beam that controls the fluorescence emission and can create a scanning point smaller than the diffraction-limited focus.

These super resolution microscope methods allow sub 100 nanometer resolution, while still maintaining the non-invasive nature of optical imaging.

Contrast

In bright field microscopy imaging, the scattering of the sample structure causes the variation of the light intensity. The sample fixed on the microscope slide is usually between10 to 100 μm in thickness. The light scattering is usually stronger than the light absorbed by the sample. Yet the contrast introduced by absorption was observed as early as 17th century, when Robert Hooke described the light microscopic appearance of a stained object, in the form of dyed wool and hair [1]. Many color stains were developed to provide more contrast for different biological structures. About color staining, we will have more detailed discussion in Chapter 2.

In 1930, when Dutch Nobel laureate Frits Zernike studied optics of diffraction gratings, he realized that the direct light and the diffracted light were actually in different phases [11]. This discovery eventually led to phase contrast microscopy. Based on the same idea, differential interference contrast (DIC), has now become one of the common readout modes for the biological microscope.

Fluorescence readout is becoming one of the most significant modalities of the optical microscope, because of the sensitivity and specificity of the fluorescence molecular probe. Fluorescence is the emission of light by a fluorescence molecule that has absorbed the light of a different wavelength. In most cases, the emission has a longer wavelength than the absorbed light. Fluorescence imaging has various applications. To name a few examples: fluorescent probes against cancer markers are used for cancer diagnosis [12]; encoded fluorescent proteins enable minimally-invasive observation of gene expressions[13]; fluorophores can serve as indicators to visualize excitable cell firing and calcium transients for functional studies in neurons [14].

Furthermore, many of the super resolution techniques mentioned above require contrast from engineered fluorophores. Multi-photon absorption/emission has also led to the invention of multi-photon microscopy, which has opened a wide range of applications in deep tissue imaging [15].

Other than fluorescence, non-linear microscopy can image non-labeled samples. For example, second harmonic generation (SHG) microscopy can image the contrast provided by structures that support SHG. Stimulated Raman scattering (SRS) microscopy [16] and coherent anti-Stokes Raman spectroscopy (CARS) microscopy can image the contrast provided by vibrational frequency signatures of molecules.

1.2 Chip-scale microscope

In the previous sections we have introduced conventional microscopy and some novel microscopy techniques that improve resolution, contrast, and imaging depth. In this section we will focus on improving the microscope in another direction: bringing down the cost of the microscope.

The conventional microscope is usually expensive and bulky because of the complicated design of the microscope objective. Despite the long history of microscopy and the new imaging techniques that have been developed since its invention, the fundamental design of microscopes has undergone little change. To reduce the cost of the system, this fundamental design needs to be changed.

For the past 10 years, the majority of cell phones have come equipped with a camera. The cost of the CMOS imaging sensor in cellphones is often less than $5. The invention of a mass-producible microscope will have the great potential not only to reduce the cost, but also to lead to the miniaturization of the microscope. The first on-chip microscope, the optofluidic microscope (OFM), was developed in our lab [17].

1.2.1 Optofluidic microscope

OFM exploits the time dimension during the image acquisition process. In the basic OFM setup one can imagine covering the sensor with a thin metal layer and etching a small aperture array onto the layer at the center of each sensor pixel.

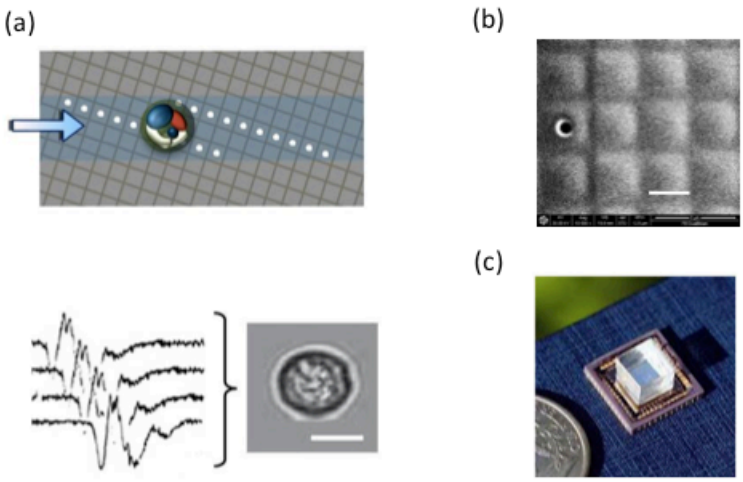

Figure 1.3. Optofluidic microscope (OFM) device. (a) Imaging principle of OFM. The scale bar on the sample is 10 μm. (b) Focused ion beam image of an aperture fabricated on a CMOS sensor chip. The scale bar is 3 μm. (c) Photograph of the OFM prototype.

The aperture array is tilted at a small angle with respect to x axis, and the sample is linearly translated in a microfluidic channel. Figure 1.3 (a) shows this imagining setup. As long as a sufficient number of apertures span across the specimen completely in the y axis, and the neighboring apertures overlap sufficiently along the y axis, a filled-in high-resolution image of the specimen will be achieved [17].

The resolution of an OFM is fundamentally determined by the aperture size and not the pixel size. Therefore, by choosing the appropriate aperture size, we can achieve high resolution. Figure 1.3 (b) shows the focused ion beam (FIB) image of an aperture defined on an imaging sensor coated with a 300 nm thick Al layer. Figure 1.3 (c) shows a prototype of the OFM.

Along the lines of the OFM imaging method, our group further developed other OFM models including Color OFM [18], Super-resolved OFM (SROFM) [19], and Fluorescence OFM [20].

1.2.2 Other chip-scale microscopes

Hologram microscopes are the base technology of one other family of on-chip microscopes. Nobel laureate Dennis Gabor first suggested this microscopic imaging concept with in-line holography [21]. Since the implementation of this method with an imaging sensor, the hologram-based chip-scale microscope has led to many biological applications [22, 23]. Compared with OFM methods, the hologram microscope has a large FOV and provides phase information from the sample. However, this method requires partially coherent light, and thus cannot be applied in fluorescence imaging. In addition, its phase retrieval algorithm has the assumption of sample sparcity, so it is not suitable for imaging cell cultures with high confluency.

1.3 Organization of the thesis

The major concentration of this thesis is on the development of the chip-scale fluorescence microscopic imaging platform. Two major devices were developed during my graduate study: the fluorescence OFM and fluorescence Talbot microscope (FTM) [24]. The former works along the lines of OFM method. FTM is a new imaging method that enables high resolution, large FOV imaging. Figure 1.4 shows an FTM prototype and an image acquired by FTM.

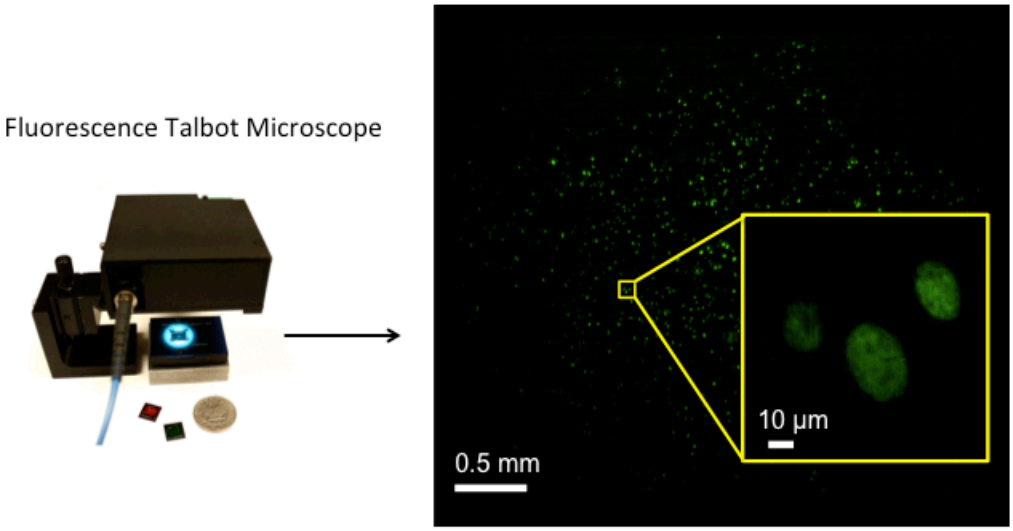

Figure 1.4. The fluorescence Talbot microscope (FTM) prototype and a large field of view image acquired by the prototype.

In Chapter 2, we will describe the implementation of a color-capable on-chip system using OFM method, termed color OFM. In Chapter 3, we will describe the fluorescence OFM and its application in cell imaging. From Chapter 4 to Chapter 8, we will focus on the FTM method. In Chapter 4 we will discuss the imaging principle and an implementation of a FTM prototype. The characterization of the on-chip FTM prototype will be described in Chapter 5, and in Chapter 6 we will report the multi-color FTM using an optical relay system. In Chapter 7 we will report two biological applications using the on-chip FTM prototype. Chapter 8 will discuss the potentials and the outlook of the FTM method.

REFERENCES

1. R. Hooke, *Micrographia or Some Physiological Descriptions of Minute Bodies* (Cosimo Classics, 2007).
2. "Nikon MicroscopeU – Infinity Optical Systems," http://www.microscopyu.com/articles/optics/cfintro.html.
3. E. Abbe, "Beiträge zur Theorie des Mikroskops und der mikroskopischen Wahrnehmung," *Archiv für mikroskopische Anatomie* **9**, 413-418 (1873).
4. U. Durig, D. W. Pohl, and F. Rohner, "Near-field optical-scanning microscopy," *Journal of Applied Physics* **59**, 3318-3327 (1986).
5. E. Betzig, and R. J. Chichester, "Single molecules observed by near-field scanning optical microscopy," *Science* **262**, 1422-1425 (1993).
6. M. G. L. Gustafsson, "Surpassing the lateral resolution limit by a factor of two using structured illumination microscopy," *Journal of Microscope* **198**, 82-87 (2000).
7. S. W. Hell, S. Lindek, C. Cremer, and E. H. K. Stelzer, "Measurement of the 4pi-confocal point-spread function proves 75 nm axial resolution," *Applied Physics Letters* **64**, 1335-1337 (1994).
8. E. Betzig, G. H. Patterson, R. Sougrat, O. W. Lindwasser, S. Olenych, J. S. Bonifacino, M. W. Davidson, J. Lippincott-Schwartz, and H. F. Hess, "Imaging intracellular fluorescent proteins at nanometer resolution," *Science* **313**, 1642-1645 (2006).
9. M. J. Rust, M. Bates, and X. W. Zhuang, "Sub-diffraction-limit imaging by stochastic optical reconstruction microscopy (STORM)," *Nature Methods* **3**, 793-795 (2006).
10. K. I. Willig, S. O. Rizzoli, V. Westphal, R. Jahn, and S. W. Hell, "STED microscopy reveals that synaptotagmin remains clustered after synaptic vesicle exocytosis," *Nature* **440**, 935-939 (2006).
11. F. Zernike, "Phase contrast, a new method for the microsopic observation of transparent objects," *Physica* **9**, 686-698 (1942).
12. D. J. Brennan, D. P. O'Connor, E. Rexhepaj, F. Ponten, and W. M. Gallagher, "Antibody-based proteomics: fast-tracking molecular diagnostics in oncology," *Nature Reviews Cancer* **10**, 605-617 (2010).
13. R. Y. Tsien, L. Ernst, and A. Waggoner, "Fluorophores for confocal microscopy: photophysics and photochemistry," *Handbook of biological confocal microscopy*, 338-352 (2006).
14. R. Kerr, V. Lev-Ram, G. Baird, P. Vincent, R. Y. Tsien, and W. R. Schafer, "Optical imaging of calcium transients in neurons and pharyngeal muscle of *C. elegans*," *Neuron* **26**, 583-594 (2000).
15. W. Denk, J. H. Strickler, and W. W. Webb, "Two-photon laser scanning fluorescence microscopy," *Science* **248**, 73 (1990).
16. C. W. Freudiger, W. Min, B. G. Saar, S. Lu, G. R. Holtom, C. W. He, J. C. Tsai, J. X. Kang, and X. S. Xie, "Label-free biomedical imaging with high sensitivity by stimulated Raman scattering microscopy," *Science* **322**, 1857-1861 (2008).
17. X. Cui, L. M. Lee, X. Heng, W. Zhong, P. W. Sternberg, D. Psaltis, and C. Yang, "Lensless high-resolution on-chip optofluidic microscopes for *Caenorhabditis elegans* and cell imaging," *Proceedings of the National Academy of Sciences* **105**, 10670 (2008).
18. S. Pang, X. Cui, J. DeModena, Y. M. Wang, P. Sternbergc, and C. Yang, "Implementation of a color-capable optofluidic microscope on a RGB CMOS color sensor chip substrate," *Lab on a Chip* **10**, 411-414 (2010).

19. G. Zheng, S. A. Lee, S. Yang, and C. Yang, "Sub-pixel resolving optofluidic microscope for on-chip cell imaging," *Lab on a Chip* **10**, 3125-3129 (2010).
20. S. Pang, C. Han, L. M. Lee, and C. H. Yang, "Fluorescence microscopy imaging with a Fresnel zone plate array based optofluidic microscope," *Lab on a Chip* **11**, 3698-3702 (2011).
21. D. Gabor, "A New Microscopic Principle," *Nature* **161**, 777-778 (1948).
22. A. Ozcan, and U. Demirci, "Ultra wide-field lens-free monitoring of cells on-chip," *Lab on a Chip* **8**, 98-106 (2008).
23. W. Bishara, T.-W. Su, A. F. Coskun, and A. Ozcan, "Lensfree on-chip microscopy over a wide field-of-view using pixel super-resolution," *Optics Express* **18**, 11181-11191 (2010).
24. S. Pang, C. Han, M. Kato, P. W. Sternberg, and C. Yang, "Wide and scalable field-of-view Talbot-grid-based fluorescence microscopy," *Optics Letters* **37**, 5018-5020 (2012).

C h a p t e r 2

COLOR OPTOFLUIDIC MICROSCOPE

In the previous chapter we have briefly reviewed some new effort in redesigning the microscope for low-cost and compact devices. In this chapter, we describe the implementation of a color-capable on-chip lensless microscope system, termed color optofluidic microscope (color OFM), and demonstrate imaging of double stained *Caenorhabditis elegans* (*C. elegans*) with lacZ gene expression. This chapter is adapted from S. Pang, X. Cui, J. DeModena, Y. M. Wang, P. W. Sternberg, and C. Yang, "Implementation of a color-capable optofluidic microscope on a RGB CMOS color sensor chip substrate", *Lab on a Chip* **10**, 411-414 (2010).

2.1 Introduction

The development of microscopes that are autonomous, compact, low-cost and high-resolution can improve existing microscopy applications in point-of-care diagnostics, and potentially engender new microscope usage. The lensless and fully on-chip microscope systems, termed the optofluidic microscopes (OFM), as briefly reviewed in the last chapter, can potentially fill this role. [1, 2]

Cell color staining is a common technique for better visualization of tissue or cells in bright field microscopy. By using different stains, one can preferentially stain specific cell components. Color staining is useful for the observation of particular metabolic processes or the differentiation between live and dead cells. Some examples of commonly used color stains are: hematoxylin, a nuclear stain that stains nuclei blue-violet; iodine, a starch indicator; Trypan blue, a vital stain that selectively colors dead tissues or cells; and nile red, which stains intracellular lipid globules red.

The capability to image a color sample using OFM will enrich more applications for on-chip imaging. In this Chapter, we present an OFM system that is capable of performing color imaging. This system uses a color CMOS sensor chip in place of a monochromatic CMOS sensor chip in the standard OFM, and employs an aperture array arrangement that accommodates the Bayer color pixel arrangement on such sensors.

In this chapter, we will first describe the specifications and operating principle of our color OFM prototype. Next, we will report on the calibration of our prototype and its use in measuring the

concentration of a dye, Trypan Blue, under varying illumination intensity. Finally, we will show color OFM images of the microscopic nematode *C. elegans* expressing β-galactosidase with a blue LacZ stain, and Ponceau, a nonspecific red stain.

2.2 Imaging principles of color OFM

As briefly mentioned in Chapter 1, OFM method utilizes microfluidic flow to transport samples across one or more arrays of small apertures (1 micron or smaller) on a metal-coated CMOS imaging sensor that is illuminated with light. The passage of a sample interrupts light transmission through the apertures, and the time-varying transmission associated with each aperture effectively represents a line trace across the sample.

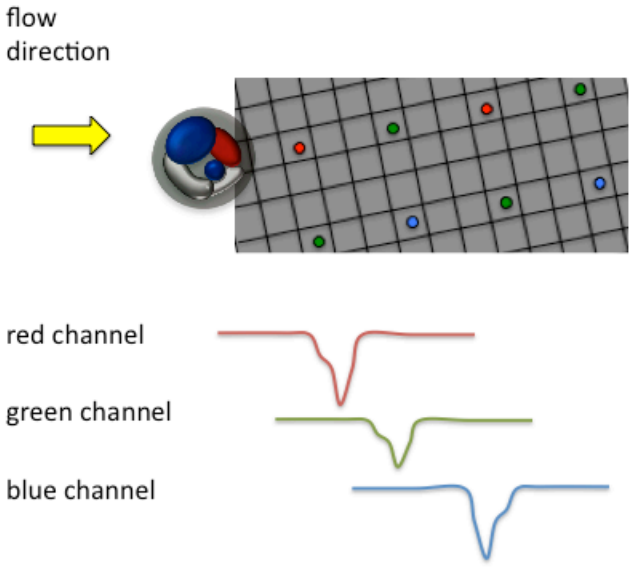

Figure 2.1. Imaging principle of the color OFM based on a color imaging sensor. Each aperture corresponds to a color channel.

By appropriately compositing these line traces from these apertures, we can then generate a high-resolution image of the sample at a resolution comparable to the aperture size. The diagonal arrangement of the aperture array across the channel floor allows the aperture arrays to fully scan a sample flowing in the channel.

The color OFM is based on the same imaging principle. Instead of using a monochromatic imaging sensor, a color sensor is employed. The small apertures are opened on pixels representing red,

green, and blue channels. Figure 2.1 shows the schematic plots of the color OFM. So instead of collecting the signal from one line of aperture array, two aperture arrays collect the light from the three different color channels. A RGB image can be acquired by combining the color channels together.

The absence of lenses and other bulk optical elements in the OFM design is particularly advantageous as it allows us to implement highly compact chip-scale microscope systems that are mass-producible in a semiconductor foundry. In addition, as the OFM can directly process samples in fluid media, this method eliminates the need to prepare fluid samples onto a glass slide for standard microscopy examination. The basic OFM design can be altered to provide additional imaging capability.

2.3 Color OFM device fabrication

The color OFM prototype was fabricated on a color CMOS sensor substrate; the sensor (Aptina, MT9T001P12STC) consists of 2048 × 1536 pixels of size 3.2 μm. Each of these pixels is coated with one of three different chromatic filters that nominally transmit the red (R), green (G) or blue (B) region of the optical spectrum. The color pixels are arranged in a two by two Bayer pattern consisting of two diagonal green pixels, one red pixel and one blue pixel as shown in Figure 2.2(a).

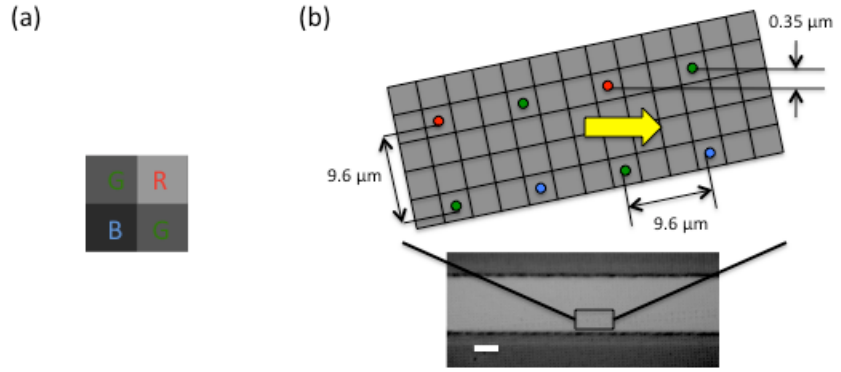

Figure 2.2. The aperture arrangement for a color CMOS imaging sensor. (a) The Bayer pattern for the color filter mask of the CMOS sensor. (b) The schematic plot for the aperture array and the microscope image of the aligned PDMS channel on top of the aperture array. The scale bar is 20 microns.

We spin-coated a polymethyl methacrylate (PMMA) layer of 300 nm in thickness to planarize the sensor's surface.

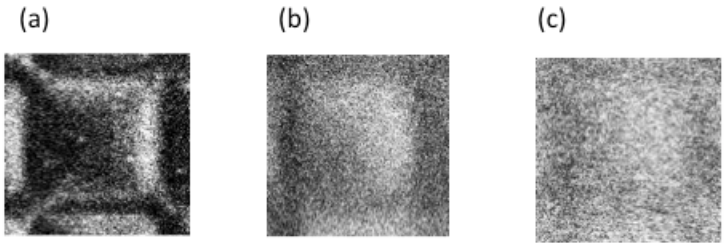

Figure 2.3. Focused ion beam (FIB) image of the sensor pixels coated with aluminum of different planarization layer thicknesses. (a) No PMMA. (b) 300 nm PMMA. (c) 600 nm PMMA.

We next used a metal evaporator with thermal source (CHA Industries, Mark 40) to deposit a 300 nm thick aluminum layer on top of the PMMA layer. By choosing the correct photoresist thickness (300 nm), we were able to discern the pixel reliefs on the chip. Figure 2.3 shows the CMOS sensor pixel with different PMMA thicknesses. At 300 nm thicknesses, the outlines of individual pixels were still discernible under SEM imaging and the surface was sufficiently flat to allow subsequent bonding of a PDMS block containing a microfluidic channel onto the chip. We then used a focused ion beam (FIB) machine (FEI Company, Nova200) to mill two arrays of 140 apertures on the aluminum layer. Then another 200 nm PMMA layer was spin coated on the aluminum layer to protect the aperture. The diameter of the aperture was 0.7 μm. The apertures were spaced 9.6 μm apart (equal to 3-pixel pitch). The two arrays were also spaced 9.6 μm apart. The relatively wide spacing choice was made to minimize crosstalk effects from neighboring pixels. We took care to ensure that the apertures were each milled directly above a single sensor pixel by exercising a good control over the milling process. The apertures of the first and second array were patterned over the color pixels in repeating sequence of –RG- and –GB- respectively. Figure 2.2 (b) shows the aperture arrangement for the color OFM device.

Finally, we attached a polydimethylsiloxane (PDMS) block containing a soft-lithography patterned microfluidic channel onto the sensor with a mask aligner (Karl Suss, MJB3). The channel was 40 μm in width and 20 μm in height. The channel was set at an angle of 0.05 radians to the aperture array. This ensured that apertures associated with the same color overlapped each other by 0.7 μm

across the width of the channel. The cross-section view and a photo of the final device are shown in Figure 2.4.

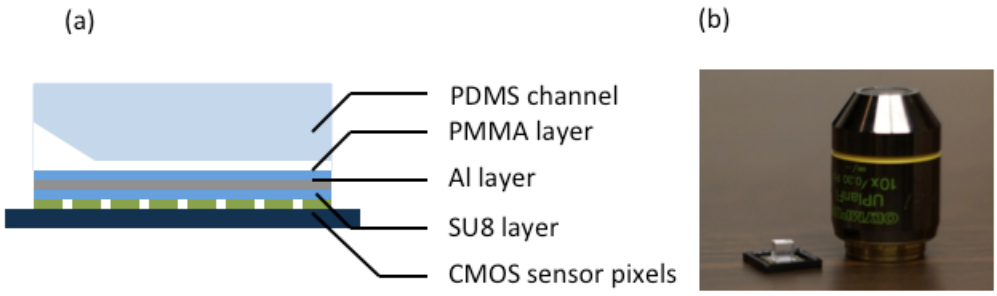

Figure 2.4. Color OFM device. (a) The illustration of the cross-section view of gravity driven color OFM setup. (b) The color OFM device compared with a microscope objective.

The system was uniformly illuminated with light (~10 mW/cm^2) from a halogen lamp. We programmed the sensor to specifically read signals from the two lines of pixels directly below the aperture arrays. The readout rate was 1.3 kHz/s. The time-varying transmission change measured through each aperture represents a line scan of a sample passing through the microfluidic channel. By stacking the line scans from the apertures together, we can then generate an image of the sample. Based on the aperture size, we have previously established that such a system has a resolution of 0.8 μm at its plane of highest acuity (bottom of the channel) [3].

2.4 The effect of the aperture on the color pixels

The image forming mechanism of OFM is different from that of the conventional microscope. Instead of collecting the light from a scattering spot within a certain collection angle, OFM uses small apertures to locally sample the light projection from the specimen. Thus the light collection efficiency through the aperture at different wavelength needs to be quantified. The spectral response of the device is measured by illuminating the device with light of different wavelength selected by a mono-chronometer. We recorded the spectral response range from 400-600 nm in 20 nm step increments.

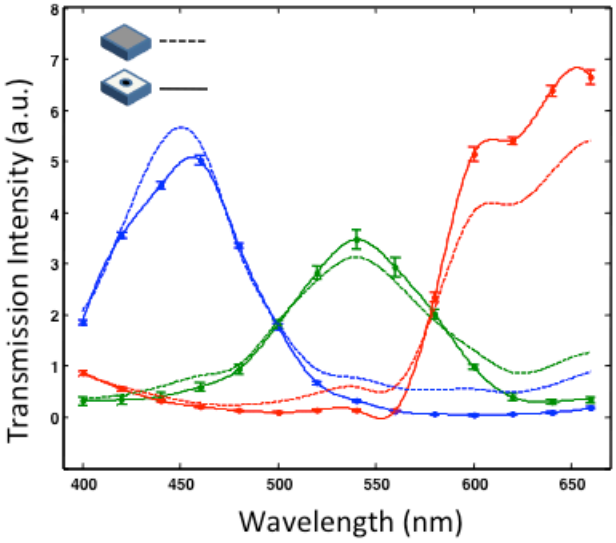

Figure 2.5. The small aperture effect on spectral response of the color sensor. The solid line are the measured transmission data from a color OFM device. The dash lines are the response from a CMOS sensor without any fabrication process.

Figure 2.5 shows the spectral response for the red, green, and blue pixels from the OFM device and compares it with an unprocessed color CMOS sensor. The results show that the blue and green pixels' spectral responses were slightly impacted by presence of the apertures while the red pixel showed some deviations. The impact is sufficiently moderate and positively indicates that our fabrication procedures did not significantly degrade the chromatic filters on the pixels. This set of data is helpful in aiding us renormalize the OFM measurements.

One of the advantages of color imaging is that the multi-spectral information can be used to quantify the relative concentration of the dye used in stained samples. For example, the optical signal detected by a blue pixel can be mathematically expressed as:

$$T_b = T_{bo} \exp(-\sigma_b n l), \tag{2.1}$$

where T_{bo} is the optical signal detectable in the absence of a sample, σ_b is the dye's absorption cross-section in the blue spectral region; n is the concentration of the dye; and l is the optical path length. We can write similar expressions for the red and green pixels. If the dye's absorption cross-section

spectral variation is known, we can determine the dye concentration by making four measurements: T_b, T_{bo}, T_r, and T_{ro}. The dye concentration can then be calculated from:

$$n = \frac{\ln(T_b/T_r) - \ln(T_{ro}/T_{bo})}{(\sigma_g - \sigma_b)l}, \tag{2.2}$$

from which we can see the linear relationship between $\ln(T_b/T_r)$ and the slope is independent of the illumination intensity, T_{bo} and T_{ro}. In this example, we chose the red and blue pixels as the target pixel pair. We can alternately pick any paired combination of the three color-pixels. Ideally, we should pick the color pixel associated with the largest dye absorption cross-section and the color pixel associated with the smallest dye absorption cross-section to maximize sensitivity.

To verify this capability, we flowed a blue dye, Trypan Blue, at varying concentration through a color OFM system. The microfluidic channel was 28 μm in height. The illumination intensity was 4 mW/cm^2. We varied the Trypan Blue concentration from 0 to 1.2 mM in 0.2 mM increments. The T_b and T_r measurements were acquired with pixels directly underneath the channel while the T_{b0} and T_{ro} measurements were acquired from pixels that were not covered by the channel. The result shown in Figure 2.6 verifies that the measured ratio $\ln(T_b/T_r)$ is a linear function of the dye concentration. To verify that this ratio is independent of the illumination intensity, we repeated the experiment at a higher illumination intensity of 6 mW/cm^2 by increasing the power of the halogen lamp. Figure 2.6 shows that the measured ratio overlapped with that of the original experiment.

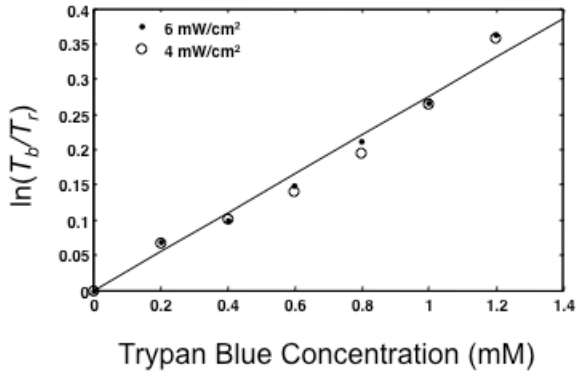

Figure 2.6. The normalized logarithm plot of the ratio of red to blue pixels after the passage of light through Trypan blue solutions. Two light intensities, 6mW/cm^2 and 4mW/cm^2, were used.

2.5 Color imaging of *C. elegans*

Next, we demonstrated our prototype by imaging *C. elegans* with for LacZ expression. The LacZ (β-galactosidase) gene is frequently used as a reporter in some bacterial-based selection techniques [4]. The location where LacZ is expressed can be easily located with a LacZ stain containing the artificial substrate X-gal, which turns blue when it is cleaved by β-galactosidase.

The *C. elegans* (pPD82.51) strain used contains a myo-2::lacZ fusion, which when expressed, stains the pharyngeal muscles of the worm's head blue after treatment with the X-gal, purchased from *Caenorhabditis* Genetics Center. The worms were fixed at their early larval stage L-1. We used the Lac Z Tissue Staining Kit (rep-lz-t, InvivoGen) for staining, and followed the protocol. In addition, we stained the worms with Ponceau-S, a stain commonly used to visualize proteins on Western blots, as a method of obtaining a second color, red, simultaneously on each worm. The stained worms were resuspended in 1 × PBS with a concentration about 10 worms/μL.

By operating the color OFM on an inclined plane, we were able to induce the *C. elegans* worms to flow through the microfluidic channel via gravitational pull. The transportation velocity ranged from 500 μm/s to 1000 μm/s. As in our previous experiments, we used the same halogen lamp as our light source. At this speed range and sensor readout speed, we could sample the worms in less than 0.5 μm intervals along the flow channel direction. This ensured adequate sampling and ensured that the image resolution was limited by the aperture size [1].

As both aperture arrays contained green pixels, we could constitute two green OFM images from the collected scans – one image for each set of green pixels. This redundancy was useful as it allowed us to 1) determine the flow speed of each worm, and 2) determine if the worms maintained their respective orientation and shape during the scan. The first task was accomplished by noting the time delay between when a worm passed the first and second green pixel array. By dividing the length separation between the arrays along the flow direction of the channel by this time delay, we could determine the flow speed. If a worm changed shape or orientation during the scan, we could expect the two green OFM images to look quite different. Therefore, the second task was accomplished by computing the cross-correlation between the two collected green images. We rejected any image set that had a cross-correlation value lower than 0.5.

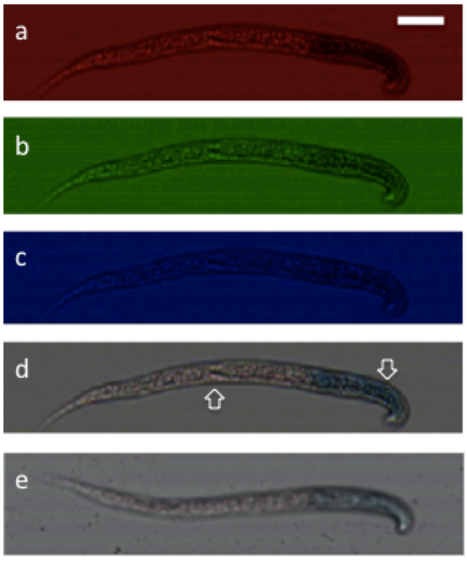

Figure 2.7. Reconstruction of a color OFM image of *C. elegans* with LacZ expression. (a)-(c) From top to bottom are the images from red, green, blue pixels of a *C. elegans* with blue Xgal stain and ponceau stain image, (d) the constructed color OFM image shows the nonspecific ponceau stain (left arrow) and the LacZ staining of the pharyngeal muscles (right arrow), (e) the conventional 10X microscope image of the same sample. The scale bar is 20 microns.

Figure 2.7 shows the color OFM images of a *C. elegans*. The LacZ stains the pharyngeal muscles of the worm blue, and Ponceau attached nonspecifically to proteins in the worm. The LacZ staining is clearly visible in the red and green OFM images, and is difficult to identify in the blue OFM images. This observation is consistent with the fact that the LacZ staining absorbs strongly in the red and green part of the spectrum and that it absorbs the blue part of the spectrum weakly. We balanced the ratio of the three color channels to ensure the background of the image had same value as the three components. The combined color image is comparable with a balanced brightfield image from a conventional microscope with a 10X objective using the same imaging sensor. The color OFM image can help us visualize the nonspecific Ponceau red staining in the middle and the tail part of the worm. Figure 2.8 compares the color image to the monochromatic image by summation of the three color-channels. Our prototype's ability to image and distinguish color stains in samples represents a significant improvement over our previously reported OFM devices.

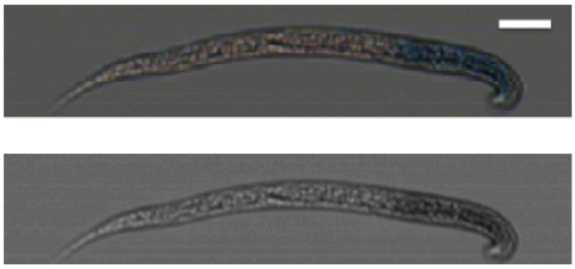

Figure 2.8. The comparison between the color OFM image and the monochromatic image. The scale bar is 20 microns.

As this color OFM design is microfluidic based, it can form part of a greater microfluidic analysis system in which sample prep and staining are all performed on chip. It is also possible to envision more sophisticated staining and imaging strategies in order that such a compact imaging system could be used optimally. For example, the color OFM can be used to automatically image samples that are sequentially stained with different dyes, in which imaging is performed after each staining step. Such a scheme is difficult to automate in a conventional laboratory, but is relatively simple to implement in a well-controlled microfluidic system [5].

2.6 Conclusion

In summary, we reported the operating principle of the color OFM prototype, its calibration experiments, and its capability of determining the dye concentration with varying illumination intensity. We also demonstrated the imaging of a double stained *C. elegans* with lacZ gene expression with the color OFM device.

REFERENCES

1. X. Q. Cui, L. M. Lee, X. Heng, W. W. Zhong, P. W. Sternberg, D. Psaltis, and C. H. Yang, "Lensless high-resolution on-chip optofluidic microscopes for *Caenorhabditis elegans* and cell imaging," *Proceedings of the National Academy of Sciences of the United States of America* **105**, 10670-10675 (2008).
2. X. Heng, D. Erickson, L. R. Baugh, Z. Yaqoob, P. W. Sternberg, D. Psaltis, and C. H. Yang, "Optofluidic microscopy - a method for implementing a high resolution optical microscope on a chip," *Lab on a Chip* **6**, 1274-1276 (2006).
3. X. Heng, X. Q. Cui, D. W. Knapp, J. G. Wu, Z. Yaqoob, E. J. McDowell, D. Psaltis, and C. H. Yang, "Characterization of light collection through a subwavelength aperture from a point source," *Optics Express* **14**, 10410-10425 (2006).
4. J. K. Joung, E. I. Ramm, and C. O. Pabo, "A bacterial two-hybrid selection system for studying protein-DNA and protein-protein interactions," *Proceedings of the National Academy of Sciences of the United States of America* **97**, 7382-7387 (2000).
5. T. Thorsen, S. J. Maerkl, and S. R. Quake, "Microfluidic large-scale integration," *Science* **298**, 580-584 (2002).

C h a p t e r 3

FRESNEL ZONE PLATE BASED FLUORESCENCE OPTOFLUIDIC MICROSCOPE

In the previous chapters, we have introduced the imaging principles and implementation of bright field/color optofluidic microscopes (OFM). In this chapter we report the implementation of an on-chip fluorescence microscope system, termed fluorescence optofluidic microscope (FOFM). This device is capable of fluorescence microscopy imaging of samples in fluid media. The FOFM employs an array of Fresnel zone plates (FZP) to generate an array of focused light spots within a microfluidic channel. As a sample flows through the channel and across the array of focused light spots, the fluorescence emissions are collected by a filter-coated CMOS sensor, which serves as the channel's floor. The collected data can then be processed to render fluorescence microscopy images at a resolution determined by the focused light spot size (experimentally measured as 0.65 μm FWHM). In our experiments, our established resolution was 1.0 μm due to Nyquist criterion consideration. As a demonstration, we show that such a system can be used to image the cell nuclei stained by Acridine Orange and cytoplasm labeled by Qtracker®. This Chapter is adapted from S. Pang, C. Han, L. M. Lee, and C. H. Yang, "Fluorescence microscopy imaging with a Fresnel zone plate array based optofluidic microscope", *Lab on a Chip* **11**, 3698-3702 (2011).

3.1 Introduction

In the past few years, there has been significant research and development in the area of bright field chip-scale microscopy [1, 2]. An inexpensive, highly compact and easy-to-use chip-scale microscope can be an important lab-on-a-chip component for point-of-care medical systems, low-cost diagnostic tools for developing country applications, and high-throughput automated bioscience analysis systems. A high-resolution and generally usable fluorescence on-chip microscopy technique can significantly expand the utility range of such chip-scale microscopes. The high sensitivity of the fluorescence signal detection and the broad array of fluorophore species and expression techniques available make fluorescence one of the most important read-out modes for microscopy [3].

This recognition has driven a number of research efforts in developing a useful fluorescence on-chip microscopy technique. However, the incoherent nature of fluorescence and the need for high quality optical filters are significant design obstacles.

Coskun *et al*. show that it is possible to superpose an indication of the fluorophore concentration sites onto brightfield in-line holography derived images of samples as long as the fluorophores are clustered and the clusters are well separated (by ~ 10 μm) [4]. A progression of that effort uses bundled fibers to collect and channel fluorescence to a sensor and was able to generate fluorescence images that have a claimed resolution of ~ 4 μm [5]. Improving the technique's resolution to the point where sub-cellular fluorescence features are resolvable may prove challenging as finer fiber tips will further diminish the effective fluorescence collection angle and the light channeling efficiency.

In this chapter, we report a chip-scale imaging method, termed "fluorescence optofluidic microscope" (FOFM), which adapts the scan-based imaging strategy of the optofluidic microscopy method to accomplish high-resolution fluorescence microscopy imaging. Compared with aperture based on-chip imaging platform [2], this approach is highly efficient at fluorescence light collection. It is also capable of placing the plane of highest acuity at any desired height within the sample and its resolution can be adjusted by a straightforward alteration of its design parameters. Our FOFM prototypes were able to achieve 0.60 μm FWHM at the focused spot for excitation wavelength of 405 nm and 0.65 μm FWHM for 488 nm excitation. The FOFM is suitable for mass-manufacture in a semiconductor foundry, and therefore FOFM devices have the potential to be made very compactly and cost-effectively.

In the following section, we will describe the FOFM's imaging principle. Then, we will describe the fabrication steps involved in our prototype construction. Next, we will discuss our characterization of the experimental results and report on our demonstration experiments that use our prototypes for fluorescence microscopy imaging of cells.

3.2 Fluorescence optofluidic microscope (FOFM)

3.2.1 Imaging principle

The FOFM basic design is centered around a microfluidic channel. Figure 3.1 shows the illustration of the FOFM device. An array of Fresnel zone plates (FZP) patterned on a metal layer forms the ceiling of the channel. Under uniform plane illumination with an appropriate excitation light source from the top, each FZP focuses light into a tight spot within the microfluidic channel.

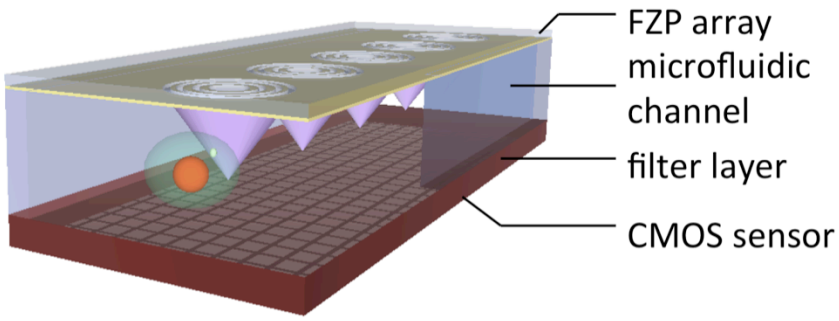

Figure 3.1. Schematics of the Fresnel zone plate based fluorescence opto-fluidic microscope (FOFM). A sample flows in the microfluidic channel on top of the filter coated image sensor. The Fresnel zone plate array creates an array of foci inside the channel.

As a sample flows through the channel, each focused light spot will locally excite fluorophores within the sample. The fluorescence signal collection is accomplished by a low-cost CMOS sensor, which is coated with a filter that effectively blocks the excitation light and that efficiently transmits fluorescence emissions well. The time varying fluorescence signal associated with each spot represents a single line scan across the sample. Figure 3.2 shows the geometry of the FZP arrangement. The FZP array spans the channel diagonally such that the distance between the adjacent scan lines is less than the FWHM of the PSF of each focus. This assures that we can fully scan all parts of the sample and that by appropriately compositing all line scans, we can then generate a high-resolution fluorescence image of the sample at a resolution that is limited by the focused spot size.

The FOFM design enables fluorescence microscopy imaging. This is not achievable with earlier versions of OFM designs [1, 2]. For previous OFM designs, the effective plane of highest acuity is right above the sensor surface. The achievable image resolution degrades as a function of object-to-sensor separation [1]. The placement of an optical filter layer on the sensor surface to accomplish fluorescence imaging would necessarily introduce an unacceptable separation and degrade the image resolution significantly. In this current FZP OFM design, the plane of highest acuity (where the light spots focus) can be set at arbitrary height within the microfluidic channel and, as such, can tolerate a significant object-to-sensor separation. This freedom allows us to place an appropriate optical filter on the sensor for fluorescence imaging purpose.

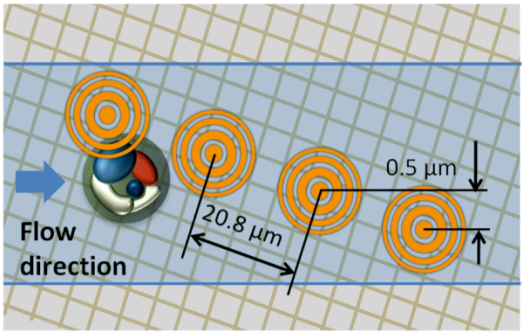

Figure 3.2. Geometry of the FOFM device (top view). The Fresnel zone plates are defined on the top floor of the microfluidic channel and span across the whole microfluidic channel (blue region).

3.2.2 Fresnel zone plate

For each of our FOFM prototypes, we fabricated the FZP array on a 300 nm thick chrome layer that was plated on a quartz substrate. Each FZP was composed of a series of transparent and opaque concentric rings [6]. Figure 3.3 (a) illustrates the FZP focusing.

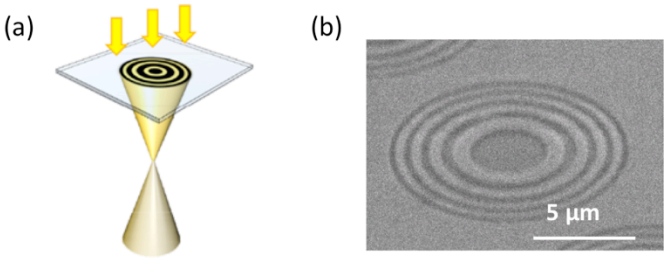

Figure 3.3. Fresnel zone plate (FZP) focusing. (a) The illustration of the FZP focusing (b) SEM image of a binary FZP patterned on a chrome mask.

To create the focus at a focal length f the zones should switch from opaque to transparent at radii

$$r_k = \sqrt{kf\frac{\lambda}{n} + \frac{k^2\lambda^2}{4n^2}}, \tag{3.1}$$

where k is an integer, λ is the wavelength of the light and n is the refractive index of the medium in which the focus is formed. The resolution, δ, of a focal spot of a zone plate depends on the smallest zone width [6]

$$\delta = 1.22\Delta r_K, \tag{3.2}$$

where Δr_K is the outer most zone width, which is determined by the fabrication limit. In our case, the FZP pattern was defined by electron beam lithography with a minimum achievable line width of 400 nm. The depth of the focus Δ [7], defined the half distance between two adjacent axial intensity minima of a FZP focus, can be calculated as

$$\Delta = f / N, \tag{3.3}$$

where N is the number of transparent zones, which is five in our design. Figure 3.3 (b) shows a scanning electron microscopy image of a single FZP in our prototypes. The distance between each FZP was 20.8 μm - this corresponds to the length of four sensor pixels on the CMOS sensor. The designed focal length was 13 μm and the diameter of each FZP was 15 μm. The exact FZP ring parameters were governed by Equation 3.1 and they differed between the two groups of FOFM prototypes we implemented. One group was designed to work at an excitation wavelength of 405 nm and the other at an excitation wavelength of 488 nm.

3.2.3 Device fabrication

The base of each of our FOFM prototypes was a monochromatic CMOS sensor. The sensor (Aptina, MT9M001) consists of 1280 × 1024 pixels of size 5.2 μm. Prior to any fabrication, we removed the glass cover to allow direct sensor surface access. We then planarized the sensor surface with a layer of Poly(methyl methacrylate) (PMMA).

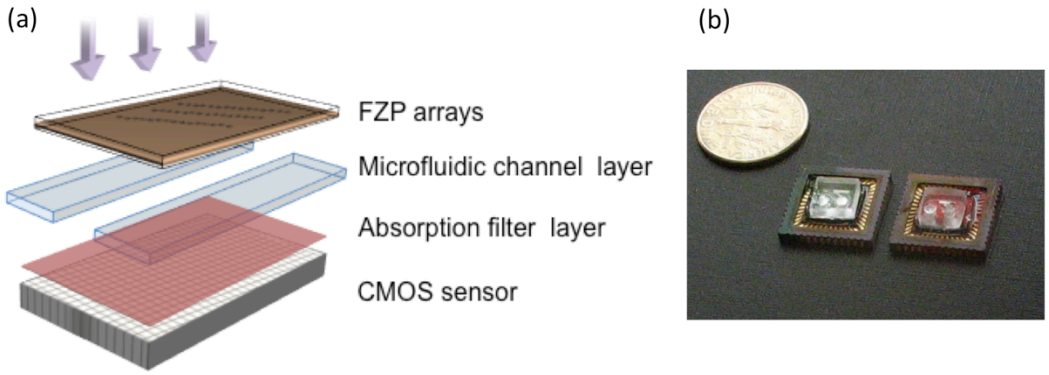

Figure 3.4. FOFM device. (a) The schematics of the FOFM device. (b) The photograph of two FOFM prototypes with green and red filter layers placed besides a US dime to show their size.

Next we coated the sensor with an appropriate filter layer. The FOFM filter layers consisted of an appropriate filter pigment dissolved in a photo-resist based material and patterned and cured directly onto the sensor. Two different filter pigments, Aptina green1 and Aptina red1 (provided by Aptina Imaging), were used. The green filter is a band pass filter that provides an optical density (OD) difference of about six between 488 nm excitation and 520 nm emission at a filter thickness of 8 μm. The red filter, which transmits the wavelength above 560 nm, provides an OD difference of nine between 405 nm excitation and 625 nm emission for a filter thickness of 6 μm. Figure 3.5 shows the transmission spectrum of the green and the red filter.

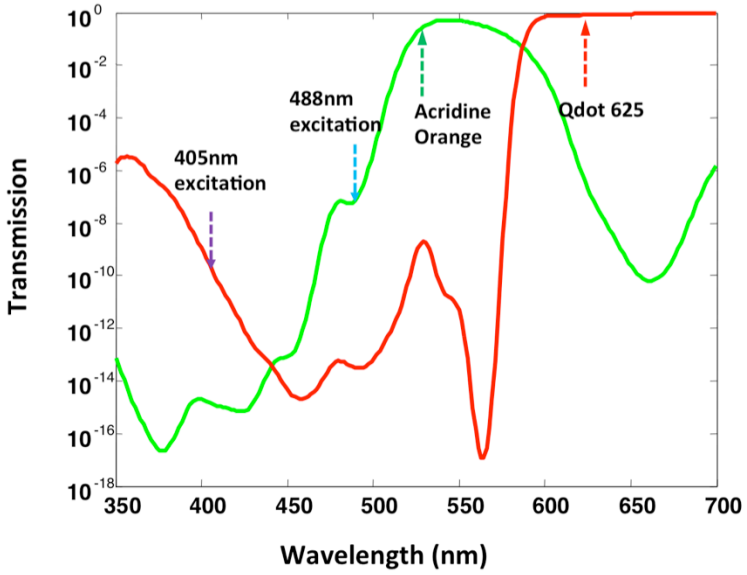

Figure 3.5. The transmission spectrum of 6 μm thick red filter layer and 8 μm thick green filter layer. The arrows indicate the emission peaks of Acridine Orange and Qdot 625. The 405 nm and 488 nm excitation lines are also marked for reference. The transmission measurement is done at 1.5 μm thickness. The OD number at 6 and 8 μm are calculated results.

The microfluidic channel was fabricated using polydimethylsiloxane (PDMS) [8]. A stamp with positive channel pattern was defined by the photo-resist SU-8 (2015, Microchem Inc.) on a glass substrate. A spin coater coated a 20 μm thick SU-8 layer at a spin speed of 1700 rpm. An uncured PDMS droplet was placed on the sensor. The channel on the stamp was set at an angle of 0.03 radian to the direction of a row of the pixels. This ensured that adjacent FZPs overlapped each other by 0.5 μm across the width of the channel. The stamp was then pressed onto the sensor while applying the heat. The PDMS was cured at 85 °C with 15 minutes bake time. After the removal of the stamp, a profiliometer measured the depth of the channel. This process introduced an extra layer of PDMS underneath the channel [9]. The thickness of the layer was measured to be 2-3 μm. Finally a mask aligner (MJB3, Karl Suss) aligned an FZP array to the fabricated sensor chip with the microfluidic channel and filter layer.

3.3 Resolution of the FOFM

To verify the focus quality, we observed the focus formed by the FZP by a 40X 0.85 N.A. water immersion microscope objective. Here we used the water immersion microscope objective to match the refractive index of the medium in the microfluidic channel. A piece of the top plate with FZP arrays was mounted on a vertical motorized stage. The stage moved with a step size of 0.5 μm, and a camera captured images of the focus at each step. Figure 3.6 shows the experimental results. The FWHM of the focus was 0.60 μm for 405 nm excitation, and 0.65 μm for 488 nm excitation, which were slightly larger than the theoretical value of 0.5 μm. The focal depth for the 405 nm version was 4.0 μm, and the focal depth for the 488 nm version was 3.5 μm.

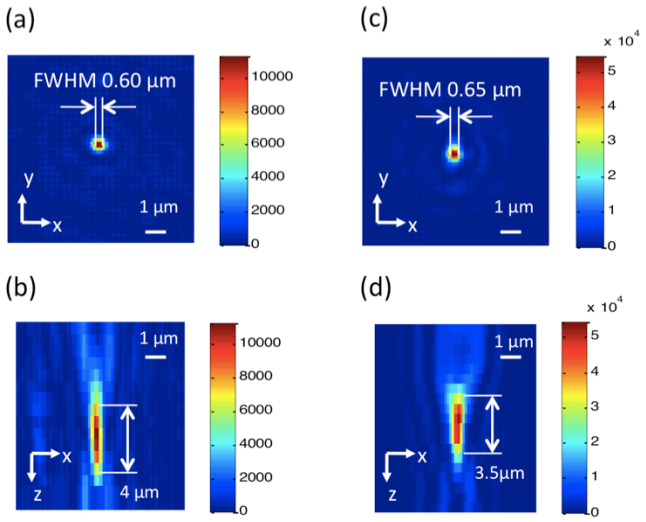

Figure 3.6. The intensity profile of the focus generated by FZP. (a) The intensity of the focus at the focal plane by 405 nm excitation. (b) The depth-wise cross-section of the intensity of the focus by 405 nm excitation. (c) The intensity of the focus at the focal plane by 488 nm excitation. (d) The depth-wise cross-section of the intensity of the focus by 488 nm excitation.

3.4 Fluorescence imaging with the FOFM prototype

In our demonstration a 488 nm laser (Cyan OEM488 nm, Spectra-Physics) and a 405 nm laser (OEM Laser System Inc.) were used as the excitation sources for the FOFM. The power at each FZP generated focal spot was about 10 μW. During operation, the imaging frame rate was 1 kHz.

In all of our FOFM prototypes, we opened a window in the chrome layer of the channel ceiling. Under illumination with a white LED (MCWHL2, Thorlabs Inc.), we were able to capture 200

frames of low-resolution bright field images of sample flowing through that segment of the microfluidic channel. These images could then be processed to form a higher-resolution image by using the sub-pixel resolving OFM (SROFM) method described in [10].

The SROFM method's resolving ability degrades as a function of sample-to-sensor separation. Since the FOFM sensor chips were coated with a ~13 μm thick layer of filter material and PDMS material, the acquired SROFM images are relatively low in resolution. Nevertheless, they could be used to provide outlines of the samples imaged. In applications where high-resolution brightfield microscopy images are required, the on-chip microscope can be designed to exclude the filter material from the SROFM portions of the sensor chip.

3.4.1 FOFM imaging of fluorescence microspheres

To verify the proper operation of our FOFM prototypes, we first conducted a verification experiment by employing an FOFM device to image a control which consisted of a fluorescence microsphere of diameter 8 μm (DG06M, Bangs Laboratories Inc.). The fluorophores were evenly distributed within the sphere. The excitation wavelength used was 488 nm and the center emission fluorescence wavelength was 520 nm. Since we know the power distribution associated with each focused light spot from the data presented in Figure 3, we can calculate the expected fluorescence emission measured by the sensor pixels as the microsphere traverses a single focused light spot. We compared the result derived from a calculation to our experimental results as shown in Figure 3.7. The good agreement verified the proper operation of our FOFM prototypes.

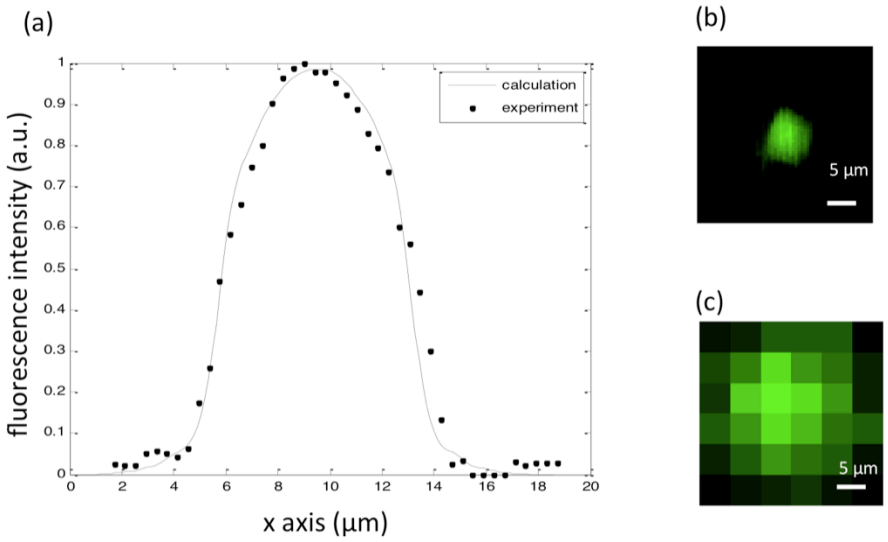

Figure 3.7 Microsphere imaging by FOFM. (a) A line trace of a fluorescence microspheres by a single FZP, comparing to the calculation result. (b) The fluorescence image of a fluorescence microsphere collected by FOFM. (c) The fluorescence image of a fluorescence microsphere by direct readout from the sensor with uniform illumination.

3.4.2 FOFM imaging of fluorescently labeled HeLa cells

We next employed our FOFM prototypes to image fluorescence stained cells. The cell samples used in the experiments were suspended HeLa cells (CCL-2, ATCC). We prepared two types of stained cells. In one preparation, we loaded quantum dots (QDs) in the cytoplasm with Qtracker® 625 Cell Labeling Kit (A10198, Invitrogen). The kit uses a custom targeting peptide to deliver Qdot 625 into the cytoplasm of live cells [11]. Qdot 625 can be excited at 405 nm and has an emission peak wavelength of 625 nm. In a second preparation, we stained the nuclear content of the cells with Acridine Orange (A1301, Invitrogen). For this, we incubated live cells with 20 μg/ml Acridine Orange solution (PBS buffered) for 5 minutes and triple rinsed with PBS before imaging. Acridine Orange can be excited at 488 nm and has an emission peak at 525 nm. We flowed the stained cells in our FOFM prototypes to acquire fluorescence images.

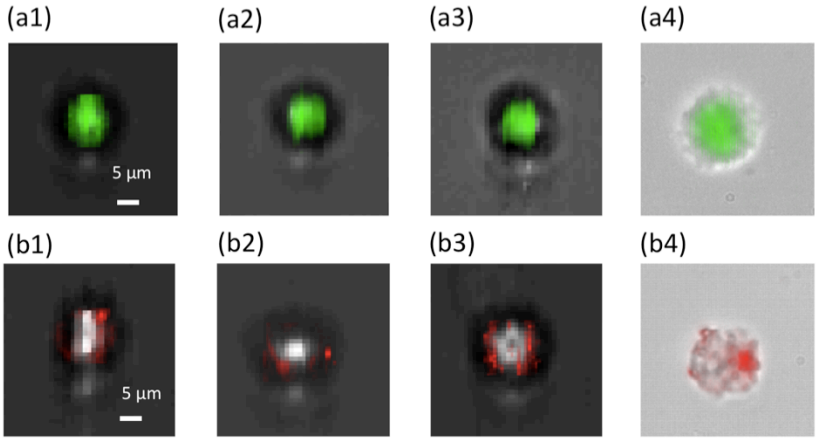

Figure 3.8. Fluorescence images of stained HeLa cells collected by FOFM. (a1-a3) The fluorescence images of Acridine Orange stained HeLa cells acquired by FZP FOFM superimposed on defocused bright field SROFM images to provide the outline. (b1-b3) The fluorescence images of Qtracker labled HeLa cells acquired by FZP FOFM superimposed on defocused bright field SROFM images. (a4, b4) The fluorescence image superimposed on a bright field image acquired by a conventional 20X 0.4 N.A. microscope.

The flow speed was approximately 500 μm/s, and the frame period was 1 ms, corresponding to the displacement of 0.5 μm per frame. Each sample's flow speed uniformity was monitored by the SROFM segments of the prototypes, and the yield rate was comparable to those of earlier OFM systems [1]. The green filter coated FOFM captured images of the Acridine Orange stained cells, and the red filter coated FOFM captured images of the Qtracker® stained cells. The fluorescence images captured by FOFM prototypes were superimposed with the super-resolution bright field images. Figure 3.8 (a1-a3) shows images of the HeLa cell nuclei stained by Acridine Orange. The fluorescence signal is concentrated within the center of a cell. Figure 3.8 (b1-b3) shows the images of the HeLa cytoplasm labeled by Qtracker®. The Qtracker contrast agents are non-specific-binding quantum dots. The Qtracker stain pattern is expected to vary from cell to cell. We also acquired images with a conventional microscope operating with a 20X 0.4 N.A. objective for comparison (Figure 3.8 (a4) and (b4)). We can see that the fluorescence images acquired with the FOFM prototypes agree with those acquired with a conventional fluorescence microscope.

We note that the FOFM's resolution is fundamentally set by the FZP's focused spot size. However, in our prototypes, our sampling step-sizes in both x- and y-axes impose a resolution limit of 1

micron to our fluorescence images due to Nyquist sampling criterion considerations [12]. To achieve the resolution set by the FZP's focused spot size, we would need to increase the sampling frame rate and increase the line scan overlap.

3.5 Discussion

In this section, we would like to point out several features of our FOFM design and the potential improvments.

First, the choice of using a filter coated CMOS sensor to serve as the device's floor carries two advantages. Specifically, we can optimally collect fluorescence from the sample without requiring the use of a more elaborate collection optics scheme. The FOFM design can collect almost all fluorescence from the bottom semisphere of an isotropic fluorescence source, which is close to 50% of the total emission. In contrast, a 0.65 N.A., 40X microscope objective is only able to collect ~12% of the total emission. In addition, this simple planar and monolithic collection design is very compatible with semiconductor mass-manufacture.

Another noteworthy point of this FOFM design is that, by spacing the FZP apart from each other at an adequate distance, it is possible to separate the detected fluorescence associated with each focused spot by the CMOS sensor without ambiguity. More interestingly, if the approximate size of the sample is known, we need only space the FZP at a distance larger than the sample size to guarantee that cross-talk is absent - in this case, only one focused spot can interrogate the sample at any given time and any signal we see on the sensor can be automatically attributed to that focused spot. In fact, our FOFM prototypes made good use of this design point. A thick layer of filter material and PDMS separates the sensor pixels from the channel: the overall thickness is about 13 microns. The fluorescence from a fluorophore in the center of one of the focused light spots would spread over an area of diameter at least 30 μm (or 6-7 sensor pixel lengths) on the sensor. This implies that at our FZP-to-FZP distance of 20.8 μm, fluorescence signals associated with adjacent focused light spots could overlap and contribute cross-talk to each other. The cells used in our experiments are less than 20 μm in diameter and, as such, only one focused light spot can excite a given cell at anytime and we were able to avert cross-talk problems. To work with large cells or samples, we simply would need to increase the FZP-to-FZP distance.

On a different note, it is worth contrasting the use of an FZP array with the use of a conventional lenslet array in the FOFM design. The FZP fabrication process is compatible with semiconductor

mass-manufacture. This is a relevant consideration as we envision the mass-manufacture of OFM would occur in semiconductor foundries. Further more, the FZP approach allows for the generation of tight focus spots with short focal length that would be very difficult to accomplish with a refractive optical element. As a case in point, if we were to replace one of the FZP elements in our prototype with a ball lens of the same diameter, the ball lens would have to possess a refractive index of at least 2.7 (in comparison to quartz glass, which has a refractive index only 1.45 in the optical band) to achieve the same focal length. The FZP approach does come at a flexibility price, since the focal length of the FZP depends strongly on the optical wavelength. As such, each FOFM needs to be designed with a specific excitation wavelength in mind. Finally, our current FZP is able to direct ~10% of the incident light into the focused spot. If application requirements demand higher efficiency, the current binary FZP can be switched to a binary phase FZP, which has 40.4% ($4/\pi^2$) efficiency, or a Fresnel lens, which in principle can reach 100% efficiency.

3.6 Conclusion

In this chapter, we described the imaging principle and the implementation of the FOFM system based on an FZP arrays. We demonstrated the imaging ability of our FOFM prototypes by imaging HeLa cell nuclei stained by Acredine Orange and HeLa cytoplasm labeled by Qtracker® 625. The resolution of such systems is limited by the focused spot size of the FZP. For our prototype, these are 0.60 μm for 405 nm, and 0.65 μm for 488 nm excitation. This FOFM design intrinsically achieves high fluorescence collection efficiency and its planar and monolithic design should allow straightforward semiconductor foundry-based mass manufacture.

REFERENCES

1. X. Cui, L. M. Lee, X. Heng, W. Zhong, P. W. Sternberg, D. Psaltis, and C. Yang, "Lensless high-resolution on-chip optofluidic microscopes for *Caenorhabditis elegans* and cell imaging," *Proceedings of the National Academy of Sciences of the United States of America* **105**, 10670 (2008).
2. S. Pang, X. Cui, J. DeModena, Y. M. Wang, P. Sternbergc, and C. Yangab, "Implementation of a color-capable optofluidic microscope on a RGB CMOS color sensor chip substrate," *Lab on a Chip* **10**, 411-414 (2010).
3. R. Y. Tsien, L. Ernst, and A. Waggoner, "Fluorophores for confocal microscopy: photophysics and photochemistry," *Handbook of biological confocal microscopy*, 338-352 (2006).
4. A. F. Coskun, I. Sencan, T. W. Su, A. Ozcan, and E. Mylonakis, "Lensfree Fluorescent On-Chip Imaging of Transgenic *Caenorhabditis elegans* Over an Ultra-Wide Field-of-View," *PloS one* **6**, 896-903 (2011).
5. A. F. Coskun, I. Sencan, T. W. Su, and A. Ozcan, "Wide-field lensless fluorescent microscopy using a tapered fiber-optic faceplate on a chip," *Analyst* (2011).
6. M. Young, "Zone plates and their aberrations," *Journal of Optical Society of America* **62**, 972-976 (1972).
7. M. Sussman, "Elementary diffraction theory of zone plates," *American Journal of Physics* **28**, 394 (1960).
8. Y. Xia, and G. M. Whitesides, "Soft lithography," *Annual Review of Materials Science* **28**, 153-184 (1998).
9. M. Heckele, and W. K. Schomburg, "Review on micro molding of thermoplastic polymers," *Journal of Micromechanics and Microengineering* **14**, R1 (2004).
10. G. Zheng, S. A. Lee, S. Yang, and C. Yang, "Sub-pixel resolving optofluidic microscope for on-chip cell imaging," *Lab on a Chip* **10**, 3125ñ3129 (2010).
11. N. Umezawa, M. A. Gelman, M. C. Haigis, R. T. Raines, and S. H. Gellman, "Translocation of a -peptide across cell membranes," *Journal of the American Chemical Society* **124**, 368-369 (2002).
12. A. V. Oppenheim, R. W. Schafer, and J. R. Buck, *Discrete-time signal processing* (Prentice hall Englewood Cliffs, NJ:, 1989).

Chapter 4

FLUORESCENCE TALBOT MICROSCOPY

This chapter intends to provide an overview of a fluorescence microscope based on the Talbot effect. In the previous chapter, we have described the implementation of a fluorescence on-chip imaging device based on OFM methods. In addition to the cost-effectiveness and compactness associated with on-chip microscopy, the fluorescence Talbot microscope (FTM) method explores the possibility of achieving wide field-of-view (FOV) and high collection efficiency. The chapter starts with a brief review of the methods used to achieve wide FOV in fluorescence microscopy, particularly by focal spot array scanning microscopy for high-speed imaging. Next we will give a brief introduction of the Talbot effect and some of its key properties, which serve as the foundations for the FTM method. In the third section, we will describe the working principle of the FTM and report an implementation of the on-chip prototype of the FTM. Finally we will show the fluorescence microscopy images acquired by the on-chip FTM prototype.

The characterization of the on-chip FTM will be described in Chapter 5, and in Chapter 6 we use the Talbot microscope method in imaging samples labeled with two different fluorescence stains. In Chapter 7 we will report two biological applications using the FTM. Chapter 8 will discuss the potentials and the outlook for FTM methods.

4.1 Wide FOV microscopy

4.1.1 Conventional microscope achieving wide FOV

The conventional microscope has limited FOV due to the constraints of the available optical material and design. One possibility to increase the FOV of the microscope is to increase the physical aperture of the microscope. However the aberration also increases if one just simply scales up the optical design. If the aberration is compensated for, the design becomes complicated and the cost of the system increases. Such large aperture lenses are used in photolithography lenses [1], and are not suitable for a biology laboratory.

Several technologies have been recently developed to enable high throughput screening for diagnosis and gene activity quantification [2-4] by transporting the samples under the conventional

microscope's FOV to increase the throughput. Figure 4.1 shows a microscope slide scanner based on this method. However, the inclusion of a conventional microscope precludes system parallelization that could otherwise bring orders-of-magnitude throughput improvements.

Furthermore, there are certain applications, such as living cell time-lapse imaging, where photo-bleaching and photo-toxicity are major concerns [5]. In these situations, users typically have to trade-off a larger FOV against increased light collection efficiency by resorting to a high magnification microscope objective, which increases the imaging time and the system cost.

Finally, the time spent on the step motion and focus readjustment is longer than the imaging time. State-of-art commercialized slide scanners use time delayed integration (TDI) cameras, so that a continuous scan can be applied in one scan direction, while the step movement is still required in the other direction [6]. This effort can reduce the full field imaging time, yet the TDI camera is not common in most labs.

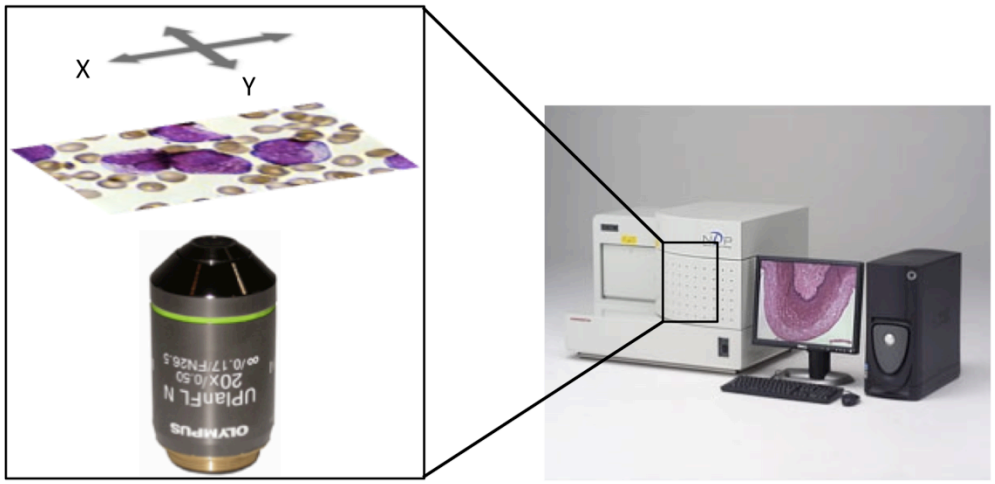

Figure 4.1. Wide FOV achieved by a conventional microscope. An example of digital slide scanner by Hamamatsu, where a motorized stage translates the slides under the microscope objective's FOV. Figure courtesy of Ref [6].

4.1.2 Chip-scale fluorescence microscope achieving wide FOV

Chip-scale fluorescence microscopes can potentially provide a wide FOV. In chip-scale microscope devices, the FOV is limited by the imaging sensor size, which is ~100 times larger than the FOV of a 20X microscope objective. Among the existing chip-scale microscope designs, the hologram method is not feasible, because of the non-coherent nature of the fluorescence signal. In a reported lens-less microscopy, which is based on post digital processing, the fluorescence point spread function (PSF) needs to be measured. Then deconvolution and compressed sensing are applied to the defocused fluorescence image to calculate the position and intensity of the fluorophore [7]. This method fails when the PSF is modified [8], as in the common cases where the fluorophore is out of the calibration plane, or there are scattering samples in the vicinity of the fluorophore. Moreover, the algorithm assumption limits the applications to only sparse fluorophore distribution [9].

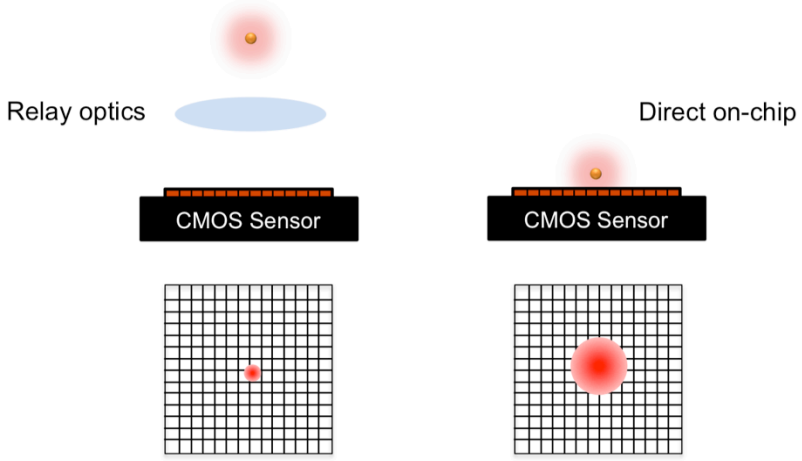

Figure 4.2. The comparison between on-chip detection and detection using a relay lens.

Because of the distance from the sample to the imaging sensor, the fluorescence spreads out on the sensor, and the PSF is usually on the order of 10-100 μm. Figure 4.2 shows this collection geometry compared with collection using imaging optics. As a result, the achievable resolution is only ~10 μm, for on-chip detection.

Fluorescence optofluidic microscopy (FOFM), as described in the previous chapter, gives a very good way to bypass the unknown fluorescence spread. Instead of relying on the CMOS sensor's resolution, an array of sharp excitation foci generated by Fresnel zone plate arrays is applied to

achieve high resolution [10]. FOFM provides resolutions as high as 1.0 μm, but it places limitations on the sample size, as the sample was translated in a microfluidic channel.

4.1.3 Focal spot grid scanning microscope

Instead of translating the sample as in the FOFM method, alternatively, we can translate the focal array to scan the sample. Recent works have demonstrated the use of point scans to improve the scanning speed in microscope systems [11-14]. In these methods, a grid of focal spots is generated by a grid of microlenses [13], a diffractive optical element [14], or a hologram plate [11]. The dimension of the focal spot grid can be designed to be much larger than the FOV of a microscope objective (< 1 mm), and even larger than the standard microscope slides (~15 mm).

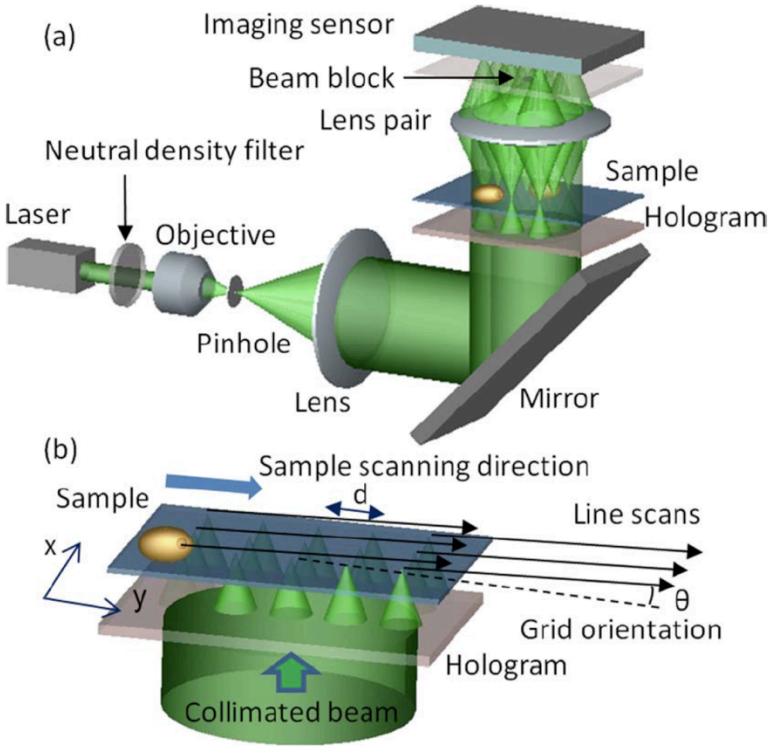

Figure 4.3. An example of a wide FOV microscope based on a hologram generated focal spot array. (a) System setup of the wide FOV microscope. (b) Scanning mechanism employed for imaging. Image courtesy of Ref [11].

Figure 4.3 shows the focal spot grid microscope described in Ref [11]. As the sample or the focal spot grid is transported by a mechanical stage, the focal spot grid scans across the sample and a relay optics system collects the fluorescence emission from each focal spot to form the full FOV image.

As long as the pitch of the focal spot grid is larger than the spread of the fluorescence on the chip, we can distinguish the fluorescence signal without relay optics. However, the scanning method requires the inclusion of a translational stage, which is bulky and expensive. This contradicts the spirit of creating a low-cost and portable fluorescence microscope.

An alternative scanning method would be to tilt the incident wave front in the same way as is done in the laser-scanning microscope. To achieve a full field scan using a lens, the focal spots need to cover the full size of the aperture. However, an angular scanning scheme of the focal spot grid would be questionable due to the off-axis aberration. The off-axis aberration will deteriorate the point spread function (PSF) of the focal spots, as illustrated in Figure 4.4. Therefore, the angular scanning method does not seem to be suitable for imaging.

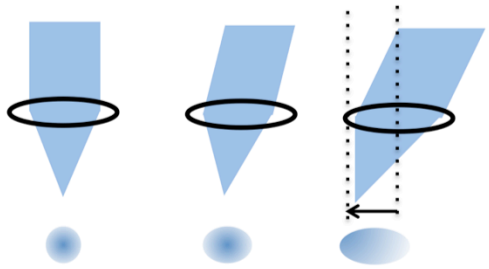

Figure 4.4. An illustration of the angular scanning using a lens. By tilting the incident beam, shift of the focal spot can be achieved. However, to cover the whole area under the aperture, a large angle is needed, and the off-axis aberration is significant.

Instead of scanning using the original spot, we can shift the focal spot generated by Talbot effect. In the next section we will introduce the Talbot effect, and explain how it enables the large FOV high resolution on-chip imaging.

4.2 The Talbot effect and its properties

The Talbot effect is a self-imaging phenomenon of a periodic pattern: the diffraction pattern of a two-dimensional planar structure under coherent planar illumination shows copies of the periodic input pattern. The Talbot effect was first observed by Henry Fox Talbot in 1836 [15]. To be specific, the periodic structure will repeat its pattern along the propagation direction at $z = nz_T$, where n is an integer, and

$$z_T = \frac{2d^2}{\lambda}, \tag{4.1}$$

where d is the period of the structure, and λ is the wavelength. Figure 4.5 shows the Talbot effect for a periodic aperture array. Notice here at half Talbot distance, $z = z_T/2$, the aperture array repeats itself but has a half-pitch shift from the original structure.

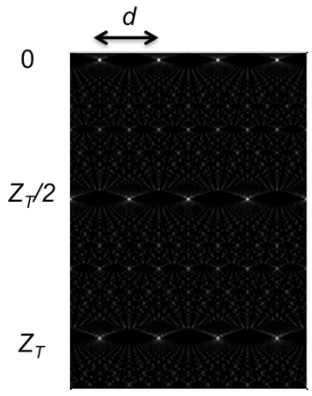

Figure 4.5. Illustration of the Talbot Effect. At z = 0, the periodic pattern is the aperture array with pitch d. At the Talbot length z = z_T, the light can be seen to repeat the exact pattern.

Talbot effect is pseudo-self-imaging: the imaging spot and the original spot do not have one-to-one correspondence. Each spot on the Talbot image is contributed from multiple spots on the original plane, and therefore the Talbot effect homogenizes the intensity of the periodic input field. The Talbot effect has been used to create uniform grid illuminators [16].

In addition to improving the spot uniformity the Talbot grid can translate a large amount in response to a small angular tilt of the input light field. This property has been used in phase imaging [17, 18]. Mathematically, the translation Δ versus angular tilt θ is given by

$$\Delta = \frac{2d^2}{\lambda}\tan\theta \quad , \tag{4.2}$$

Figure 4.6 shows this angular tilt. To appreciate this phase sensitivity, assume we have a microlens grid with a pitch of 30 μm. The focal length of the microlens is 90 μm. Then only 8.2 mrad will result in a full aperture (30 μm) lateral translation of the first Talbot grid. In comparison, the original focal grid would only shift by 0.73 μm.

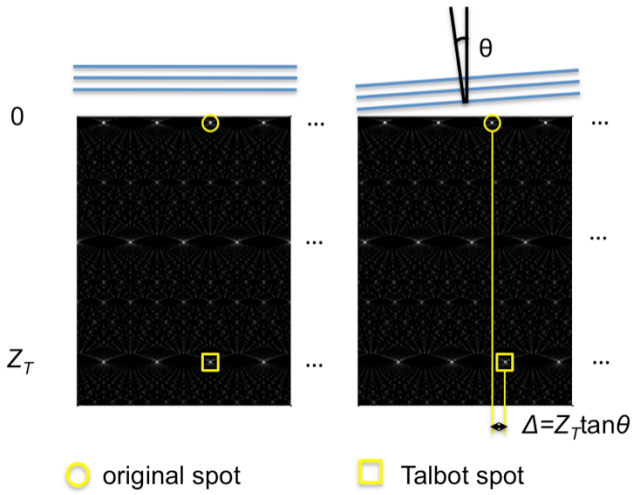

Figure 4.6. Scanning mechanism of Talbot focal grid. With normal incidence illumination, the Talbot focal spot grid is generated right beneath the original focal spot. If the plane wave is tilted by a small angle θ, the Talbot focal grid laterally shifts by $2\tan(\theta)d^2/\lambda$, while the original focal grid shows very little displacement.

4.3 On-chip fluorescence Talbot microscope

In the previous section, we have briefly explained the Talbot effect. The Talbot effect is capable of homogenizing the intensity of the periodic input field. Also the Talbot grid can laterally translate a significant amount in response to a small angular tilt of the input light field.

Based on this phase sensitivity of Talbot effect to the incident field, we can shift the focal spot by changing the incident wave front of a periodic structure. In this section we will introduce the imaging and reconstruction principle of the fluorescence Talbot microscope (FTM).

4.3.1 Principle of the fluorescence Talbot microscope

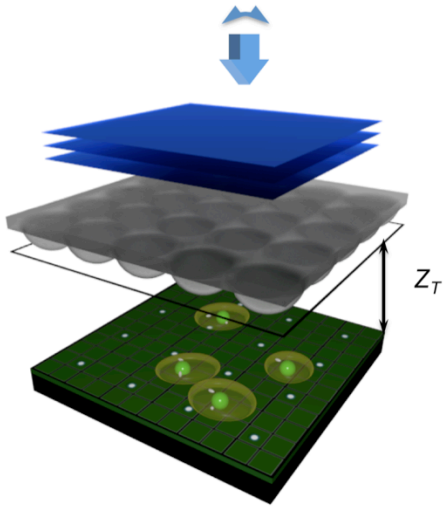

Figure 4.7. The schematic of the FTM system. The microlens array within the Talbot illuminator creates the original focal spot grid. The sample on a filter-coated CMOS sensor is located at the Talbot length z_T away from the original focal grid. The Talbot illuminator sweeps the gradient of the incident planar wave on the microlens array to perform the scanning of the Talbot focal grid.

The FTM method utilizes the Talbot effect to project a grid of focused excitation light spots onto the sample. The sample rests on a filter-coated CMOS sensor chip. Figure 4.7 shows the setup of the system.

Figure 4.8 depicts the reconstruction process. As the Talbot focal grid scans across the sample, the COMS sensor collects the fluorescence emissions associated with each focal spot. Each frame is composed into a sparsely sampled fluorescence image. When the scanning finishes, the imaging sensor has collected a sequence of sparse images. From the fluorescence signal associated with one focal spot, we can reconstruct a regional image. By combining these regional images, we can then reconstruct a filled-in high-resolution fluorescence image.

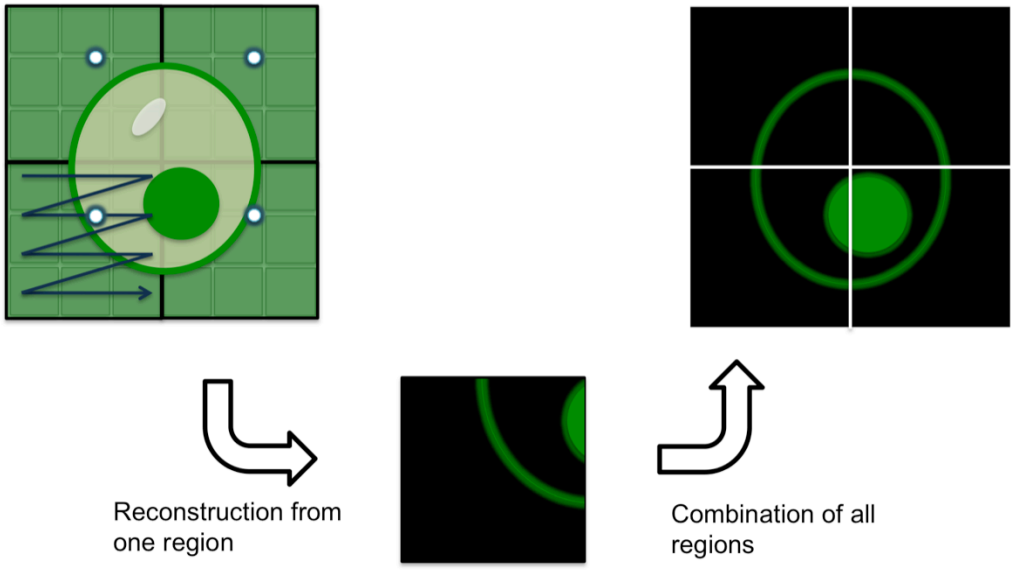

Figure 4.8. Reconstruction of the full-field image. Each Talbot focal spot raster scans a small region. The readout sequence from the sensor pixels under each Talbot focal spot reconstructs a regional fluorescence image. The full-field image is acquired by combining all the regional fluorescence images.

The use of Talbot effect affords a large working distance between the optical illumination elements and the sample. This advantage also distinguishes the FTM method from a non-Talbot approach, which has a much shorter demonstrated working distance (~40 μm) [13]. The FOV of the FTM is directly scalable simply by using a larger microlens grid to create more focal spots and by employing a larger sensor chip for signal collection. In conventional microscopy, where scaling up the FOV requires a larger mechanical scanning range, the image acquisition time is longer.

In the previous section we calculated that only 8.2 mrad will result in a full aperture (30 μm) scan, while the original focal grid would only shift by 0.73 μm. Because the required tilt angle is small, the scan induces little aberration to the Talbot focal grid. The detailed discussion of the aberration aspects will be presented in Chapter 5. In addition, a miniaturized device, such as MEMS mirror, can easily implement this small scanning angle change. This can lead to an inexpensive and portable imaging system.

4.3.2 System setup for on-chip FTM prototype

FTM takes advantage of the recent development and commercialization effort of semiconductor and Micro-electro-mechanical system (MEMS) to reduce the cost [19, 20]. The FTM system consists of two main components: the imaging sensor and the Talbot illuminator. Figure 4.9 shows the setup of the on-chip FTM prototype.

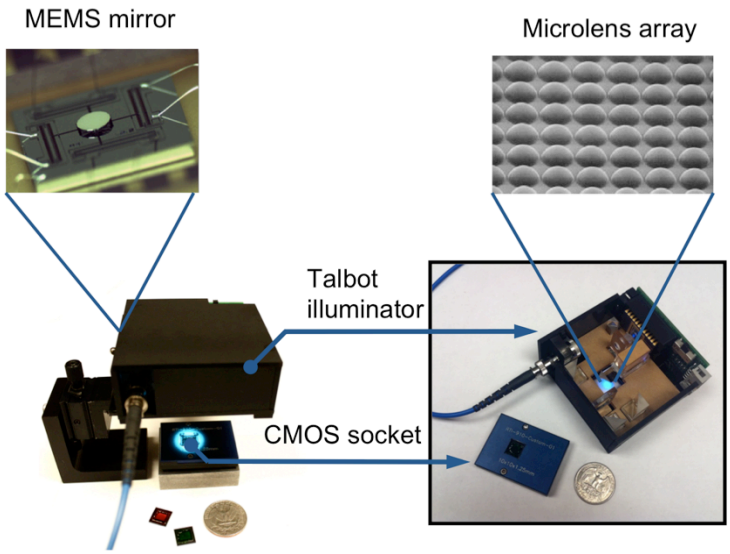

Figure 4.9. Photo of the FTM prototype. The Talbot illuminator and a filter-coated CMOS sensor chip mounted to the readout socket.

The CMOS sensors used in the experiment have a pixel size of 2.2 μm. (MT9P031I12STM, Aptina). The glass cover was removed from each sensor to allow direct sensor surface access. Red and green filter layers were coated on separate CMOS sensors based on the methods in our previous work [10]. The thickness is 8 μm. An extra polydimethylsiloxane (PDMS, Dow Corning) layer with a thickness of 2 μm was then coated on the filter layer for protection.

The Talbot illuminator consists of a microlens array (Suss Micro-optics) and a MEMS mirror (Mirrorcle). The MEMS mirror is a mature and highly reliable optical scanning component that is widely used in portable projectors [20]. The detailed optical setup is shown in Figure 4.10. The 488 nm laser (100 mW, Cyan Scientific Laser, Spectra Physics) was coupled into a single mode fiber and then launched into the Talbot illuminator. A fiber collimator (f = 11 mm, CFC-11X-A – Adj.

Thorlabs) collimated the laser beam and guided to a polarizing beam splitter (PBS051, Thorlabs) and subsequently to the MEMS mirror (3.6 mm diameter, Mirrocle Technologies). A quarter wave plate was rotated to the appropriate angle and placed in between the polarizing beam splitter (PBS) and the MEMS mirror, so that the beam reflected from the MEMS mirror could pass through the beam splitter. Specifically, the linear polarized beam is incident on the PBS, and is reflected to the quarter wavelength wave plate. The linear polarized beam is then transformed to a clockwise circular polarized beam by the quarter wave plate. The circular polarized beam is reflected from the MEMS mirror and the polarization changes to counter clockwise. After passing the quarter wavelength wave plate again, the polarization of beam is transformed back to linear but its direction is perpendicular to the original direction. With this polarization change, the light will then pass through the beam splitter and is incident on the convex lens L1. Two convex lenses L1 (f=10 mm, AC060-010-A, Thorlabs) and L2, (f=50 mm, LA1213-A, Thorlabs) expanded the beam by a factor of 5. The MEMS mirror was set at the back focal plane of L1, and the microlens array was placed at the front focal plane of L2. Thus, the MEMS mirror plane and the microlens array plane are conjugated planes, so that the tilt of the MEMS mirror will not induce any lateral movement of the beam on the microlens array.

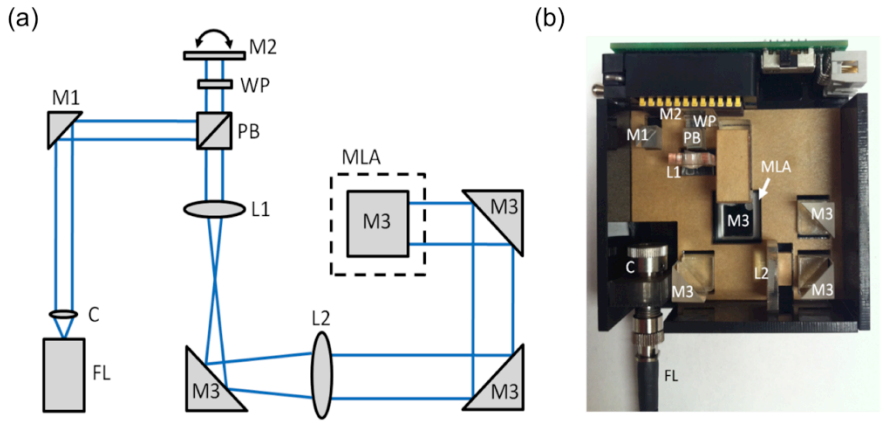

Figure 4.10. Optical setup of Talbot illuminator. (a) The schematic diagrams of the Talbot illuminator setup. C: collimator; FL: fiber laser; L1: Plano-convex lens (f=10 mm); L2: plano-convex lens (f=50 mm); M1: right angle prism mirror; M2: MEMS mirror; M3: right angle prism mirror; MLA: microlens array; PB: polarizing beamsplitter; WP: achromatic quarter-wave plate. (b) The photo of the Talbot illuminator setup. All the optical parts are labeled in accordance with (a).

The microlens array focuses the uniform coherent input beam into a grid of focal spots at a distance of z_f = 90 μm from the microlens array. The separation between adjacent focal spots is equal to the microlens array pitch d =30 μm.

To perform FTM imaging, we place the sample of interest on the filter-coated sensor and align the sample to the first Talbot focal grid. The MEMS Mirror performs a raster scan of the Talbot grid across the sample. The sensor is synchronized with the scan so that a raw image is acquired at each time-point in the scan process.

After performing background subtraction for each raw image, the stack of processed images (local images) is then combined to reconstruct the full-field image. The reconstruction program is implemented in Matlab (Mathworks).

The FTM provides a wide FOV that is limited by the imaging area of the sensor chip and the extent of the Talbot focal grid. In this case the sensor size is the limits of the system FOV, which is 3.9 × 3.5 mm^2 for the prototype.

4.4 Results

To demonstrate that the FTM can be used to image fluorescent biological specimens with microscopic resolution, we first performed full-field FTM imaging of live infected HeLa cell line expressing GFP in the nucleus.

In the experiment, the HeLa cells (ATCC) were infected at approximately 35% confluence with VSVG-pseudotyped lentivirus to obtain cells ubiquitously expressing GFP fused to histone-2B, driven by the chicken beta-actin-CMV (CAG) promoter. Stably infected cells were propagated in DMEM (Cellgro) and supplemented with 10% FBS (Cellgro). Green filter-coated sensors were incubated with gelatin for 6 hours for better cell adhesion. Before imaging, cells were trypsinized (0.05% Trypsin/EDTA, Cellgro), plated onto gelatin-treated sensors and incubated for 12 hours.

The full area of imaging was 3.9×3.5 mm^2 on the CMOS sensor. The scan step size was 0.60 μm in both X and Y directions. The dwell time for the scan step depended on the fluorescent intensity from the sample. With approximately 1 μW on each focal spot, the pixel dwell time for the cell nucleus of HeLa cell was set at 16 ms for sufficient signal collection. The total scan time was 50

seconds. The data readout and storage time for the process, which was mainly limited by the sensor readout speed, was about 4-5 min.

The full field image was reconstructed from a stack of 2500 raw images acquired with 128×114 Talbot focal spots, and the reconstructed image contained 6400×5700 pixels. The image reconstruction time was less than 1 minute and was performed by a 64-bit Windows 7 personal computer with Intel Xeon® 2.5 GHz CPU and 12 GB memory.

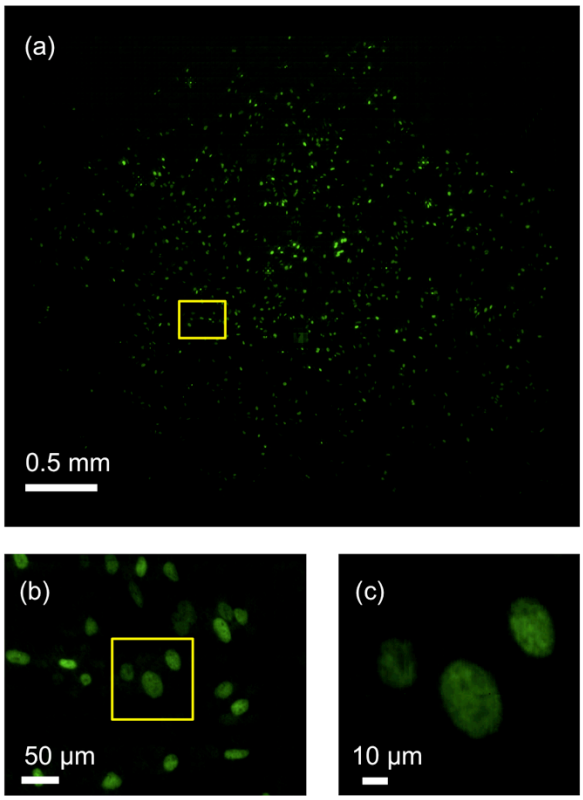

Figure 4.11. Fluorescence image of HeLa cells with GFP expression in nuclei. (a) The full FOV FTM image. (b) The magnified FTM image with a specified rectangle shows the FOV of (a). (c) The magnified FTM image with a specified rectangle shows the FOV of (b)

Figure 4.11 (a) shows the FTM image over the full field of view. Figure 4.11 (b) is a blowup image from the region specified in Figure 4.11 (a), the FOV of which is the same as the FOV of a 20X

microscope objective. The sub-nuclear bodies were discernible from a further enlarged image, shown in Figure 4.11 (c).

Next, we performed full-field FTM imaging of live *C. elegans* expressing GFP in the pharynx. The *C. elegans* strain used in the experiments was PS5643 syIs231 [hs:LIN-3C , myo-2::GFP]; him-5. The worm strain was cultured at 22°C using standard protocols [21]. To have a uniform size distribution of the worm population, we synchronize the worm to L1 stage. The eggs were harvested from PS5643 gravid adults by bleaching and placed on plates, and the worms were allowed to develop at 22°C to L1 stage.

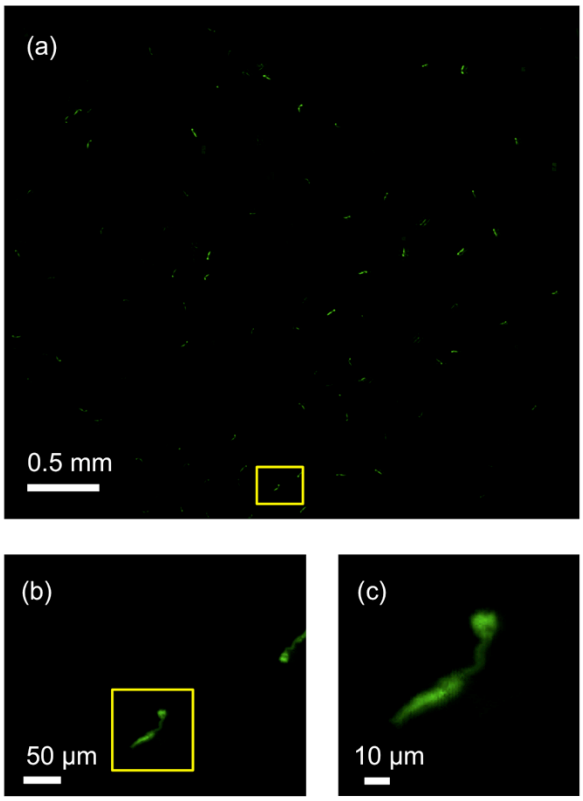

Figure 4.12. Fluorescence image of *C. elegans* (PS5643) with GFP expression in pharynx. (a) The full FOV FTM image. (b) The magnified FTM image with a specified rectangle shows the FOV of (a). (c) The magnified FTM image with a specified rectangle shows the FOV of (b)

The pixel dwell time for the pharynx of *C. elegans* was set at 10 ms. The total scan time was 32 seconds.

Figure 4.12 (a) shows the FTM image over the full field of view. Figure 4.12 (b) is a blowup image from the region specified in Figure 4.12 (a), and a further enlarged image was shown in Figure 4.12 (c).

We also used FTM to image the fixed fluorescence human cancer cells (SK-BR-3), which have cancer marker (Her2) on their membranes labeled by quantum dots (QDots® 625, Life Technologies)

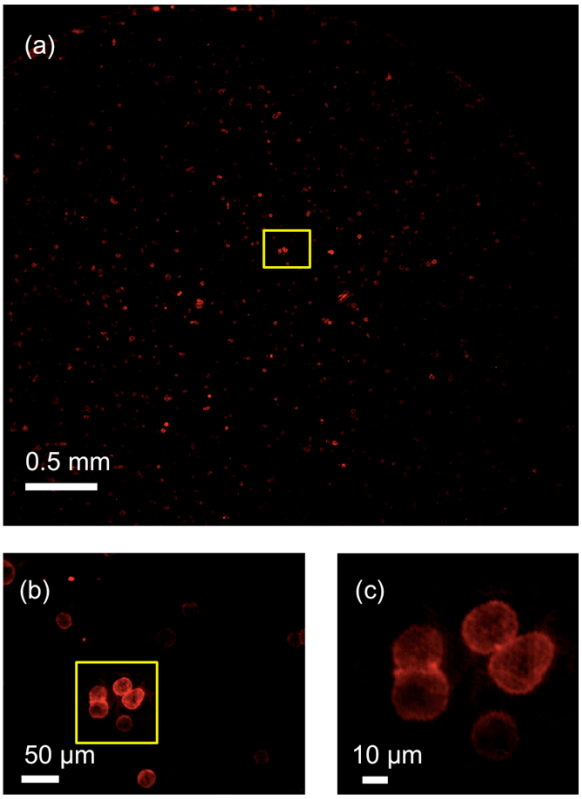

Figure 4.13. Fluorescence images of human breast cancer cells (SK-BR-3) with membranes stained by Qdot® 625. (a) The full field of view (FOV) FTM image. (e) The magnified FTM image with a specified rectangle shows the FOV of (a). (c) The magnified FTM image with a specified rectangle shows the FOV of (b).

The human breast cancer cell line SK-BR-3 was purchased from American Type Culture Collection (ATCC). Cells were cultured at 37 °C, 5% CO2 in McCoy's 5A medium (ATCC) with 10% fetal bovine serum (FBS, Invitrogen). Before the experiment, cells were fixed with 4% formaldehyde for 5 min, and incubated sequentially with mouse anti-HER2 (c-erbB-2) antibody (Invitrogen) for 1 h and 5 nM Qdot® 625 goat F(ab')2 anti-mouse IgG conjugate (Invitrogen) for 1 h, then washed with Dulbecco's phosphate-buffered saline (DPBS, Invitrogen). Before the experiment, cells were mounted on a red filter-coated sensor with a 5 mm-diameter coverslip on top. Mineral oil was then poured around at the edge of the coverslip to avoid evaporation.

The pixel dwell time for the cell membrane of SK-BR-3 breast cancer cell was 12 ms, and the total scan time was about 40 seconds.

Figure 4.13 (a) shows the FTM image over the full field of view. Figure 4.13 (b) is a blowup image from the region specified in Figure 4.13 (a). The further enlarged image is shown in Figure 4.13 (c). The cell membranes were clearly discernible.

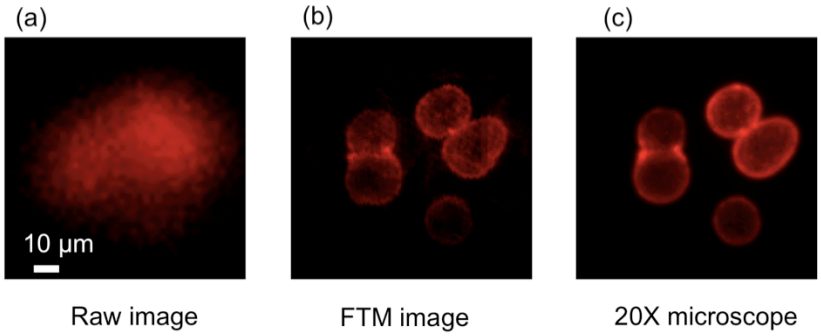

Figure 4.14. Comparison of the FTM image with the conventional microscope image. (a) Low resolution fluorescence image directly acquired by the sensor with uniform illumination. (b) FTM image of the same area as (a). (c) 20X microscope image of the same area. All images are human breast cancer cells (SK-BR-3) with membranes stained by Qdot® 625

Figure 4.14 (a) shows the direct fluorescence collection from the CMOS sensor chip when we applied a uniform illumination. Any structure that was finer than the fluorescence PSF was indistinguishable [7]. Figure 4.14 (b) shows the image acquired by the FTM prototype, the images were comparable with microscope images taken with a 20X objective, shown in Figure 4.14 (c).

4.5 Conclusion

In this chapter we have introduced the FTM method. It utilizes the Talbot effect to project a grid of focused excitation light spots onto the sample. The Talbot focal spot grid scans the sample placed on a filter-coated CMOS sensor chip. The fluorescence emissions associated with each focal spot are collected by the sensor chip and are composed into a sparsely sampled fluorescence image. We could then reconstruct a filled-in high-resolution fluorescence image. In contrast to the conventional microscope, the collection efficiency, resolution, and FOV of this technology are not tied to each other. For FTM, the resolution depends on the Talbot focal spot size, the FOV is related to the extent of the focal spot grid, and the collection efficiency is related to the physical proximity of the fluorescence sites to the sensor pixels. In the next chapter we will quantify the resolution and collection efficiency of the FTM prototype.

REFERENCES

1. M. Totzeck, W. Ulrich, A. Göhnermeier, and W. Kaiser, "Semiconductor fabrication: Pushing deep ultraviolet lithography to its limits," *Nature Photonics* **1**, 629-631 (2007).
2. K. H. Chung, M. M. Crane, and H. Lu, "Automated on-chip rapid microscopy, phenotyping and sorting of *C. elegans*," *Nature Methods* **5**, 637-643 (2008).
3. H. K. Lin, S. Y. Zheng, A. J. Williams, M. Balic, S. Groshen, H. I. Scher, M. Fleisher, W. Stadler, R. H. Datar, Y. C. Tai, and R. J. Cote, "Portable filter-based microdevice for detection and characterization of circulating tumor cells," *Clinical Cancer Research* **16**, 5011-5018 (2010).
4. B. Neumann, M. Held, U. Liebel, H. Erfle, P. Rogers, R. Pepperkok, and J. Ellenberg, "High-throughput RNAi screening by time-lapse imaging of live human cells," *Nature Methods* **3**, 385-390 (2006).
5. R. A. Hoebe, C. H. Van Oven, T. W. J. Gadella, P. B. Dhonukshe, C. J. F. Van Noorden, and E. M. M. Manders, "Controlled light-exposure microscopy reduces photobleaching and phototoxicity in fluorescence live-cell imaging," *Nature Biotechnology* **25**, 249-253 (2007).
6. "Hamamastu NanoZoomer 2.0-HT Catalog," http://jp.hamamatsu.com/resources/products/sys/pdf/eng/e_ndp20.pdf.
7. A. F. Coskun, I. Sencan, T. W. Su, and A. Ozcan, "Lensfree fluorescent on-chip imaging of transgenic *Caenorhabditis elegans* over an ultra-wide field-of-view," *Plos One* **6** (2011).
8. L. B. Lucy, "An iterative technique for the rectification of observed distributions," *The Astronomical Journal* **79**, 745 (1974).
9. D. L. Donoho, "Compressed sensing," *IEEE Transactions on Information Theory* **52**, 1289-1306 (2006).
10. S. Pang, C. Han, L. M. Lee, and C. H. Yang, "Fluorescence microscopy imaging with a Fresnel zone plate array based optofluidic microscope," *Lab on a Chip* **11**, 3698-3702 (2011).
11. J. Wu, X. Cui, G. Zheng, Y. M. Wang, L. M. Lee, and C. Yang, "Wide field-of-view microscope based on holographic focus grid illumination," *Optics Letters* **35**, 2188-2190 (2010).
12. J. G. Wu, G. A. Zheng, Z. Li, and C. H. Yang, "Focal plane tuning in wide-field-of-view microscope with Talbot pattern illumination," *Optics Letters* **36**, 2179-2181 (2011).
13. A. Orth, and K. Crozier, "Microscopy with microlens arrays: high throughput, high resolution and light-field imaging," *Optics Express* **20**, 13522-13531 (2012).
14. B. Hulsken, D. Vossen, and S. Stallinga, "High NA diffractive array illuminators and application in a multi-spot scanning microscope," *Journal of the European Optical Society-Rapid Publications* **7**, 12025, 2026 (2012).
15. H. F. Talbot, "LXXVI. Facts relating to optical science. No. IV," *The London and Edinburgh Philosophical Magazine and Journal of Science* **9**, 401-407 (1836).
16. A. W. Lohmann, and J. A. Thomas, "Making an array illuminator based on the Talbot effect," *Applied Optics* **29**, 4337-4340 (1990).
17. A. W. Lohmann, and D. E. Silva, "An interferometer based on the Talbot effect," *Optics Communications* **2**, 413-415 (1971).
18. F. Pfeiffer, T. Weitkamp, O. Bunk, and C. David, "Phase retrieval and differential phase-contrast imaging with low-brilliance X-ray sources," *Nature Physics* **2**, 258-261 (2006).
19. A. El Gamal, and H. Eltoukhy, "CMOS image sensors," *IEEE Circuits & Devices* **21**, 6-20 (2005).

20. M. Freeman, M. Champion, and S. Madhavan, "Scanned laser pico-projectors: Seeing the big picture (with a small device)," *Optics and Photonics News* **20**, 28-34 (2009).
21. S. Brenner, "The genetics of *Caenorhabditis elegans*," *Genetics* **77**, 71 (1974).

C h a p t e r 5

SYSTEM CHARACTERIZATIONS OF THE FLUORESENCE TALBOT MICROSCOPE PROTOTYPE

In Chapter 4, we introduced the Talbot Effect and described the operation principle of the fluorescence Talbot microscope (FTM). We further demonstrated the imaging capability of a prototype of FTM. In this chapter we aim to characterize several key parameters of the FTM prototype. In the first section we will establish the resolution of the FTM prototype through both numerical simulation and experiment. In the second section we will describe experimental methods to quantify the collection efficiency of the FTM prototype, and show the advantage of on-chip fluorescence collection efficiency compared with that of a traditional microscope objective. The measurement in this chapter is limited to the FTM prototype described in Chapter 4. We note here that this prototype does not reach the theoretical limit of the FTM method. We will discuss the potentials of the FTM method in Chapter 8.

5.1 Resolution of the FTM prototype

As discussed in the previous chapter, the resolution of the FTM is determined by the spot size of the Talbot focal spot. We can consider the Talbot illumination as a special case of structure illumination. The upper limit of the detectable frequency of the FTM image is the highest frequency component that can be generated from the Talbot focal spots. The quantification of the Talbot focal spot quality will determine the highest achievable resolution that is limited by the FTM prototype. This information will provide us a point of reference for choosing the step size for the raster scan.

In this section, we will first perform the numerical simulation to estimate the intensity profile of the Talbot focal spots. Next we will discuss the effect on the Talbot focal spots quality of tilting the incident angle. Finally we will demonstrate how we established the resolution experimentally by imaging the resolution target fabricated on a CMOS sensor.

The microlens grid used in the FTM prototype was purchased from Suss MicroOptics (part number 18-00025). The pitch of the microlens grid is 30 μm. The microlens is plano-convex shaped, and the radius of the curvature is 42 μm. The microlens grid is made of fused silica, which has a refractive

index of 1.461 at wavelength of 500 nm. The focal length of the microlens is ~95 μm, and the N.A. is ~ 0.15.

5.1.1 Numerical simulation of the focal spot quality of the Talbot image

Because the N.A. of the microlens is relatively small (~0.15), simulations based on scalar wave theory can give accurate results of the profile of Talbot focal spots [1]. First we exam the quality of the Talbot effect under perpendicular illumination, i.e. the light incident at 0 mrad angle to the microlens array. In the simulation the wavelength is set to 488 nm, the microlens parameters are as above. The Talbot distance is 3.69 mm.

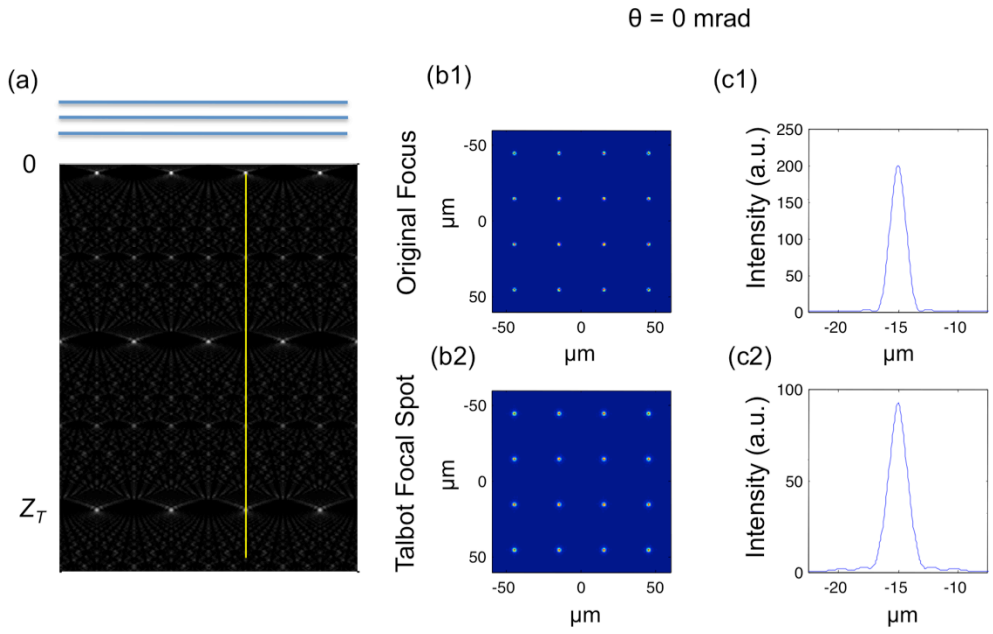

Figure 5.1. The simulation of the focal spot grid and its Talbot self-images with perpendicular illumination (incident angle of 0 mrad). (a) The z plane cross-section view. (b) The focal spot intensity on the lateral plane for the original focal plane (b1) and the Talbot focal plane (b2). (c) The intensity profile of one focal spot in on the original focal plane (c1) and the Talbot focal plane (c2).

Figure 5.1 (a) shows the cross-section of the intensity profile along the propagation direction. The bright spots at $z = 0$ are the original focal spots. At distance $z = z_T$, the Talbot focal spots are right underneath the original focal spot. The yellow vertical line indicates this alignment.

Figure 5.1 (b1) shows the intensity distribution of a four-by-four original focal spots grid. Figure 5.1 (c1) shows the profile of one original focal spot. The FWHM of the focal spot is 1.25 μm. Under perpendicular illumination the FWHM of the Talbot focal spot is 1.28 μm, as shown in Figure 5.1 (b2) and (c2). This indicates that the focal quality of the original focus can be well maintained.

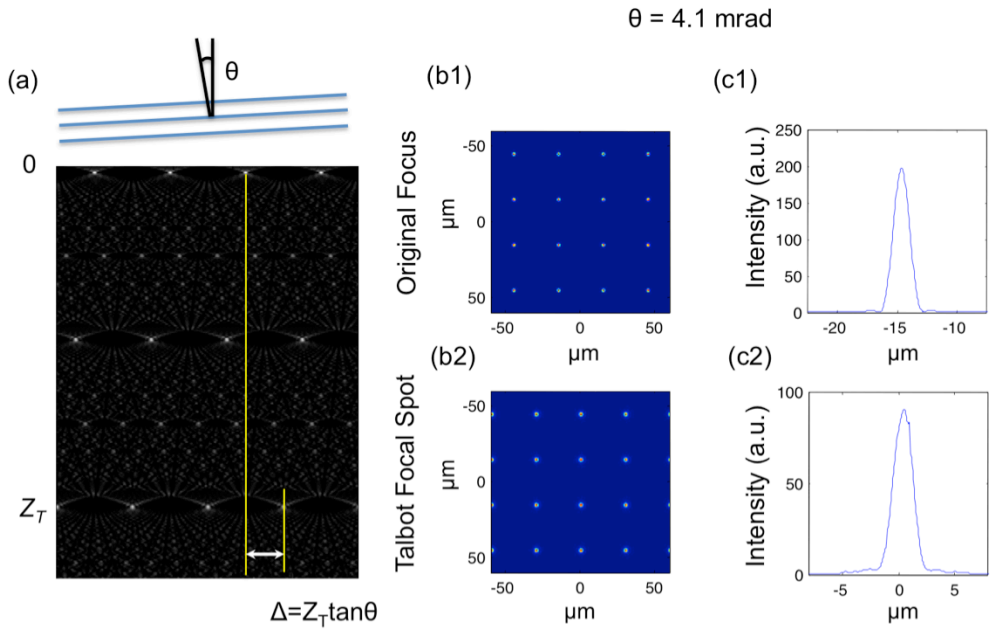

Figure 5.2. The simulation of the focal spot grid and its Talbot self-images with incident angle of 4.1 mrad. (a) The z plane cross-section view. (b) The focal spot intensity on the lateral plane for the original focal plane (b1) and the Talbot focal plane (b2). (c) the intensity profile of one focal spot in on the original focal plane (c1) and the Talbot focal plane (c2).

To be able to perform a full-field scan with the Talbot focal spots with this resolution, the focal spot should be able to shift half the pitch of the microlens array without deterioration of the quality of the focal spot. The incident angle θ_{max} needed for the half pitch scan is:

$$\theta_{\max} = \tan^{-1}(\lambda / 4d), \tag{5.1}$$

Where λ is the wavelength of the incident light, and d is the pitch of the microlens array. The calculated θ_{max} is 4.1 mrad.

Figure 5.2 (a) shows the simulation results of the intensity profile cross-section along the propagation direction with an incident angle of 4.1 mrad. The Talbot focal spots array has a lateral shift of half the pitch of the microlens array, which is indicated by the yellow lines in the figure.

Figure 5.2 (b1) shows the intensity distribution of a four by four original focal spots grid with an incident angle of 4.1 mrad. Figure 5.2 (c1) shows the profile of one original focal spot. As the incident angle is very small we observed that the FWHM of the original focal spot is 1.25 μm, the same as that with perpendicular incidence. The FWHM of the Talbot focal spot is 1.30 μm, as shown in Figure 5.2 (b2) and (c2). This FWHM only increased by 0.02 μm, compared with the FWHM of 1.28 μm with perpendicular incidence, which verified that with the small tilt angle the quality of the Talbot focal spot is maintained when the spot array shifts by a half pitch.

5.1.2 Experimental measurement of the resolution of the FTM prototype

To experimentally verify the resolution of the FTM prototype, we fabricated a resolution target that is similar to the USFA resolution target on a CMOS sensor. The glass cover of a CMOS imaging sensor (MT9P031I12STM, Aptina) was first removed to allow the direct sensor access. A layer of SU-8 photo-resist (2010, Microchem) of 10 μm was spin coated on to the sensor to match the thickness of the filter layer. The exposure and curing procedures followed the protocol from the manufacturer [2]. A thermal evaporator deposited a 100 nm aluminum layer on to the sensor. A focused ion beam (FIB) machine (Nova 600, FEI) milled the resolution target pattern on the aluminum layer. Figure 5.3 shows the FIB image of the fabricated resolution target.

We patterned the resolution target with line widths of 3 μm , 2 μm , 1.5 μm , 1.4 μm , 1.3 μm , 1.2 μm , 1.1 μm , and 1.0 μm. The opaque width between the lines was same as the line width. We also patterned an open window with the size of 50 μm by 50 μm . This opening was used later for tracking the scanning of the Talbot focal spot.

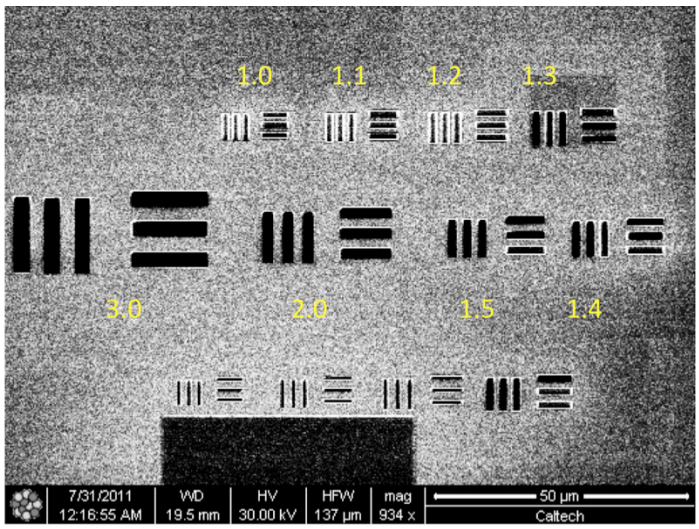

Figure 5.3. Focused ion beam (FIB) image of the resolution target fabricated on a CMOS imaging sensor with resolution marks.

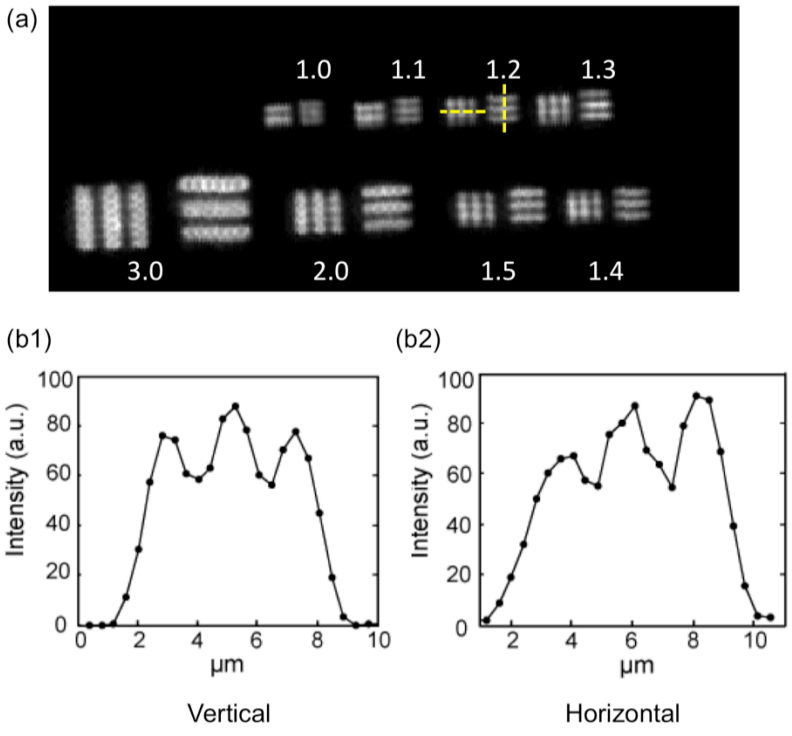

Figure 5.4. Resolution of the FTM prototype. (a) The FTM image of the resolution target. The achieved resolution is 1.2 µm. (b) The cross-section line trace from the FTM image of the horizontal (b1) and vertical (b2) marks of 1.2 µm.

The numerical simulations in the previous section suggest that the FWHM of the Talbot focal spot is about 1.3 μm. Therefore, the sampling step size defined by Nyquist sampling theorem is ~0.7 μm [3]. For the actual scanning of the resolution target, we chose the FTM scan step size to be 0.25 μm for imaging. This step size is much smaller than the sampling step size defined by Nyquist sampling theorem, in order that the resolution would be only limited by the optical resolution of the Talbot focal spots. Figure 5.4 (a) shows the image of the resolution target scanned by the FTM prototype.

The minimal discernable line width is 1.2 μm. Figure 5.4 (b1) and (b2) shows the profiles of line traces from the vertical, and horizontal scans of the 1.2 μm target, respectively. In this experiment, we established that the resolution of the FTM prototype was 1.2 μm . Therefore in the experiments we chose the step size to be 0.6 μm to satisfy the Nyquist sampling criteria.

5.2 Collection efficiency of the FTM prototype

As mentioned in Chapter 1, in an aberration-corrected conventional microscope objective, the resolution is correlated to the collection efficiency through the N.A. The resolution of the FTM prototype is determined by the Talbot focal spot size, as discussed in the previous section, and the collection efficiency is determined by the collection geometry of the on-chip setup.

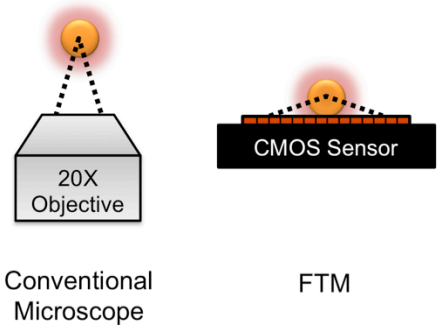

Figure 5.5. Collection geometry of a conventional microscope objective compared with that of an FTM.

For a conventional microscope, without taking loss from the refractive surfaces into account, by calculating the solid angle of the collection defined by the N.A., a 20X/0.4 N.A. objective can collect only 4.2% of the total fluorescence. Figure 5.5 compares the collection geometry of a microscope objective with the on-chip collection geometry of the FTM prototype.

The sample sits right on top of the filter coated CMOS sensor. Ideally the sensor will be able to collect all the fluorescence emitting to the bottom hemisphere, which is 50% of the collection efficiency. However, in practice, to avoid the cross-talk from the regions of adjacent Talbot focal spots, the pitch of the focal spot grid places a limit on the collection area for fluorescence excited by one focal spot. Also due to the thickness of the filter layer, the sample is about 10-20 μm above the sensor surface. We can estimate the on-chip fluorescence collection efficiency by considering that the fluorescence from a single Talbot focal spot was collected from an area covering 12×12 pixels (26.4×26.4 μm^2), which is less than the area taken by an individual microlens (30×30 μm^2). The separation between the fluorophores and sensor was 15 μm. Calculating according to this collection geometry the FTM prototype collects ~12.5% of the total fluorescence, equivalent of 0.67 N.A. microscope objectives. This collection efficiency is about three times greater than that of the 0.4 N.A. microscope objectives.

The high collection efficiency implies that to measure the same amount of fluorescence signal, we can excite the fluorescently labeled sample with a lower intensity, which will reduce the photo-bleaching rate [4]. In this section we will compare the fluorescence decay due to photo-bleaching with the FTM prototype and conventional microscope objectives with different N.A.s. These experiments will help us establish the collection efficiency experimentally.

5.2.1 System setup and calibration

We built a system to compare the photo-bleaching rate of a sample with the same fluorescence labeling with a conventional 20X/0.4 N.A. microscope objective (Olympus) and a filter coated CMOS sensor. Because the illumination systems are different in the two systems, we first calibrated the excitation intensity and exposure time in the conventional microscope to match the detected fluorescence signals from FTM.

Figure 5.6 shows the system setup. We used the same filter-coated CMOS sensor in both the conventional microscope (C1) and the FTM prototype (C2) to ensure the same sensor sensitivity.

The epi-illumination microscope system (BX41, Olympus) for comparison was equipped with a 20X objective (0.4 N.A. Plan, Olympus), and a 488 nm fiber laser (FTECH 488, Fiberoptics) for excitation. SK-BR-3 cells labeled with QDots, which has very high resistance to photo-bleaching, were imaged to calibrate the conventional microscope and the FTM system.

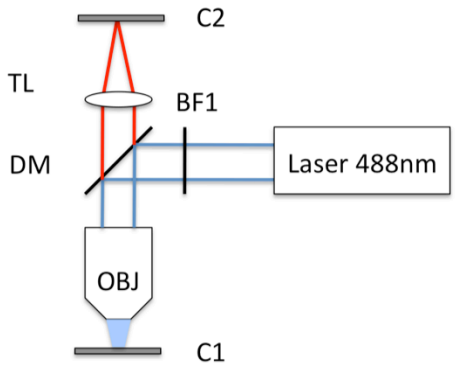

Figure 5.6. System setup for comparison of the microscope objectives and FTM collection geometry. BF1: excitation band pass filter. C1: CMOS sensor with calibration Quantum Dots sample. C2: CMOS sensor with a red coating observing the sample through a microscope. DM: dichroic mirror. OBJ: 20X 0.4 N.A. microscope objectives. TL: tube lens.

The sample dwell time was 12 ms at each focus spot position for FTM imaging. For the conventional microscope measurements, the same SK-BR-3 cell samples on the sensor C1 were imaged by the 20X 0.4 N.A. microscope objective. The exposure time was set from 1 to 3 sec with 200 ms step size. The exposure time of 2.4 seconds from the conventional microscope measured the same fluorescence signal as the FTM system.

This benchmarking method allowed us to do the subsequent direct comparison of the photo-bleaching rate for samples in the FTM and conventional microscope system without requiring direct measurements of the excitation light field intensities and the various light loss mechanisms in the two systems.

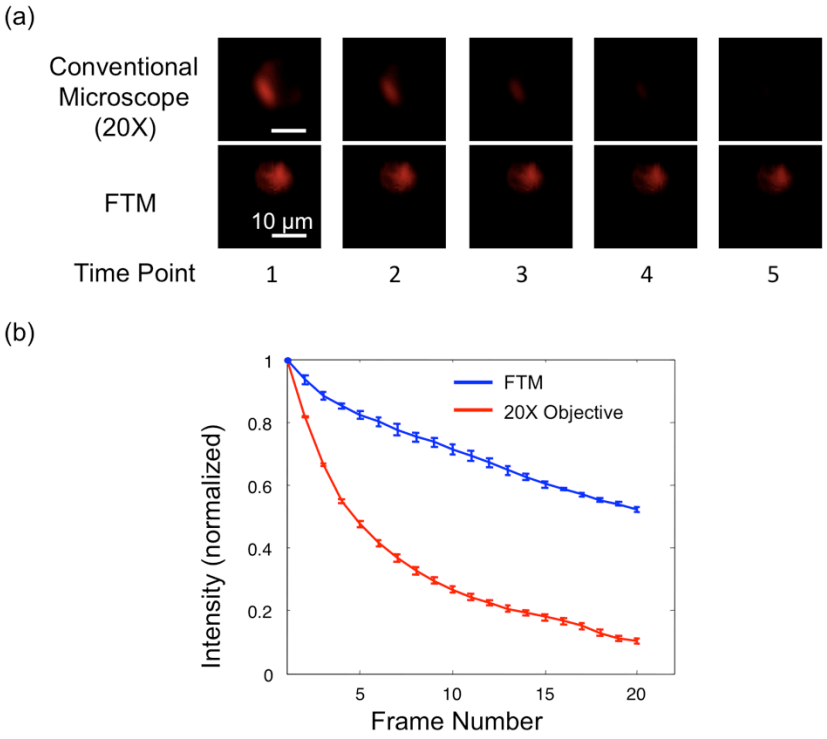

Figure 5.7. Collection efficiency comparison between an FTM and a 20X/0.4 NA microscope objective. (a) The image sequences of human embryonic kidney (HEK) cell membrane stained by LavaCell™ at the first five time points by FTM and a conventional microscope with a 20X 0.4 N.A. objective. (b) The fluorescence photo-bleaching decay curve. Intensities have been normalized to the starting signal intensity in each case.

5.2.2 Photo-bleaching rate comparison between microscope objectives and the FTM

FTM and the conventional microscope each take an image sequence of human embryonic kidney (HEK) cells with membrane labeled by LavaCell™ (Active Motif) at 20 sequential time points. To label LavaCell™ cell membrane, a cultured human embryonic kidney cell line HEK-293 was incubated in DPBS solution with LavaCell™ (15004, Active Motif) for 15 min.

Figure 5.7 (a) shows the images taken by FTM and 0.4 N.A. microscope objectives for the first five time points. Figure 5.7 (b) shows the photo-bleaching decay curves by averaging the intensity from three regions selected from all time points. The photo-bleaching rate was calculated by fitting the

normalized fluorescence decay curve to the exponential functions $e^{-k(n-1)}$, where n is time point and k is the photo-bleaching rate. The fluorescence decay rate in the FTM system was 3.6 times slower than the 0.4 N.A. microscope objective. Experimental collection efficiency values were inversely proportional to the photo-bleaching rates. Therefore the collection efficiency of the FTM is 3.6 times greater than that of the conventional microscope using a 20X/0.4 N.A. objective.

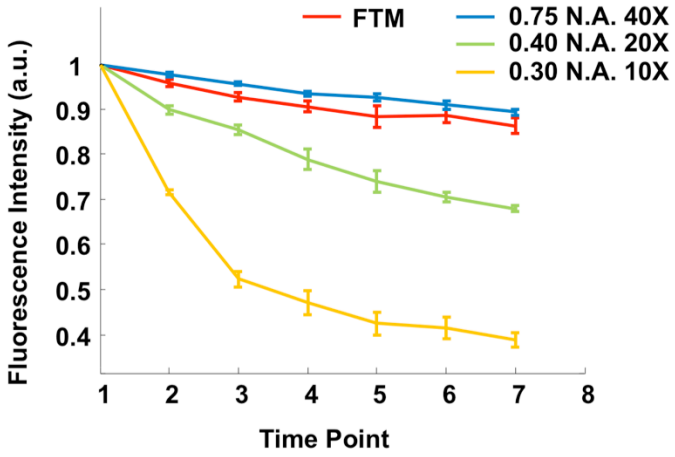

Figure 5.8. Quantification of fluorescence collection efficiency by comparing the photo-bleaching rate of the fluorophore Lavacell™ between the FTM and different microscope objectives.

Table 5.1. Collection efficiency of microscope objectives and the FTM prototype

	0.3 N.A.	0.4 N.A.	0.75 N.A.	FTM
Normalized calculated collection efficiency[1,2]	0.55 (2.30%)	1.00 (4.17%)	4.05 (16.9%)	2.97 (12.4%)
Normalized experimental collection effeciency[1,3]	0.44	1.00	3.65	3.60

[1] The collection efficiency values are normalized to the 0.4 N.A. objective.

[2] The absolute collection efficiency values are in the parentheses.

[3] Experimental collection efficiency values are inversely proportional to the photo-bleaching rates.

We used the same setup to further compare the FTM system with microscope objectives of N.A. of 0.3 and 0.75. The exposure times were set for 340 ms and 19.7 s for 0.75 N.A. and 0.3 N.A. microscope objectives respectively. The result showed that the fluorescence decay in the FTM system was slightly faster (≤ 2%) than the microscope objective with 0.75 N.A. and 8.3 times slower than the objectives with 0.3 N.A. (Figure 5.8), which is in agreement with the collection efficiency calculation based on collection geometry (Table 6.1). This implies that the collection efficiency of the FTM is similar to an objective with an N.A. of ~0.7.

5.3 Conclusion

In this chapter, we have characterized the resolution and the collection efficiency of the FTM prototype. The resolution of the FTM is determined by the Talbot focal spot size. The half pitch scan of the Talbot focal spot requires very small tilt angle, which does not deteriorate the quality of the focal spot. The experimentally established resolution is 1.2 μm . The collection efficiency of the on-chip detection can achieve collection efficiency equivalent to a 0.7 N.A. microscope objective. Comparing the photo-bleaching rate of the LavaCell^{TM} stained HEK cell sample to the FTM prototype and the conventional microscope objective with 0.4 N.A. We observed a 3.6 times slower photo-bleaching decay rate.

REFERENCES

1. J. W. Goodman, *Introduction to Fourier optics* (Roberts & Company Publishers, 2005).
2. "SU-8 2000 Data Sheet (2000.5-2015) - MicroChem," http://microchem.com/pdf/SU-82000DataSheet2000_5thru2015Ver4.pdf.
3. A. V. Oppenheim, R. W. Schafer, and J. R. Buck, *Discrete-time signal processing* (Prentice hall Englewood Cliffs, NJ:, 1989).
4. J. Pawley, *Handbook of biological confocal microscopy* (Springer, 2006).

Chapter 6

MULTICOLOR FLUORESCENCE IMAGING BASED ON THE FLUORESCENCE TALBOT MICROSCOPY METHOD

In Chapter 4 and Chapter 5 we described the imaging principle and the implementation of a chip-scale fluorescence Talbot microscope. The capability of performing multicolor fluorescence microscopy imaging over a wide field-of-view (FOV) is important in screening and pathology applications. Due to the limitation of the choices of absorption filter layer, it is challenging to perform multicolor fluorescence imaging on-chip. In this chapter we will describe an "off-chip" version of FTM system that can achieve wide FOV multicolor fluorescence imaging. The prototype system achieved an FOV of 12 × 10 mm^2 at an acquisition time as fast as 23 s for one fluorescence channel, with a resolution at 1.2 μm. The prototype was used to image green fluorescence beads and double stained human breast cancer cell line SK-BR-3. This imaging method is scalable and simple for implementation of high-speed wide FOV fluorescence microscopy.

6.1 Introduction

As mentioned in previous chapters, fluorescence imaging plays a vital role in modern clinical diagnosis and biological research. Fluorescent probes can bind to target proteins with high specificity, and the multicolor fluorescence microscope enables us to simultaneous visualize multiple protein interactions in living cells [1]. Multicolor fluorescent staining also provides higher contrast for tissue imaging in pathology [2], and reveals the neuronal subsets in small animals [3]. In the abovementioned applications, a large imaging area is often required.

The conventional fluorescence microscope is limited by its FOV. The most common method to increase the FOV of the fluorescence microscope is by translating the sample under a conventional microscope objective [4]. In this method, the time spent on the step motion and focus readjustment is longer than the imaging time. The state-of-the-art commercialized slide scanners use time delayed integration (TDI) cameras, so that a continuous scan can be applied in one scan direction, while the step movement is still required in the other direction [5]. This effort can reduce the full field imaging time, yet the TDI camera is not common in most labs.

Instead of using a microscope objective, recent works have demonstrated using a point scan to improve the scanning speed [6-13]. In these methods, an grid of focal spots is generated by a grid of

microlenses [10, 11], a diffractive optical element [12], or a hologram plate [6]. The dimension of the focal spot grid can be designed to be much larger than the FOV of a microscope objective (< 1 mm), and even larger than standard microscope slides (~15 mm). As the sample is transported by a mechanical stage, the focal spot grid scans across the sample and a relay optics system collects the fluorescence emission from each focal spots to form the full FOV image. A raster scan scheme can be used in these methods to eliminate the step motion of the translational stage, and thus increase the imaging speed.

Instead of using the focal spots directly generated by a microlens grid for wide FOV imaging, using the Talbot effect provides a long working distance for easy sample mounting [7-9] and generates more uniform intensities among focal spots [14]. The phase sensitivity of the Talbot effect can be applied in chip-scale imaging [8, 9]. In these systems, the sample was directly placed on an imaging sensor. The sample mounting is not a standard preparation procedure, and it is difficult to image the fluorescent sample with multiple staining, due to the limitations of the transmission spectrum of the fixed filter on chip. In this chapter, we describe a system that is based on fluoresencence Talbot microscope methods for wide FOV microscopy imaging of multicolor fluorescence samples using relay optics.

As mentioned in Chapter 4, the angular scanning scheme of the immediate focal spot grid is questionable due to the off-axis aberration. The angle of the view of a conventional microscope is usually less than 4°, which means to preserve the image quality, the tilt angle in the conventional microscope should be less than this field angle [16]. In the scanning scheme using a microlens grid, the focal spot needs to shift a distance of a half pitch of the microlens grid in order to perform the whole area scan. For a typical microlens grid with a 30 μm pitch and a typical focal lens of 70 μm this means that the tilt angle needs to be 12° (0.21 rad). Under this this tilt angle, the focal spot is distorted by the off-axis aberration. Figure 6.1 (b1, b2) shows the scalar wave simulation of the point-spread function (PSF) of the focal spot when it is shifted by a half pitch. From the results, we can see that the full width at half maximum (FWHM) of the focal spot along the shift direction was 1.8 μm, which suggests scanning with the original spot would introduce a significant distortion, and is therefore not a suitable method for imaging applications.

Instead of scanning with the original spot, alternatively, we could shift the focal spot generated by the Talbot effect [16, 17]. Mathematically, the translation, Δ, versus angular tilt, θ, is given by

Equation 4.2. The required angle tilt is $\theta = \tan^{-1}(\lambda/4d)$ for the Talbot spot to move a half pitch $d/2$. If we use the microlens array parameters mentioned above, the tilt angle is only 4.1 mrad, which is 50 times smaller than the tilt angle needed to shift the original focal spots. Figure 6.1 (b3, b4) shows the PSF of the Talbot focal spot under the shift. The simulation results show that the full-width at half-maximum (FWHM) of the Talbot focal spot is 1.3 μm. This suggests that using Talbot focal spot grid is a feasible way to perform wide FOV imaging.

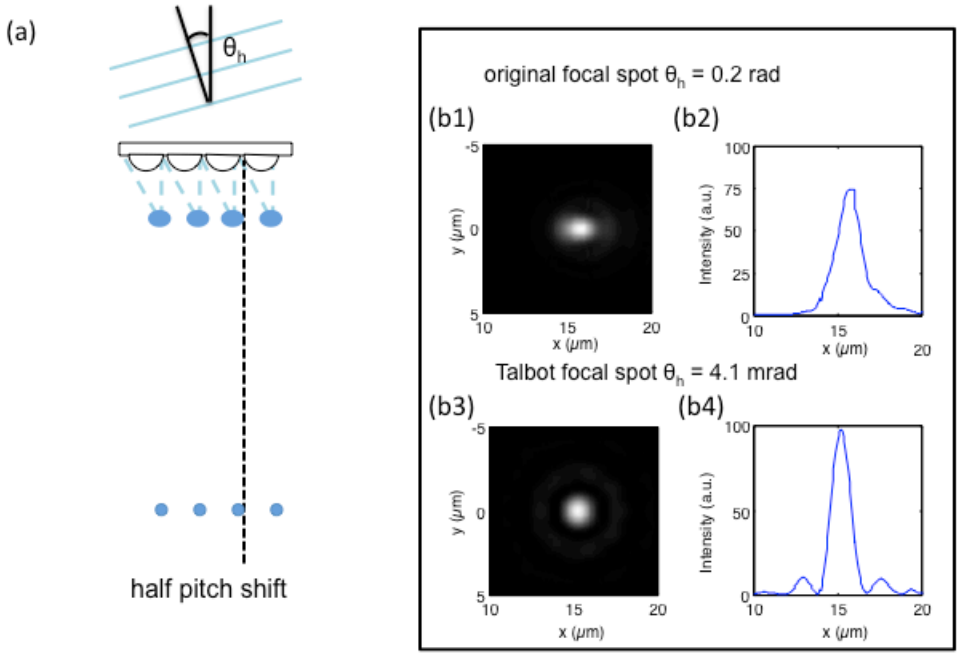

Figure 6.1. Comparison of scanning with the original focal grid and with the Talbot focal grid. (a) By tilting the incident beam angle, the original focal spots generated by the microlens array and Talbot focal spots can be shifted for scanning. (b) Simulated focal spot intensity profile at the tilt angle of a half pitch shift of 15 μm in this case. The angle needed for a half pitch shift for the original focal spot was 0.2 radians and the focal spot was affected by the off-axis aberration (b1,2). The angle needed for a half pitch shift for the Talbot focal spot is 0.2 radian and the focal spot maintains good quality (b1,2).

To perform Talbot focal spot scanning, we only need a mirror to angularly tilt the incident beam to the microlens grid and place the sample at the Talbot distance. When the Talbot focal spot grid

scans across the sample, the locally excited fluorescence can be collected and the full FOV image is reconstructed.

In the following sections we will describe the setup of the system and the quantification of the system resolution and imaging depth. Then we will demonstrate the imaging capability of the system with a double stained SK-BR-3 sample.

6.2 System setup for muilticolor fluorescence Talbot microscope

The Figure 6.2 shows the setup for generating Talbot illumination. The 488 nm laser (Newport Cyan 100mW) was expanded by a telescope system. Two plano-convex lenses L1, (Thorlabs, f1= 25.4 mm), and L2 (Thorlabs, f2=125 mm) expanded the beam ~5 times to fill the aperture of the MEMS mirror (Mirrocle, 5.0 mm diameter). A polarization sensitive beam splitter (PBS, Thorlabs) directed the beam to the MEMS mirror.

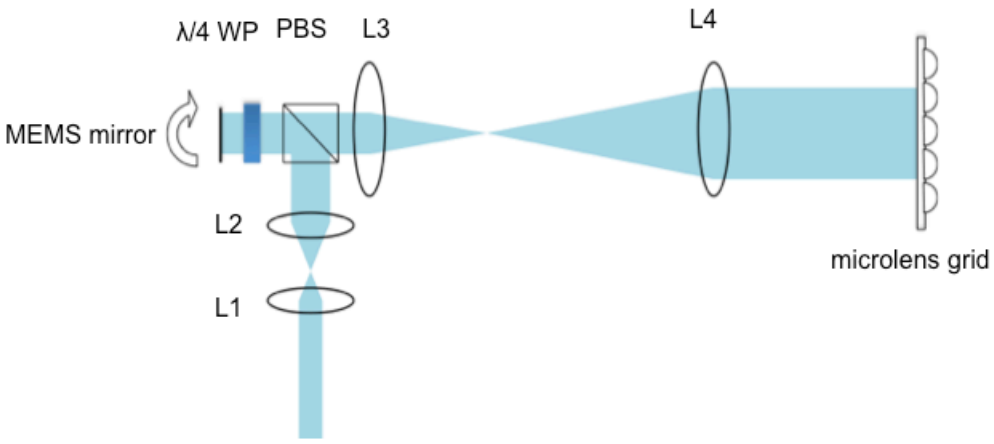

Figure 6.2. The optical setup for generating angular tilted incident beam to the microlens grid. L1 (f=25.4mm) and L2 (f=125mm) expand the beam to fit the MEMS mirror diameter. After the beam passes through the PBS (polarized beam spliter) and λ/4 WP (quarter wave plate), the beam was further expanded by L3 (f=50mm) and L4 (f=400 mm).

A quarter wave plate was inserted in between the MEMS mirror and the PBS. The quarter wave plate transformed the linear polarized beam to a circular polarized beam. The beam reflected by the mirror altered the rotation direction of the circular polarized beam, and the quarter wave plate converted the beam to a linear polarized beam with direction orthogonal to the original beam. This

polarization change allowed the beam pass through the PBS. The beam was further expanded by two lenses L3 (Thorlabs, f = 50 mm) and L4 (Thorlabs, f = 400 mm) and is incident on the microlens grid (Suss MicroOptics, pitch 30μm). To perform wide FOV imaging, we used a large microlens grid with area of 40 × 40 mm^2. This secondary expansion make the final beam diameter to be ~40 mm. The MEMS mirror was placed on the front focal plane of L3, and the microlens grid was placed on the back focal plane of L4. Because the MEMS mirror and the microlens grid were on conjugate planes, the tilt of the MEMS mirror would only change the incident angle to the microlens grid but not induce the beam shift on the microlens grid.

Figure 2(b) shows the system setup for fluorescence collection. The sample on a microscope slide was placed at one Talbot distance away from the microlens focal spot grid. To collect the fluorescence emission from the sample, two single-lens reflex (SLR) camera lenses served as a 1:1 relay system (Nikon Nikkor 50 mm f/1.2). The collection efficiency of the SLR camera lenses was equivalent to 0.4 N.A. The CMOS camera (Teledyne DALSA, Falcon2 4M) has a pixel size of 6 μm. The resolution on the collection side, according to Nyquist sampling criterion, was only 12 μm. However, this is does not determine the FTM image resolution, which depends on the Talbot focal spot size. The imaging area of the CMOS camera is 14 × 10 mm^2, which determines the FOV of the system. The interference filter is inserted in between the two camera lenses. In this setup, the filter can be changed easily for imaging of samples tagged with multicolor fluorophores.

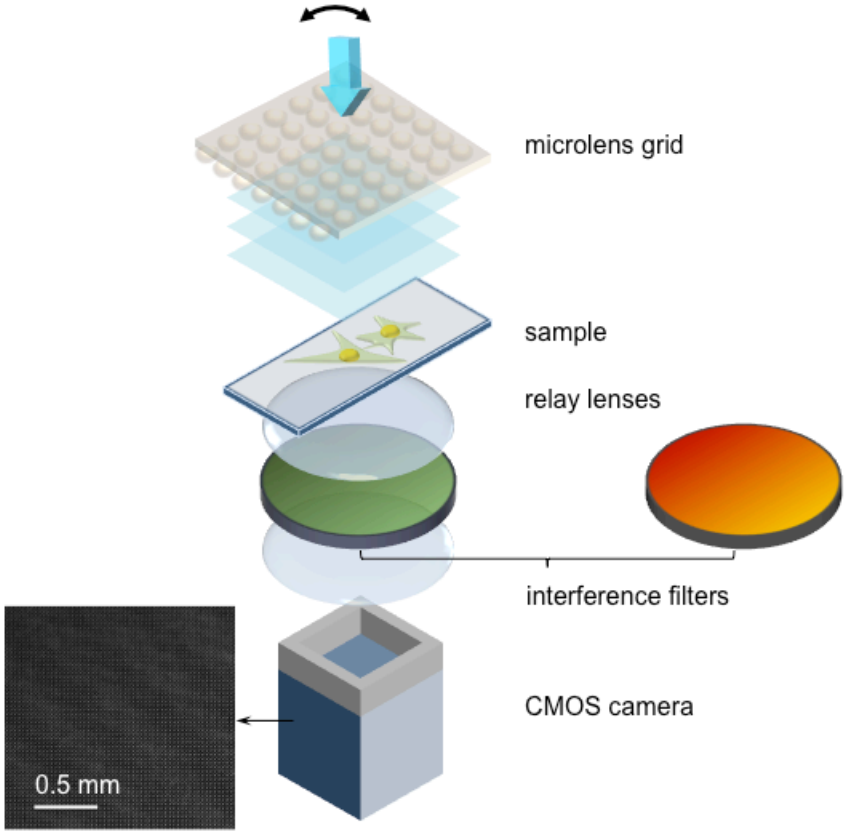

Figure 6.3. System setup for the sample and detection optics. The sample was placed at Talbot distance away from the focal grid generated by the microlens array, and two SLR camera lenses (f=50 mm) form a 1:1 relay system to collect the fluorescence signal; the optical filters was inserted between the relay lenses. (Insert) The Talbot focal spot imaged by the CMOS camera without inserting the optical filter.

6.3 Resolution and depth of focus

The resolution of the system can be quantified by measuring the PSF of the Talbot focal spot. We use the Talbot system to image the 200nm green fluorescent microspheres (Life Technologies, FluoSpheres® 0.2 µm). Figure 6.4 (a) shows the setup of the measurement scan scheme. The step size of the scan was 0.25 µm. Figure 6.4 (c, d) shows the measured lateral profile of the resolution. The lateral intensity profile was fit to Gaussian functions, and the FWHM were 1.20 µm and 1.21 µm along the horizontal direction and vertical direction, respectively.

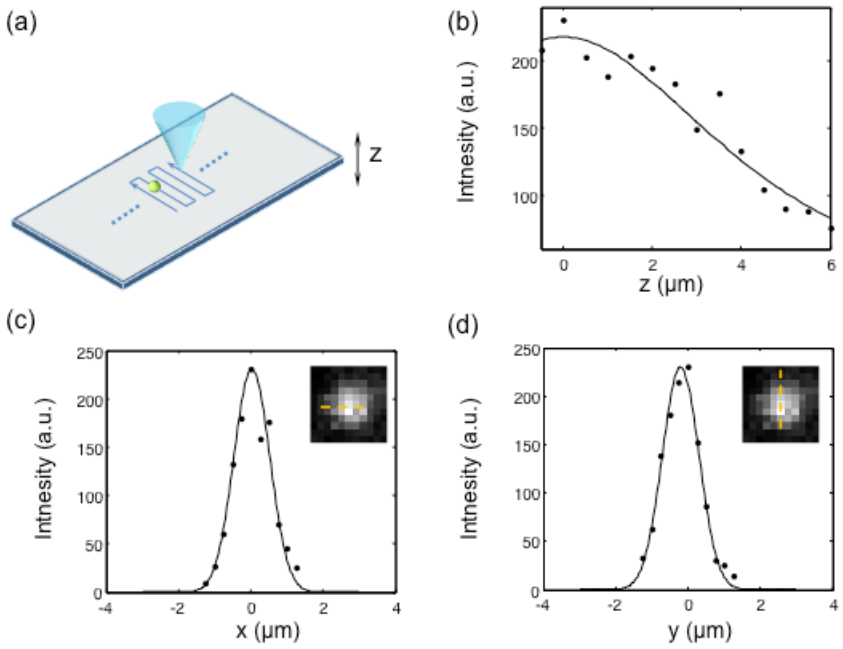

Figure 6.4. System resolution of the multicolor FTM. (a) The point spread function of the Talbot focal spot was measured by scanning a 200 nm fluorescence bead. (b) The z profile of the Talbot focal spot, (c) the x profile of the Talbot focal spot, and (d) the y profile. The insert of (c) and (d) is the image of the 200 nm fluorescence bead.

We also measured the focal depth along the axial direction. The microsphere sample was placed on a translational stage (Newport, ESP0001), and was moved along the z direction with a step size of 1 μm. Figure 6.4 (b) shows the *z* profile measurement.

Assuming the Talbot focal spot as it propagates along the axis has a Gaussian beam profile. We fit the z axis profile with

$$I(z) = I_0 \Big/ \left[1 + (z / z_r)^2\right], \tag{6.1}$$

where I_0 is the central intensity of the Talbot focal spot, and z_r is the half focal depth of the beam. The experimentally measured focal depth was 9.7 μm.

Using the measured lateral profile mentioned above, we can also calculate the depth of the focus by the beam width ω_0 with Equation 6.1.

$$2z_r = \frac{2\pi\omega_0^2}{\lambda} \ . \tag{6.2}$$

The calculated focal depth is 12.8 μm, which is close to the experimental results. The small difference can be attributed to the relay system. Note that the camera lens relay system has an N.A. = 0.4, so the relay system can also provide optical sectioning. However, the relay system did not serve as a direct fluorescence imaging system, so the focal depth limit should not be calculated by $\lambda/(\text{N.A.})^2$. The camera collected the fluorescence spread to an area of four by four pixels (24 μm by 24 μm). The focal depth limit calculated from geometric optics was 24 μm/(N.A.) = 60 μm. This depth was much larger than the focal depth provided by the Talbot focal spot. Therefore the focal depth of the system was greatly determined by the focal depth of the Talbot spot.

6.4 Results

6.4.1 Full FOV fluorescence microspheres imaging

First, we applied the system to image green fluorescence microspheres (Bangs Laboratories, DG06M 8 μm diameter). To satisfy the Nyquist sampling theorem, the step size was chosen to be 0.60 μm. The number of scan steps was 56 along one direction. The extra six steps provide an overlap region between the adjacent tiles. Each tile has 56×56 = 3156 pixels. With approximately 40 nW on each focal spot, the dwell time for each pixel was 7 ms, which was limited by the frame rate of 140 frames per second. The full field imaging time was 23 seconds.

The full field image was reconstructed from 410×330 Talbot focal spots, and the reconstructed image contained 20500×16500 pixels. The image was reconstructed using Matlab code. The reconstruction time was 7 minutes on a 64-bit Windows7 personal computer with Intel Xeon® 2.5 GHz CPU and 36 GB memory.

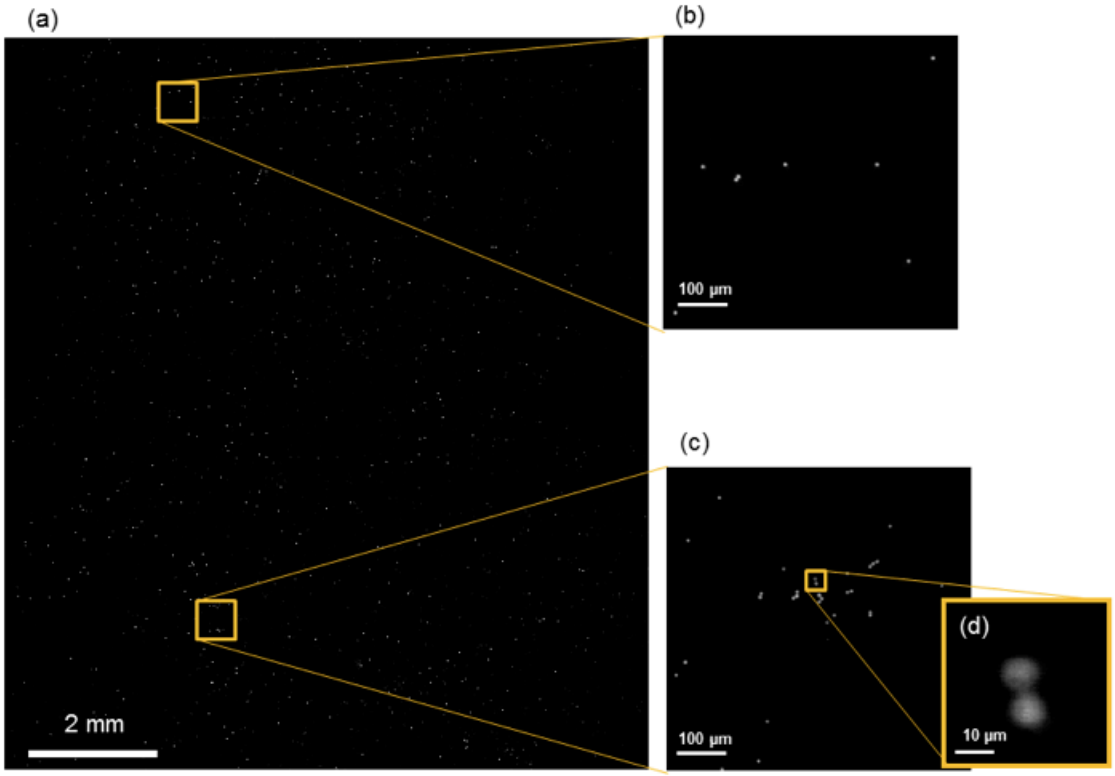

Figure 6.5. Image of fluorescence microspheres. (a) The full field of view (FOV) image of 8 µm microsphere. (b), (c) The enlarged view of two 0.55 mm by 0.55 mm sections. (d) A further enlarged view to show two microspheres next to each other.

Figure 6.5 shows the full FOV image. The full FOV was 12 mm by 10 mm. From the enlarged sections of the image we can easily distinguish the adjacent microspheres.

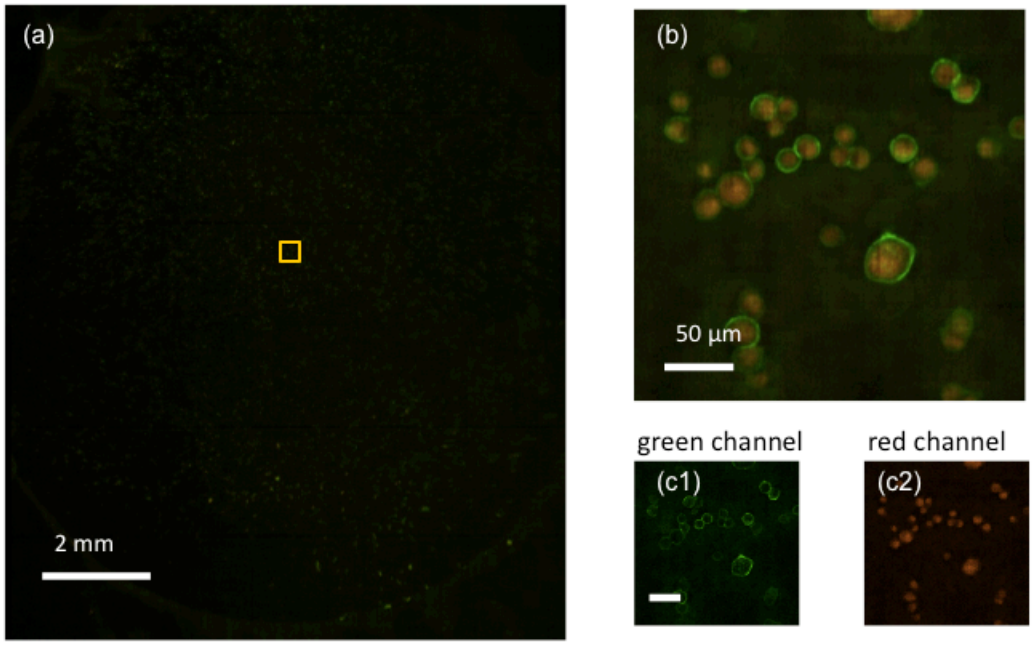

Figure 6.6. Fluorescent image of human breast cancer cell line SK-BR-3. The cell membrane marker Her2 was stained with Alexafluo 488 (green), and cell nucleus was stained with PI (red). (a) The full field of view (FOV) image. (b) The enlarged view of the region indicated in (a). (c1) The green channel. (c2) The red channel.

6.4.2 Multicolor fluorescence imaging of human breast cancer cell line

Compared with the system described in the on-chip system mentioned in Chapter 4 and Chapter 5, the current system provides the flexibility of imaging multiple color fluorescence. Here we demonstrate the multicolor fluorescence imaging capability by imaging the human breast cancer cell line SK-BR-3 (ATCC). The SK-BR-3 cell line has a cancer marker (HER2) on the membrane, which was labeled by AlexaFluo 488 and the cell nuclei were labeled with propidium iodide (PI). Both fluorescent probes can be excited by 488 nm laser line.

The cells were fixed with 4% formaldehyde for 5 min, and incubated sequentially with mouse anti-HER2 (c-erbB-2) antibody (Life Technologies, 187107) for 1 h and 5 nM AlexaFluo 488 goat F(ab')2 anti-mouse IgG conjugate (Life Technologies, A10684) for 1 h, then washed with Dulbecco's phosphate-buffered saline (DPBS, Life Technologies). The sample was then incubated with 500 nM PI (Life Technologies, P3566) in 2X SCC (0.3 M NaCl, 0.03 M sodium citrate, pH 7.0) solution for 10 minutes at 37°C.

A green interference emission filter (Edmund Optics, 86-627) was used for imaging the HER2 marker on the cell membrane. The pixel dwell time was 40 ms. A red interference filter (Edmund Optics, 87-011) was used for imaging the cell nuclei stained by PI. The pixel dwell time was 30 ms. The total scan time for two channels was about 200 seconds.

The two channels were combined to generate the double color image. Figure 6.6 shows the full FOV images of the double stained SK-BR-3 cells. We can clearly distinguish the cell membrane and cell nuclei.

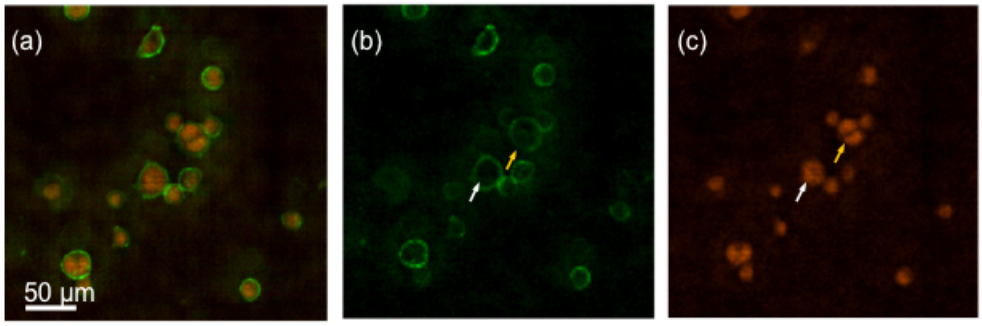

Figure 6.7. Two-color fluorescence image reveals cell cycle. (a)Two channel image. (b) The green channel. (c) The red channel.

Figure 6.7 shows another area within the full FOV image. In Figure 6.7 (b) and (c), we can clearly see the cell indicated by the yellow arrow is in mitosis. The cell nuclear has divided into two and the cell membrane has not yet split. The cell indicated by the white arrow has similar membrane morphology. By examining the PI channel, we can tell that the cell has one nucleus and has not reached cell division cycle.

In this experiment, one excitation wavelength excited two different fluorophores. The system could also be adjusted for multiple laser beams to image fluorophores with different excitation wavelengths, with a stage to move the detection side along the z-axis to accommodate the Talbot distance change for different wavelengths. It is possible to implement both bright field imaging and fluorescence imaging by using another non-excitation laser for bright field imaging.

The FOV of the system is determined by the dimension of the Talbot focal spots, the field of the relay lens and the imaging area of the CMOS sensor. In the current setup the Microlens grid has a

dimension of 40 × 40 mm^2, and the SLR camera lens is designed for 50 mm film format. Therefore, the current FOV is determined by the imaging area of the CMOS camera, which is 14 × 10 mm^2. One simple way to increase the FOV is by using a demagnification relay system on the detection side. This means the N.A. on the sample side is less than the N.A. on the image side. This will restrict the collection efficiency of the system.

For the imaging of the microsphere sample, the imaging speed was limited by the electronic readout speed. In the double-color fluorescence imaging experiment, low fluorescence signal level limits the imaging speed. Due to the large FOV, the excitation intensity of each Talbot spot is very low, only ~10^{-5} mW. A higher power laser could be used to improve the imaging speed. We would like to point out that the key to improved imaging speed is to increase the collection efficiency. The current system has a collection N.A. of 0.4. A collection system with a larger N.A. could be employed to improve the imaging speed.

6.5 Conclusion

In this chapter, we have described a microscopic imaging system based on the Talbot effect that can achieve wide field-of-view (FOV) imaging. Taking advantage of the phase sensitivity of the Talbot effect, we perform the sample scanning by tilting the incident beam to the microlens grid. This scanning scheme avoids the off-axis aberration to the focal spot grid. The prototype system has achieved an FOV of 12 × 10 mm^2 at a resolution of 1.2 μm. The acquisition time can be as fast as 23 s for one fluorescence channel. We have demonstrated the imaging of green fluorescence beads and double stained human breast cancer cell line SK-BR-3. We expect this system can be applied in wide FOV screening and sensing applications. In the last three chapters, we have covered the instrumental development part of the Talbot microscope. In the next chapter we will describe two biological applications using the on-chip FTM prototype.

REFERENCES

1. C.-D. Hu, and T. K. Kerppola, "Simultaneous visualization of multiple protein interactions in living cells using multicolor fluorescence complementation analysis," *Nature Biotechnology* **21**, 539 (2003).
2. H. Tsurui, H. Nishimura, S. Hattori, S. Hirose, K. Okumura, and T. Shirai, "Seven-color fluorescence imaging of tissue samples based on Fourier spectroscopy and singular value decomposition," *Journal of Histochemistry & Cytochemistry* **48**, 653-662 (2000).
3. G. Feng, R. H. Mellor, M. Bernstein, C. Keller-Peck, Q. T. Nguyen, M. Wallace, J. M. Nerbonne, J. W. Lichtman, and J. R. Sanes, "Imaging neuronal subsets in transgenic mice expressing multiple spectral variants of GFP," *Neuron* **28**, 41-51 (2000).
4. B. Neumann, T. Walter, J. K. Heriche, J. Bulkescher, H. Erfle, C. Conrad, P. Rogers, I. Poser, M. Held, U. Liebel, C. Cetin, F. Sieckmann, G. Pau, R. Kabbe, A. Wunsche, V. Satagopam, M. H. A. Schmitz, C. Chapuis, D. W. Gerlich, R. Schneider, R. Eils, W. Huber, J. M. Peters, A. A. Hyman, R. Durbin, R. Pepperkok, and J. Ellenberg, "Phenotypic profiling of the human genome by time-lapse microscopy reveals cell division genes," *Nature* **464**, 721-727 (2010).
5. "Hamamastu NanoZoomer 2.0-HT Catalog," http://jp.hamamatsu.com/resources/products/sys/pdf/eng/e_ndp20.pdf.
6. J. Wu, X. Cui, G. Zheng, Y. M. Wang, L. M. Lee, and C. Yang, "Wide field-of-view microscope based on holographic focus grid illumination," *Optics Letters* **35**, 2188-2190 (2010).
7. J. G. Wu, G. A. Zheng, Z. Li, and C. H. Yang, "Focal plane tuning in wide-field-of-view microscope with Talbot pattern illumination," *Optics Letters* **36**, 2179-2181 (2011).
8. S. Pang, C. Han, M. Kato, P. W. Sternberg, and C. H. Yang, "Wide and scalable field-of-view Talbot-grid-based fluorescence microscopy," *Optics Letters* **37**, 5018-5020 (2012).
9. C. Han, S. Pang, D. V. Bower, P. Yiu, and C. Yang, "Wide field-of-view on-chip Talbot fluorescence microscopy for longitudinal cell culture monitoring from within the incubator," *Analytical Chemistry* **85** (4), 2356–2360 (2013).
10. A. Orth, and K. Crozier, "Microscopy with microlens arrays: high throughput, high resolution and light-field imaging," *Optics Express* **20**, 13522-13531 (2012).
11. A. Orth, and K. Crozier, "Gigapixel fluorescence microscopy with a water immersion microlens array," *Optics Express* **21**, 2361-2368 (2013).
12. B. Hulsken, D. Vossen, and S. Stallinga, "High NA diffractive array illuminators and application in a multi-spot scanning microscope," *Journal of the European Optical Society-Rapid Publications* **7**, 12025, 2026 (2012).
13. A. Olszak, and M. Descour, "Microscopy in multiples," *IEEE OE Magzine*, 16-18 (2005).
14. A. W. Lohmann, and J. A. Thomas, "Making an array illuminator based on the Talbot effect," *Applied Optics* **29**, 4337-4340 (1990).
15. W. J. Smith, and I. Genesee Optics Software, *Modern Lens Design: A Resource Manual* (McGraw-Hill, 1992).
16. F. Pfeiffer, T. Weitkamp, O. Bunk, and C. David, "Phase retrieval and differential phase-contrast imaging with low-brilliance X-ray sources," *Nature Physics* **2**, 258-261 (2006).
17. A. W. Lohmann, and D. E. Silva, "An interferometer based on the Talbot effect," *Optics Communications* **2**, 413-415 (1971).

C h a p t e r 7

BIOLOGICAL APPLICATIONS OF THE FLUORESCENCE TALBOT MICROSCOPE

In Chapter 4 and Chapter 5, we have introduced the FTM imaging principle, prototype implementation, and we have also characterized the resolution and collection efficiency of the system. The chip-scale FTM system is compact, and it has a collection efficiency equivalent to a 0.7 N.A. microscope objective and an FOV of 14 mm^2. With these advantages over the conventional fluorescence microscope, we expect it to be applied to many biological problems.

In this chapter we will demonstrate two biological applications that take advantage of the large FOV and the compactness of the system. We will describe the application of FTM system in phenotyping the distal tip cells (DTC) development of *C. elegans*. We will also demonstrate drug screening by integrating a microfluidic cell culture system with FTM that enables large FOV time-lapse fluorescence imaging of living cells.

7.1 Phenotyping of *C. elegans* based on FTM imaging

The full FOV of FTM is about 100 times larger than that 20X microscope objective. In addition, the FTM is compact, and thus is very suitable for system parallelization. Therefore, FTM is very suitable for screening applications. In this section we will demonstrate the utility of the large FOV in simultaneous imaging of a large number of *C. elegans* (~ 50 adult *C. elegans*.) for the DTC migration phenotyping experiment.

7.1.1 *C. elegans* and distal tip cells

In the hermaphrodite *C. elegans*, the gonad achieves its final shape through the migration of two DTCs located at the opposite ends of the developing gonad. Figure 7.1 shows the cartoon of the *C. elegans* and the development of the gonad. Beginning at approximately 12 hours post-hatching, the DTCs migrate away from each other until 28 hours post-hatching, then turn back, and migrate towards one another until 38 hours post-hatching when they cease migration [1]. We used the distance between the two DTCs as the readout of the progress in migration. We also examined worms having two different types of migration defects. In animals deficient for *daf-12*, which encodes a transcription factor affecting developmental timing [2], the DTCs migrated only slightly

more slowly than wild-type. After 28 hours post hatching, the DTCs continued to migrate away from each other instead of turning back. Worms that were deficient in the gene *gon-1*, encoding a metalloprotease required for remodeling the basement membrane around the DTCs will not migrate during development.

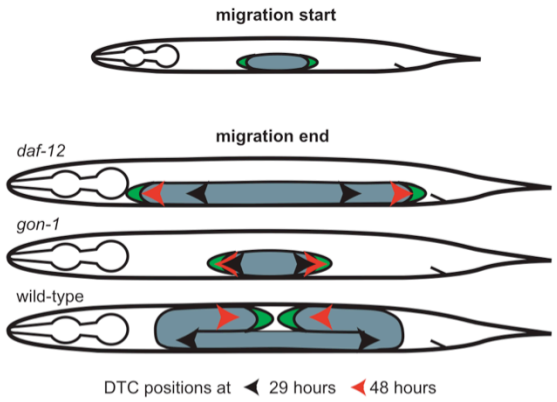

Figure 7.1. The illustration of the migratory path of the DTCs in mutant *daf-12*, *gon-1*, and wild-type hermaphrodite *C. elegans*.

7.1.2 Phenotyping of *C. elegans* DTCs migration by RNA interference

To observe and quantify the DTC migration and the effect of silencing *gon-1* and *daf-12* to the migration of DTCs, we applied FTM to image the synchronized population of worms with GFP-labeled DTCs. We imaged the *C. elegans* population at two typical time points of the migration: 29 h and 48 h. The large FOV of the FTM allowed us to image up to 50 adult worms on one chip.

In the experiments we used the *C. elegans* strain JK2868 qIs56 [lag-2::GFP; unc-119(+)]. The *C. elegans* were cultured at 22°C. The eggs were harvested from JK2868 gravid adults by bleaching and placed on plates containing either *gon-1* RNAi bacteria, *daf-12* RNAi bacteria, or bacteria without an RNAi construct, and the worms were allowed to develop at 22°C.

The RNAi bacteria were obtained from the Ahringer Library (Geneservice), and their RNAi feeding protocol was used with modifications [3]. RNAi feeding plates were made by spreading carbenicillin at 25 μg/mL and IPTG at 1 mM final concentration on agar plates, and adding RNAi liquid bacterial culture. The plates were either used the following day or stored at 4°C.

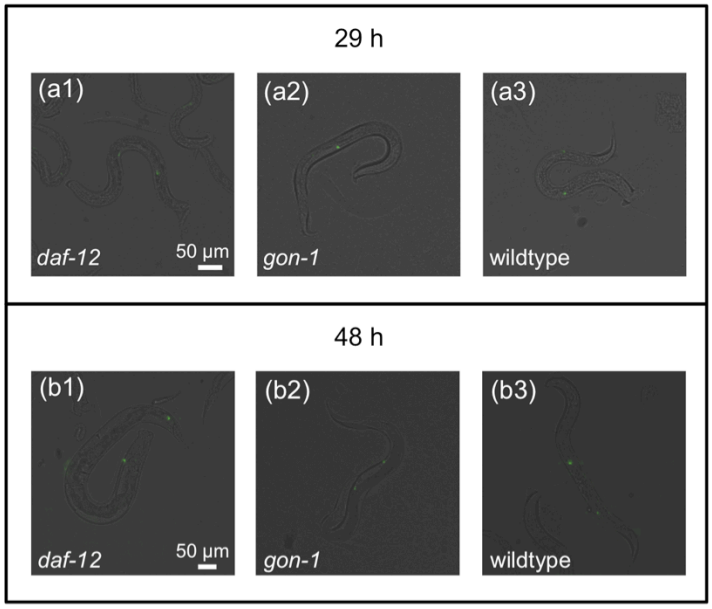

Figure 7.2. FTM images of *C. elegans* DTCs labeled with GFP superimposed with bright field images. (a1-a3) *daf-12* mutant, *gon-1* mutant and wild-type worms at 29 h. (b1-b3) *daf-12* mutant, *gon-1* mutant and wild-type worms at 48 h.

The *C. elegans* worms were immobilized on the CMOS sensor using hydrogel by modifying established protocols [4]. Briefly, hydrogel prepolymer solution was prepared by adding 20% (wt/wt) poly(ethylene glycol) 1000 dimethacrylate (PEG-DMA, Polysciences) in DPBS, then 1% (wt/wt) Irgacure 2959 (2-hydroxy-1-(4-(hydroxyl-ethoxy) phenyl)-2-methyl-1-propanone, BASF) as the photoinitiator. Worms were washed into the hydrogel prepolymer solution, and a 2 µL worm suspension was mounted onto the green filter-coated sensor with a 5 mm-diameter coverslip on top. A UV exposure of ~10 mW cm^{-2} at 365 nm for 1 min was applied to induce gelation.

Our current FTM prototype has the ability to perform low-resolution bright field imaging by illuminating the sensor chip with light at the pass band wavelength of the absorption filter. Such a direct shadow imaging approach can provide a coarse bright field image to be used in conjunction with the high-resolution fluorescence image.

Figure 7.2 shows the typical image acquired by FTM superimposed with the bright field image directly acquired by the sensor chip. The current bright field resolution is equal to the size of 2 sensor pixels (4.4 µm for our prototype).

With the bright field and the fluorescence images, we can measure the body length and DTC distance of the *C. elegans* population. We first detected the boundary of each worm in bright field images. We then segmented an individual *C. elegans* image along its length and manually marked the central point for each segment. Next, we connected the central points by line segments. The length of the *C. elegans* was given by the total length of the line segments. The fluorescence image from FTM was superimposed with the bright field image and the center points of DTCs were marked. The distance between the two DTCs was measured with the same method as the length of the *C. elegans*. Figure 7.3 shows the histogram of the *C. elegans* body length and DTC distance at the 29 h time point.

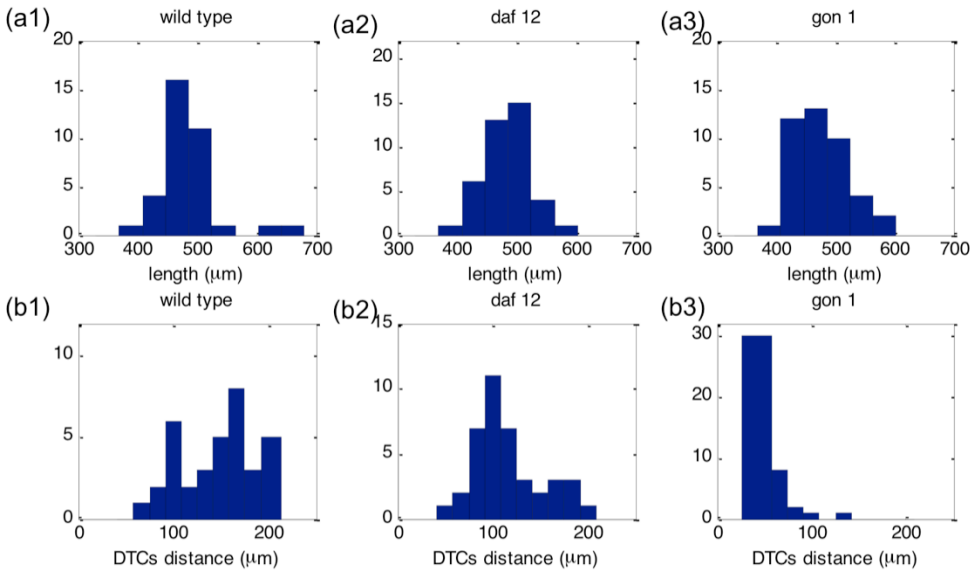

Figure 7.3. Histogram of the *C. elegans* body length and DTC distance at 29 h. The Y-axis stands for the number of worms. (a) Body length histogram for wild-type (a1), *daf-12* (a2), and *gon-1*(a3). (b) DTC distance histogram for wild-type (b1), *daf-12* (b2), and *gon-1*(b3).

The mean distance between the DTCs was 147±40 μm at 29 h for the wild-type worm population. For the worms that were deficient in the gene *daf-12* the mean DTC distance was 116±36 μm and the worms that were deficient in the gene *gon-1* showed little migration after 29 h: the DTC distance was only 54±19 μm. The mean body length of the worms were 490±50 μm, 480±40 μm, and 480±50 μm, for the wild-type, gene *daf-12* deficient and gene *gon-1* deficient animals,

respectively. The body lengths of the wild-type and migration-defective animals were not significantly different.

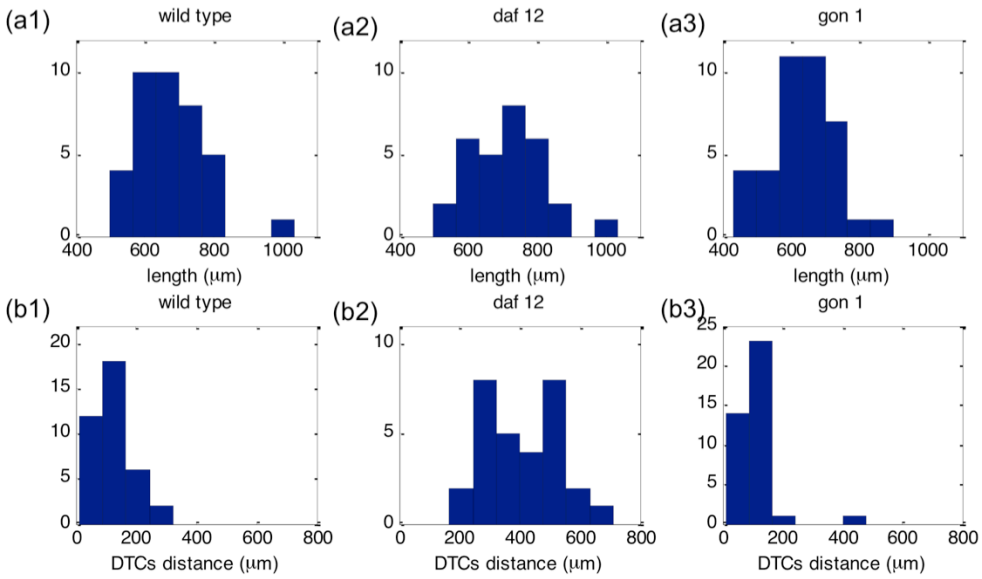

Figure 7.4. Histogram of the *C. elegans* body length and DTC distance at 48h. The Y-axis stands for the number of worms. (a) Body length histogram for wild-type (a1), *daf-12* (a2), and *gon-1*(a3). (b) DTC distance histogram for wild-type (b1), *daf-12* (b2), and *gon-1*(b3)

Figure 7.4 shows the histogram of the *C. elegans* body length and DTC distance at the 48 h time point. As the DTCs migrated outwards and then turned back, the mean distance was slightly shorter than at the 29 h time point, but the orientation of the two DTCs was opposite. This is also illustrated by Figure 7.1. The mean distance between the DTCs was 124±65 μm at 48 h for the wild-type worm population. For the worms that were deficient in the gene *daf-12* the DTCs continually migrate outwards consistently, and the mean DTC distance was 403±138 μm. For the worms that were deficient in the gene *gon-1*, the DTC distance was only 107±58 μm. The mean body length of the worms were 680±90 μm, 720±100 μm, and 640±90 μm, for the wild-type, gene *daf-12* deficient and gene *gon-1* deficient animals, respectively. The body lengths of the wild-type and migration-defective animals were not significantly different at 48 h time point.

Figure 7.5 summarized the comparison between the wild-type and migration-defective animals for 29 h and 48 h. In animals deficient for *daf-12*, which encodes a transcription factor affecting

developmental timing [2], the DTCs migrated only slightly more slowly than wild-type at 29 h ($P<0.001$, Student's t test), but at 48 h, the mean distance was 415±124 μm ($P<0.0001$, Student's t test) strongly indicating that the DTCs continued to migrate away from each other instead of turning back. Worms that were deficient in the gene *gon-1*, encoding a metalloprotease required for remodeling the basement membrane around the DTCs [5], showed little migration compared to the wild-type after 29 h ($P<0.0001$, Student's t test).

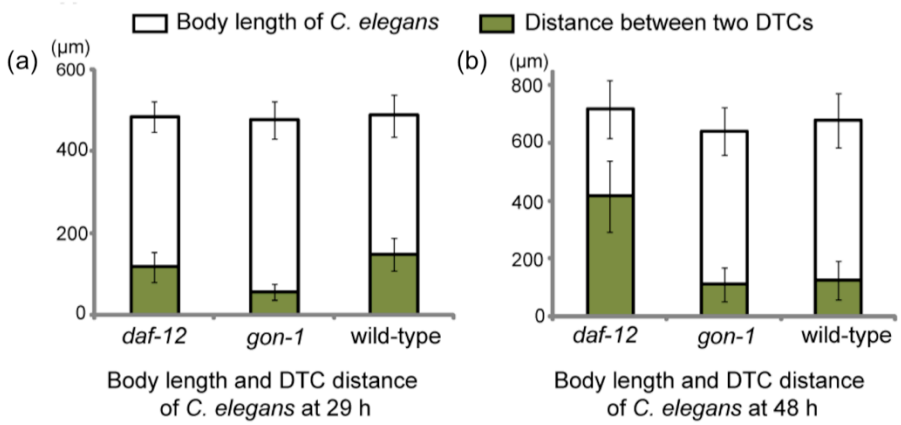

Figure 7.5. Phenotyping results of the DTC migration. (a) The statistics of DTC distance 29 h: the number of the worms of the wild-type, *daf-12*, and *gon-1* were 35, 40, and 42, respectively. (b) The statistics of DTC distance at 48 h: the number of worms of the wild-type, *daf-12*, and *gon-1* were 38, 30, and 38, respectively.

7.2 Longitudinal fluorescence imaging platform for live cells

Instead of observing only the endpoint, time-lapse imaging of live cell provides useful temporal information for understanding physiological processes and cell behavior [6]. In the case of fluorescence imaging, longitudinal studies require special care to minimize photo-bleaching and photo-toxicity caused by extensive exposure. With its high collection efficiency and compactness, FTM can reduce the excitation dosage and can be easily integrated into a cell culture imaging system.

The intrinsic large FOV of the FTM allows simultaneous fluorescence imaging of a large number of samples (~2000 cells in this case) that is otherwise unachievable with conventional microscopy without laborious pan-and-scan. This advantage coupled with the compact nature of the FTM

design indicates that the FTM is a good basis technology for implementing self-imaging fluorescence time-lapse imaging systems.

7.2.1 Microfluidic cell chamber for cell culture

In the adaption of the FTM to a time-lapse imaging system, the Talbot illuminator remains the same as described Chapter 4. The major modification is on the absorption filter-coated CMOS sensor chip. The coated absorption fluorescence filter (Aptina green1, Aptina) has a thickness of ~10 μm, and an optical density of 6 [7].

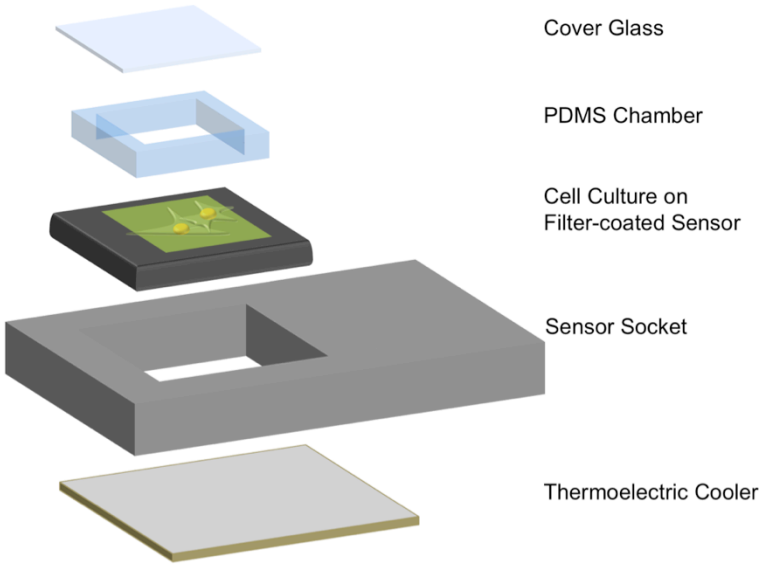

Figure 7.6. Microfluidic cell culture chamber setup for time-lapse imaging using FTM. A micro chamber made of PDMS was built on top of an image sensor, and a thermoelectric cooler (TEC) attached to the bottom of the sensor socket for temperature control.

An additional PDMS layer was spin-coated on top of the filter layer for protection. The microfluidic component was made from PDMS by following standard micro-molding processes [8]. The completed microfluidic component was attached to the coated CMOS sensor with the edges sealed by PDMS. The cell culture chamber in the microfluidic component had a dimension of 4 mm × 3.5 mm and a height of 400 μm. The ceiling of the chamber was a glass coverslip.

Figure 7.6 shows the microfluidic cell culture chamber setup for the longitudinal imaging application. This microfluidic-integrated sensor chip was mounted onto a camera board (SV9M001, EPIX) via a customized sensor socket. A thermoelectric cooler (TEC, 89413, American Science & Surplus) was attached to the socket and turned on during live cell imaging to protect cells from the heat generated by the sensor circuit. A CPU fan cooled the backside of the TEC.

To provide an adequate cell culture environment, the imaging platform was placed inside a humidified 5% CO_2 incubator at 37 °C. We turned on the TEC (power input = 13W) during imaging to prevent the sensor surface temperature from exceeding 37 °C.

We used HeLa cells expressing nuclear GFP in the experiment and cultured the cells directly on the FTM sensor that was housed in an incubator. HeLa cells (ATCC) were infected at approximately 35% confluence with VSVG-pseudotyped lentivirus to obtain cells ubiquitously expressing eGFP fused to histone-2B (H2B), driven by the chicken beta-actin-CMV (CAG) promoter. Stably infected cells were propagated in DMEM (Cellgro) supplemented with 10% FBS (Cellgro).

The microfluidic-integrated image sensor was treated with Poly-L-lysine solution (Sigma-Aldrich) overnight for better cell attachment. Upon experiment, the cell solution was adjusted to a concentration of 1×10^6 cells/ml, and loaded into the microfluidic device. After 4 h of incubation to permit the cells to attach to the image sensor surface, the image sensor was mounted onto the socket for imaging.

Figure 7.7 (a) shows a representative full FOV image of the cell culture collected by the FTM. Figure 5 (b1) - (b3) are vignettes of the same image and they show the morphological differences of the cell nuclei in G1 phase (b1), G2 phase (b2), and mitosis phase (b3). The different cell cycle phases are clearly discernible.

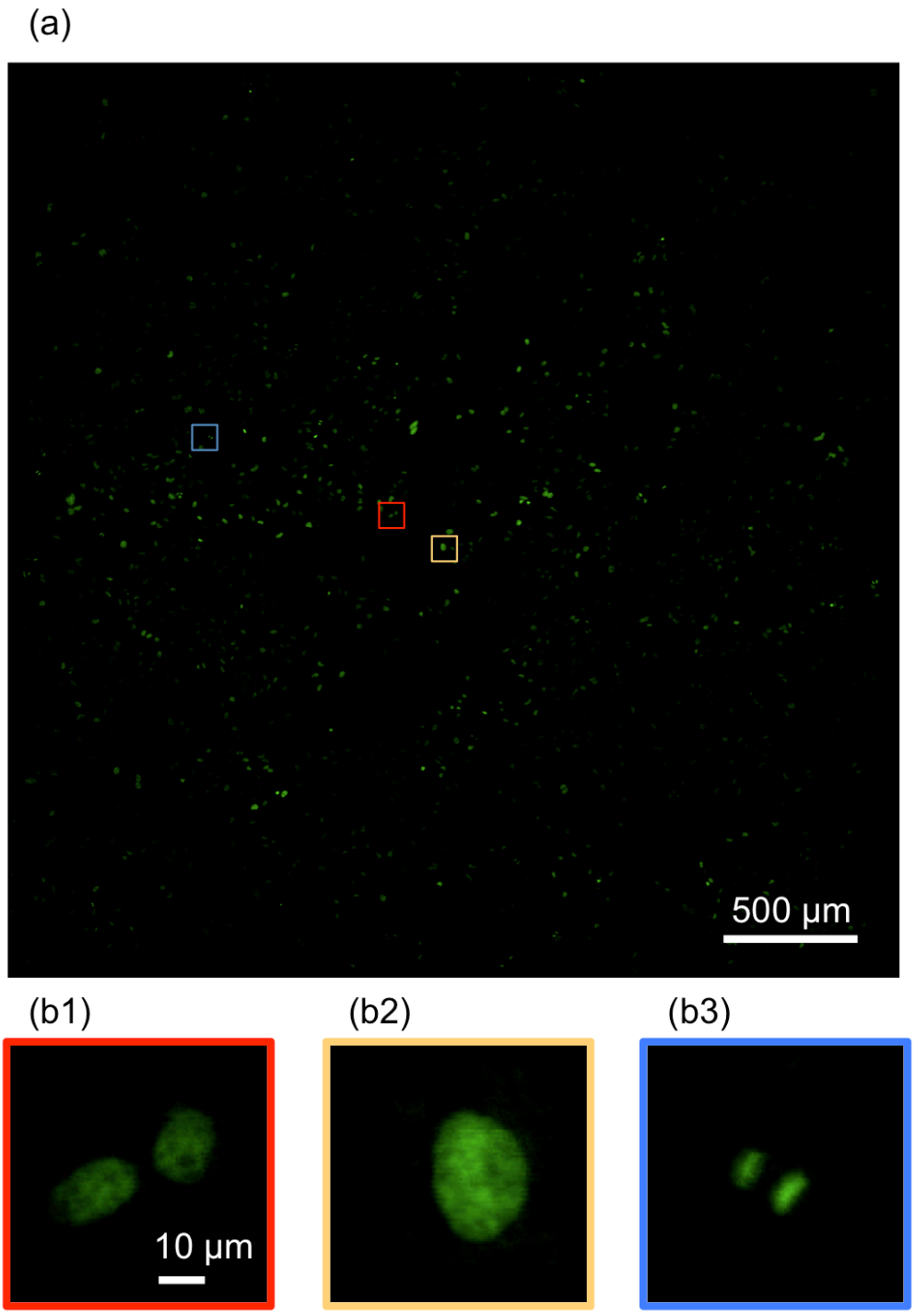

Figure 7.7. FTM time-lapse image of the HeLa cell culture. (a) The full FOV of the HeLa cell culture. (b) the magnified images of cells in G1 phase (b1), G2 phase (b2), and mitosis phase (b3).

7.2.2 Cell segmentation algorithm

To be able to quantitatively extract the features of the image sequences of the cell culture, we develop a method to segment individual cells from the whole FOV images based on the watershed segmentation algorithm. The segmentation algorithm can provide the cell count and the morphological information of the cell nucleus.

Cell nuclei in FTM images were segmented and counted using Matlab, by following the well-established watershed algorithm with minor modifications [9, 10]. Briefly, FTM images were smoothed using a Gaussian filter, followed by a background subtraction. The edges and local maxima of cell nuclei were detected, and used by the Matlab build-in watershed algorithm for segmentation. Segmented objects were analyzed to get the number of cells. Figure 7.8 shows the key steps of the segmentation process. By inspecting four random selected 1.2 mm × 1.2 mm regions, the segmentation has an accuracy of 95.7 ± 1.4 % (877 objects, 3.3 ± 1.8 % over segmented and 1.0 ± 0.5 % under segmented).

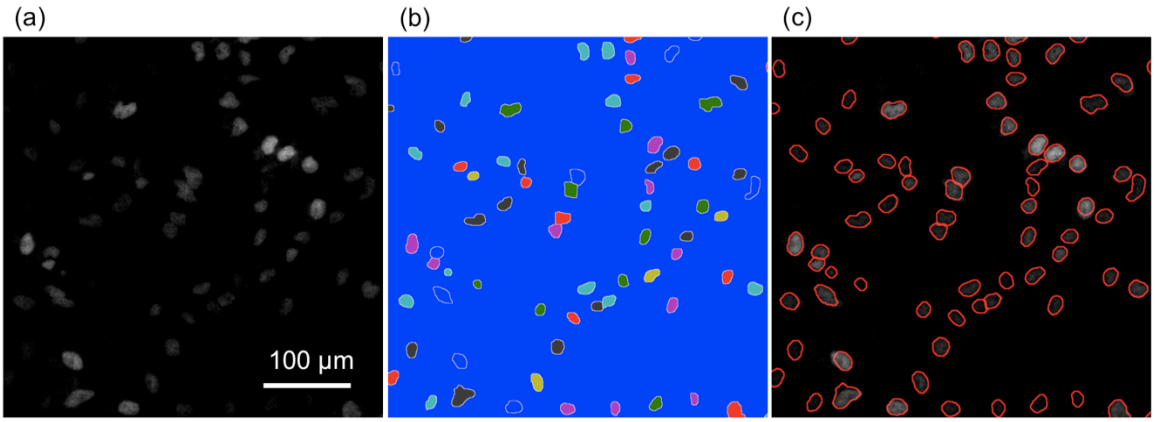

Figure 7.8. Cell segmentation and counting using the watershed algorithm. (a) A selected region from the FTM image of HeLa cells labeled by H2B-GFP. (b) Result of segmentation by watershed algorithm. (c) The segmentation result superimposed with the original image.

7.2.3 Quantification of the effect of the anticancer drug camptothecin

Drug screening is an excellent longitudinal study format for which an inexpensive, high-resolution and wide FOV fluorescence imaging system can significantly improve the efficiency. As a demonstration of such an application, we performed the following experiment with camptothecin (CPT) - a well-characterized anti-cancer drug. CPT inhibits DNA and RNA replication and synthesis by targeting the nuclear enzyme topoisomerase I [11]. Analogues of CPT have been successfully used in cancer chemotherapy [12].

We performed the longitudinal study on two groups of Hela cells that were cultured on separate filter-coated CMOS sensor chips. 12 hours after the cell plating, the experiment group was exposed to 5 μM camptothecin (Sigma Aldrich), and the control group had no CPT. Both groups were cultured on chip for 24 hours. FTM captured images every 12 hours to produce a 3-frame time-lapse sequence. We applied the watershed algorithm to all FTM images for cell segmentation and counting as mentioned in the previous section. Figure 7.9 (a) shows a small area of the CPT treated group at the three time points. Within this region, cell growth or cell division was not observed. Figure 7.9 (b) showed an area of control group at the three time points.

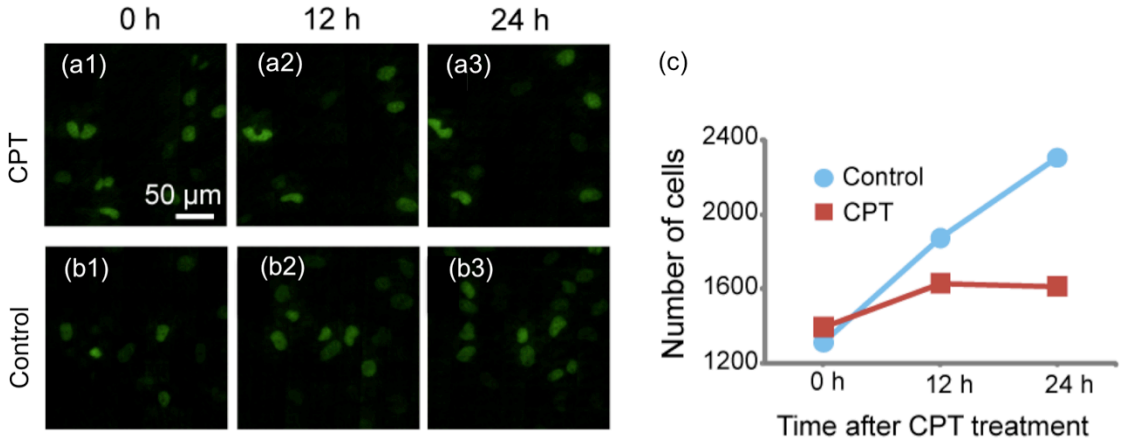

Figure 7.9. Time-lapse imaging to quantify the effect of camptothecin (CPT) on HeLa cell culture by FTM. (a) The magnified time lapse sequence of the experiment group exposed to CPT at 0, 12 and 24 h time points. (b) The time lapse sequence of the control group at same time points. (c) The total cell counts of the control and experiment group at each time point.

By using the segmentation algorithm we described in the previous section, we could count the cell number for the control and CPT treated group. Figure 7.9 (c) shows the results. For the CPT treated group, we observed that the total cell count increased 16.8% during the first 12-hour period. We did not observe a statistically significant increase from 12 h to 24 h. The control group (without CPT) showed an increase of 38.2% and 27.1% during the first and second 12-hour period, respectively. The observation from the CPT treated group was consistent with the fact that CPT is an S phase specific drug [13]. After exposure to CPT, the cells that had passed S phase could continue moving through mitosis phase, which accounted for the increase of the cell number in the first 12 hours. No increase was observed during the second 12-hour period because almost all the cells would have been arrested in S phase.

Our algorithm also provided information on the morphology of the cell nucleus, thus allowing us to further verify the hypothesis by identifying and counting the number of cells in anaphase. We found that the percentage of cells in anaphase in the control group was 0.76%, 0.80%, and 0.78% at 0 h, 12 h, and 24 h, respectively, and that of the experiment group was 0.79%, 0.12%, and 0.06%, respectively. The steep drop of the ratio of cells in mitosis phase for the experiment group in contrast with the near constant ratio for the control group provides strong evidence of the effect of CPT in the experiment group.

7.2.4 Improvements of the time-lapse imaging system

The system demonstrated in this section is semi-automated: the temperature control system was switched on and off manually; the culture media needs to be replaced manually. Due to these limitations, the cell-culture environment was difficult to maintain, and the frame rate of the system was very low. To solve these issues, we further improved the system, which we named the fluorescence ePetri system. The detailed description can be found in Ref [14].

In this system the microfluidic perfusion cell chamber was used. The cell culture chamber had a diameter of 5 mm, with two channels as the inlet and outlet. The microfluidic component was connected with a self-priming micro-pump (EW-73120-64, Cole-Parmer), and fresh medium was loaded into the microfluidic culture chamber every 10 min. The maximum flow speed was set below 50 μm/s, which is within the suggested range for perfusion culture [15]. The illumination, image data acquisition, and micro-pump were all automatically controlled by a customized LabVIEW program.

For measuring the local temperature inside the microfluidic device during the imaging process, the microfluidic device was placed inside the humidified 5% CO_2 incubator at 37 °C. A 76 μm-diameter T-type thermocouple (Omega Engineering) was inserted into the cell culture chamber from the inlet, and the temperature was read out by a digital thermometer. The TEC was switched on 1 min before imaging for pre-cooling.

This improvement on the cell culture environment leads to an increase of the achievable frame rate. We were able to achieve a frame rate of 33 minutes per frame. We further implemented the tracking algorithm to investigate the cell migration division and migration behaviors in response to CPT based on the nearest-neighbor tracking method on the segmented images [16], which finds the next position of each cell by searching its neighborhood in the next frame. A threshold for the neighbor range was defined according to the image sequence to optimize the tracking results. Newly divided cells were given a new tag.

In a proof-of-concept experiment, wide FOV images were taken over a total duration of 21.5 hours. We performed watershed segmentation to count the number of cells in each image. The cells in the control and CPT groups had average total migration distances of 246.0±59.2 μm and 210.3±68.5 μm, respectively, showing a significant difference by the Student's t-test ($P<0.001$). From these data, we can conclude that CPT inhibits cell proliferation and migration.

7.3 Conclusion

In this chapter we have discussed two biological applications that take advantage of the wide FOV and the compactness of the system. In the first section, we have demonstrated the application of the FTM system in phenotyping of distal tip cells (DTC) of *C. elegans*. We further reported a microfluidic environment for large FOV time-lapse fluorescence imaging platform for live cell imaging and drug screening applications. This is the first implementation of automated wide FOV and high-resolution fluorescence imaging for longitudinal cell cultures, in which the conventional microscope objective and its associated shortcomings are eliminated. We further explored the application of our system by observing cellular response to CPT, demonstrating the system's potential for the study of drug dynamics and anticancer drug discovery. Our system is low cost, integratable with microfluidic devices, and compact enough to be placed inside a standard incubator. We believe FTM systems could be further applied on many emerging fields such as

tissue engineering and stem cell differentiation where the longitudinal study of a large number of living samples is needed.

REFERENCES

1. J. Kimble, and D. Hirsh, "The postembryonic cell lineages of the hermaphrodite and male gonads in *Caenorhabditis elegans*," *Developmental Biology* **70**, 396-417 (1979).
2. A. Antebi, J. G. Culotti, and E. M. Hedgecock, "daf-12 regulates developmental age and the dauer alternative in *Caenorhabditis elegans*," *Development* **125**, 1191-1205 (1998).
3. R. S. Kamath, M. Martinez-Campos, P. Zipperlen, A. G. Fraser, and J. Ahringer, "Effectiveness of specific RNA-mediated interference through ingested double-stranded RNA in *Caenorhabditis elegans*," *Genome Biology* **2** (2001).
4. Y. A. Du, E. Lo, S. Ali, and A. Khademhosseini, "Directed assembly of cell-laden microgels for fabrication of 3D tissue constructs," *Proceedings of the National Academy of Sciences of the United States of America* **105**, 9522-9527 (2008).
5. R. Blelloch, and J. Kimble, "Control of organ shape by a secreted metalloprotease in the nematode *Caenorhabditis elegans*," *Nature* **399**, 586-590 (1999).
6. T. Schroeder, "Long-term single-cell imaging of mammalian stem cells," *Nature Methods* **8**, S30-S35 (2011).
7. S. Pang, C. Han, L. M. Lee, and C. H. Yang, "Fluorescence microscopy imaging with a Fresnel zone plate array based optofluidic microscope," *Lab on a Chip* **11**, 3698-3702 (2011).
8. D. C. Duffy, J. C. McDonald, O. J. Schueller, and G. M. Whitesides, "Rapid prototyping of microfluidic systems in poly (dimethylsiloxane)," *Analytical Chemistry* **70**, 4974-4984 (1998).
9. F. H. Long, H. C. Peng, and E. Myers, "Automatic segmentation of nuclei in 3D microscopy images of *C.elegans*," *2007 4th IEEE International Symposium on Biomedical Imaging : Macro to Nano*, **1-3**, 536-539 (2007).
10. L. Vincent, and P. Soille, "Watersheds in digital spaces - an efficient algorithm based on immersion simulations," *IEEE Transactions on Pattern Analysis and Machine Intelligence* **13**, 583-598 (1991).
11. Y. H. Hsiang, R. Hertzberg, S. Hecht, and L. F. Liu, "Camptothecin induces protein-linked DNA breaks via mammalian DNA topoisomerase-I," *Journal of Biological Chemistry* **260**, 4873-4878 (1985).
12. R. Garcia-Carbonero, and J. G. Supko, "Current perspectives on the clinical experience, pharmacology, and continued development of the camptothecins," *Clinical Cancer Research* **8**, 641-661 (2002).
13. Y. H. Hsiang, M. G. Lihou, and L. F. Liu, "Arrest of replication forks by drug-stabilized topoisomerase I-DNA cleavable complexes as a mechanism of cell killing by camptothecin," *Cancer Research* **49**, 5077-5082 (1989).
14. C. Han, S. Pang, D. V. Bower, P. Yiu, and C. Yang, "Wide field-of-view on-chip Talbot fluorescence microscopy for longitudinal cell culture monitoring from within the incubator," *Analytical Chemistry* **85** (4), 2356–2360 (2013).
15. L. Kim, Y.-C. Toh, J. Voldman, and H. Yu, "A practical guide to microfluidic perfusion culture of adherent mammalian cells," *Lab on a Chip* **7**, 681-694 (2007).
16. A. Hand, T. Sun, D. Barber, D. Hose, and S. MacNeil, "Automated tracking of migrating cells in phase-contrast video microscopy sequences using image registration," *Journal of Microscopy* **234**, 62-79 (2009).

C h a p t e r 8

OUTLOOK OF THE FLUORESENCE TALBOT MICROSCOPE

This chapter is the final chapter concerning the fluorescence Talbot microscope (FTM). In this chapter we will discuss the outlook for the FTM. FTM method enables the miniaturization of high-resolution on-chip fluorescence microscopes. We would like to further explore the possibilities of further improvement of FTM in resolution, imaging speed, multi-imaging modalities and other implementation geometries. Because of compactness and cost-effectiveness, the FTM could open up new applications. In this chapter we would also like to envision some of the potential applications for FTM.

8.1 Further system improvement

Image resolution: In Chapter 5, we quantified the resolution of our prototype to be ~1 μm. The current FTM resolution is adequate for a wide range of biological applications. Yet, for end users and instrumental developers alike, there is one logical question to ask: can this resolution be improved? Since the resolution of the FTM is based on the quality of the Talbot focal spot, the key to improving the resolution of FTM is to generate a Talbot focal spot grid with tighter focusing.

While employing a microlens grid that has higher N.A. may appear to be a reasonable solution, it is actually an approach with diminishing returns. In the Appendix, we deduct the Talbot length based on the scalar wave propagation. The Talbot self-imaging effect is a paraxial optical approximation [1], which implies that the Talbot image is unable to faithfully regenerate the focal grid when the focal spot size is comparable to the optical wavelength [2].

As mentioned in the Appendix, for one-dimensional case, the phase factor without any approximation, $\varphi(\alpha,z_T)$, is

$$\varphi(\alpha, z_T) = kz_T\sqrt{1-(\lambda\alpha)^2}\,, \tag{8.1}$$

where z_T is Talbot length; k is wave number, λ is the wavelength, and α is the spatial frequency of the lateral structure. The phase factor with Fresnel approximation, $\varphi_{paraxial}(\alpha,z_T)$, is

$$\varphi_{paraxial}(\alpha, z_T) = kz_T[1 - \frac{1}{2}(\lambda\alpha)^2] \quad (8.2)$$

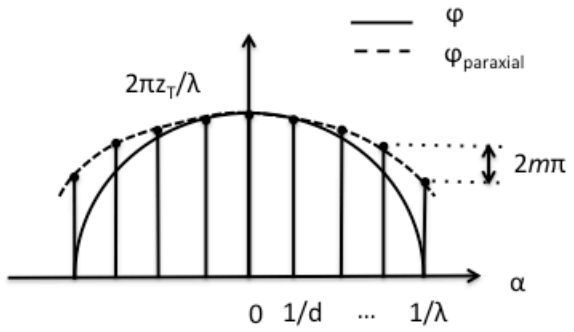

Figure 8.1. The propagation phase with paraxial approximation, $\varphi_{paraxial}$, and the phase with no approximation, φ.

Figure 8.1 illustrates this difference in phase. We only consider this difference, $\delta\varphi(\alpha,z_T)$, to the fourth order term,

$$\delta\varphi(\alpha, z_T) = \varphi_{paraxial} - \varphi \approx kz_T \frac{1}{8}(\lambda\alpha)^4 \quad (8.3)$$

According to Rayleigh criterion, to achieve the diffraction limited focal spot, the maximum phase difference should be less than π/2 [3]. We substitute $z_T = 2d^2/\lambda$, and let $\delta\varphi(\alpha,z_T) < \pi/2$, to get

$$\alpha < \frac{1}{d}\sqrt{\frac{d}{\lambda}} \quad (8.4)$$

For infinite periodic object, α is the integer multiple of 1/d. Equation 8.4 determines the maximum spatial frequency of the structure. As long as the maximum spatial frequency of the structure is less than this limit, the Fresnel approximation is valid, and the Talbot image will not be aberrant. In our prototype, the pitch of a microlens grid, d, is 30 μm, and the wavelength, λ, is 0.488 μm. α should be less than 0.26 μm^{-1}. This spatial frequency is achievable by an aberration-free lens with an N.A. of 0.13. In the FTM prototype, the N.A. of the microlens grid is ~0.15, which is close to this limit. However, if we want to generate a focal spot that equivalent to a microscope objective with an N.A.

of 0.7, the maximum phase difference, $\delta\varphi(\alpha,z_T)$, is about 227π, which is much larger than the limit set by the Rayleigh criterion.

The calculation suggests that the large angle (high spatial frequency) field projections cannot correctly "phase in" with the small angle (low spatial frequency) field at the Talbot length to generate more tightly focused spots. Yet as mentioned in Ref [2], if the scan plane is a little off from the original Talbot distance, the high frequency component can "phase in" and produce a pattern with sharp central peak. On these planes, the PSF of the Talbot spot has larger side band, which is the result of the optical path mismatch from the low frequency components.

Other than shifting the focal plane, one promising way to achieve further resolution improvement would be to redesign the refractive microlens surface. Specially designed diffractive optical elements can be employed to achieve higher resolution [4]. Recorded holograph plates can also achieve high-resolution focus [5]. The calculation showed that to achieve an N.A. of 0.7 ~ 227π of phase difference needs to be compensated for. If we use fused silica as the refractive medium, this phase difference requires a compensation with a thickness of 120 μm. Considering the pitch of a microlens array is only 30 μm, this thickness suggests that it is not realistic to use a continuous optical plate to compensate this difference. In Ref. [4], the diffraction pattern also shows phase discontinuity.

Imaging speed: Unlike the case of bright field imaging, low fluorescence signal level usually limits the imaging speed in fluorescence microscopy. The key to improved imaging speed is high collection efficiency. As shown above, the FTM geometry is capable of collecting a significant fraction of the fluorescence emission.

Using the FTM method to perform large FOV imaging eliminates the sample transportation time for large field-of-view applications. The current imaging speed bottleneck of our prototype is the electronic readout speed. This can be greatly improved by using a sensor with binning capability. With n by n binning of the pixels, the data transfer/storage time can be expected to reduce about n^2 times. In the current prototype, we sum up over all read-in pixels, which contain both non-signal pixels and the pixels with the fluorescence signals. With the binning, we essentially only read in the pixels with the fluorescence signal. The readout speed will be the same as other focal spot grid scanning microscopes [5, 6], in which the readout does not contain non-signal pixels. In the case where the speed is limited by scanning, we expect the FTM to achieve faster imaging speed than the

translational stage based scanning methods, as the scanning speed of the MEMS mirror is faster than the piezo stage.

Finally, The FTM dissociates the collection efficiency from the resolution. For certain high-throughput screen applications, where low-resolution images are sufficient, FTM can increase the imaging speed by using a Talbot focal grid with reduced sharpness and coarser scan steps.

Combination of bright field and fluorescence imaging: Our current FTM prototype has the ability to perform low-resolution bright field imaging by illuminating the sensor chip with light at the emission wavelength. Such a direct shadow imaging approach can provide a coarse bright field image to be used in conjunction with the high-resolution fluorescence image.

As a future development, it is possible to implement high-resolution bright field imaging by using two lasers where the wavelength of one is double that of the other. The shorter wavelength laser can serve as the fluorescence excitation light source and the other can serve as the brightfield illumination source. The first Talbot distance for the excitation wavelength would coincide with the second Talbot distance for the bright-field imaging wavelength. By performing alternate scans with these two light sources, we should be able to collect high-resolution fluorescence and brightfield images.

Depth-selection: The use of the Talbot effect in the FTM scheme carries an additional advantage that has previously been demonstrated for bright field Talbot imaging [7]. Specifically, the Talbot distance can be adjusted by fine-tuning the wavelength of the excitation light, which enables depth-selective imaging of the sample without the need for additional mechanical actuation. In the context of our prototype, a wavelength tuning of 5 nm will allow an axial focal shift of 38 μm.

Non-transmission geometry: The current FTM system is operated in transmission geometry. This system implementation has a couple of drawbacks. First, the system needs two optical surfaces for imaging. This is less convenient for long-term imaging, where cell culture media evaporation causes surface disturbance. Second, the excitation beam takes the same path as the fluorescence emission. The optical filter needs to have higher OD to reject the transmitted excitation beam, and the autofluorescence level from the filter needs to be low.

One way to solve this problem is by implementing an epi-illumination setup for the Talbot microscope, shown in Figure 8.2.

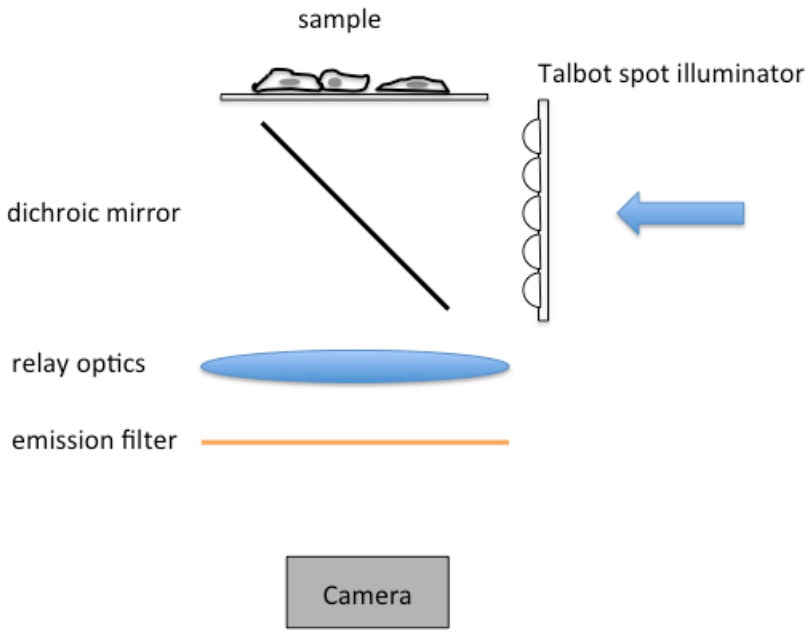

Figure 8.2. Epi-illumination geometry for the fluorescence Talbot microscope.

This setup takes advantage of the long working distance of the FTM. The Talbot illumination will be reflected by the dichroic mirror and projected onto the sample. An optical relay system collects the fluorescence signal from the sample. The required working distance is longer (> 5 mm), in order to maintain the large FOV. The dichoric mirror is based on multilayer interference, and it cannot efficiently reflect high angular frequency illumination. Therefore, the achievable resolution could be lower than the transmission geometry.

System parallelization: The key components of the FTM are all mass producible. The cost of the system is significantly lower than a conventional fluorescence microscope, and the imaging sensor can be used as a consumable component. The FTM system can be made highly compact, and the large FOV could greatly improve the throughput for screening.

The compactness of the FTM simplifies its integration with other systems. In the demostrated longitudinal study of the effect of CPT, FTM was simply placed in an incubator. The total cost of

the system is much less than building a customized incubation environment for a conventional microscope. The compactness of the FTM system also allows system parallelization. One personal computer can connect to multiple FTM devices to further improve the throughput.

8.2 Further applications

The key components of the FTM are all mass producible. The estimate cost of an FTM prototype is around $100 (excluding the laser and the personal computer). Its low-cost and portable properties make the FTM very promising for field diagnosis in low-resource setting [8].

In Chapter 7, we have demonstrated the phenotyping of *C. elegans*. Fast large FOV imaging with high resolution can greatly assist the study of system biology and drug discovery, where high-throughput screening is needed [9, 10]. Compared with the increasing computing power and digital storage capacity, front end microscopic imaging devices have been the bottleneck in screening. Parallelized FTM systems could potentially be the key to change this situation.

The open and simple geometry of the FTM sensor makes it a suitable platform on which sophisticated microfluidic systems can be built. Such integration could engender new compact systems for various high-throughput applications.

We also envision that an FTM-enabled fluorescence ePetri system could be applied in a broad range of research areas. For example, in stem cell differentiation studies, cell tracking is necessary, but long-term imaging can be very tedious [11]. A fluorescence ePetri could significantly reduce the manual labor for such experiments. A fluorescence ePetri assisted with computerized analysis could also be a powerful tool in genome wide RNAi screens [12]. In addition to the large FOV, the time-lapse capability would decrease the phenotype misinterpretation introduced by the time variance of the gene expression [13].

8.3 Conclusion

This chapter is the final chapter concerning the FTM. In this chapter we have explored the possibilities of improving the resolution, imaging speed, various imaging modalities, etc. We also have envisioned the potential biological applications for FTM based on its portability and cost-effectiveness.

REFERENCES

1. D. W. Montgome, "Self-Imaging objects of infinite aperture," *Journal of the Optical Society of America* **57**, 772-778 (1967).
2. E. di Mambro, R. Haidar, N. Guerineau, and J. Primot, "Sharpness limitations in the projection of thin lines by use of the Talbot experiment," *Journal of the Optical Society of America a-Optics Image Science and Vision* **21**, 2276-2282 (2004).
3. M. Born, and E. Wolf, *Principles of optics: electromagnetic theory of propagation, interference and diffraction of light* (Cambridge university press, 1999).
4. B. Hulsken, D. Vossen, and S. Stallinga, "High NA diffractive array illuminators and application in a multi-spot scanning microscope," *Journal of the European Optical Society-Rapid Publications* **7**, 12025, 2026 (2012).
5. J. Wu, X. Cui, G. Zheng, Y. M. Wang, L. M. Lee, and C. Yang, "Wide field-of-view microscope based on holographic focus grid illumination," *Optics Letters* **35**, 2188-2190 (2010).
6. A. Orth, and K. Crozier, "Gigapixel fluorescence microscopy with a water immersion microlens array," *Optics Express* **21**, 2361-2368 (2013).
7. J. G. Wu, G. A. Zheng, Z. Li, and C. H. Yang, "Focal plane tuning in wide-field-of-view microscope with Talbot pattern illumination," *Optics Letters* **36**, 2179-2181 (2011).
8. L. Denny, L. Kuhn, M. De Souza, A. E. Pollack, W. Dupree, and T. C. Wright, "Screen-and-treat approaches for cervical cancer prevention in low-resource settings - a randomized controlled trial," *Journal of the American Medical Association* **294**, 2173-2181 (2005).
9. P. Lang, K. Yeow, A. Nichols, and A. Scheer, "Cellular imaging in drug discovery," *Nature Review Drug Discovery* **5**, 343-356 (2006).
10. R. Pepperkok, and J. Ellenberg, "Innovation - High-throughput fluorescence microscopy for systems biology," *Nature Review Molecular Cell Biology* **7**, 690-696 (2006).
11. T. Schroeder, "Long-term single-cell imaging of mammalian stem cells," *Nature Methods* **8**, S30-S35 (2011).
12. B. Neumann, T. Walter, J. K. Heriche, J. Bulkescher, H. Erfle, C. Conrad, P. Rogers, I. Poser, M. Held, U. Liebel, C. Cetin, F. Sieckmann, G. Pau, R. Kabbe, A. Wunsche, V. Satagopam, M. H. A. Schmitz, C. Chapuis, D. W. Gerlich, R. Schneider, R. Eils, W. Huber, J. M. Peters, A. A. Hyman, R. Durbin, R. Pepperkok, and J. Ellenberg, "Phenotypic profiling of the human genome by time-lapse microscopy reveals cell division genes," *Nature* **464**, 721-727 (2010).
13. B. Neumann, M. Held, U. Liebel, H. Erfle, P. Rogers, R. Pepperkok, and J. Ellenberg, "High-throughput RNAi screening by time-lapse imaging of live human cells," *Nature Methods* **3**, 385-390 (2006).

APPENDIX: TALBOT SELF-IMAGING EFFECT

A.1 Scalar diffraction theory in the angular spectrum framework

Throughout the thesis, the simulations are based on the scalar diffraction theory. The scalar diffraction theory is sufficient, since in the FTM setup, all the dielectric media are linear, isotropic, homogenous, and non-dispersive. The electric and magnetic fields behave identically and their behavior can be fully described by a single scalar wave equation [1].

We now consider the propagation of the electric or magnetic field. Let $u(x, y, 0)$ be the complex field at $z = 0$ plane, This can be treated as the input of the system, and we would like to calculate the output field, $u(x, y, z)$, at a plane that is parallel to the incident plane and a distance z away from it.

The scalar diffraction calculation can be formulated by the theory developed for linear, time invariant (LTI) systems in signal processing.

Suppose a monochromatic wave is incident on a transverse (x, y) plane traveling with a component of propagation in the positive z direction. Across the $z = 0$ plane, the field, $u(x, y, 0)$, has a two-dimensional Fourier transform $U(\alpha, \beta; 0)$, given by

$$U(\alpha,\beta;0)=\int_{-\infty}^{\infty}\int u(x,y,0)\exp\left[-j2\pi(\alpha x+\beta y)\right]dxdy \quad , \tag{A.1}$$

and

$$u(x,y,0)=\int_{-\infty}^{\infty}\int U(\alpha,\beta;0)\exp\left[j2\pi(\alpha x+\beta y)\right]d\alpha d\beta \quad . \tag{A.2}$$

It is obvious that the Fourier transform pair is (x, y) and (α, β). To give the physical meaning of the Fourier decomposition, consider the individual Fourier component

$$\exp\left[j2\pi(\alpha x+\beta y)\right]=\exp\left[jk\left((\alpha\lambda)x+(\beta\lambda)y\right)\right] \quad . \tag{A.3}$$

This can be interpreted as a plane wave whose wavenumber is **k**. The magnitude, k, is $2\pi/\lambda$. The direction cosine of the wave propagation is $(\alpha\lambda, \beta\lambda, \gamma\lambda)$. Figure A.1 shows the direction cosine in the xyz coordinate. The sum of the direction cosine square equals to 1. Therefore.

$$\alpha^2 + \beta^2 + \gamma^2 = 1/\lambda^2 \quad . \tag{A.4}$$

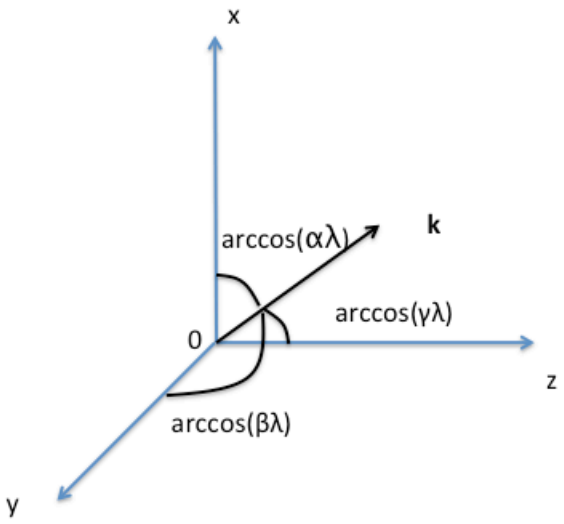

Figure A.1. The wave vector **k** and its direction cosine.

From Equation A.4 we can clearly see that (α, β) represents the spatial frequency of the complex field, and has the same unit as the inverse of the wavelength. For a given wavelength λ, γ is a function of (α, β). $k(\gamma\lambda)$ represents the wavenumber in the propagation direction.

Consider now the spatial frequency spectrum of the field U across the plane parallel to the (x, y) plane and at a distance $z = l$ from it. Let U(α, β; l) represent the spatial frequency spectrum of $u(x, y, l)$. Then

$$U(\alpha,\beta;l) = \int_{-\infty}^{\infty}\int u(x,y,l)\exp\left[-j2\pi(\alpha x + \beta y)\right]dxdy \quad . \tag{A.5}$$

The relation between the angular spectrum at $z = l$, $U(\alpha, \beta; l)$, and that at $z = 0$, $U(\alpha, \beta; 0)$ can be given by

$$U(\alpha,\beta;l) = U(\alpha,\beta;0)\exp\left(j2\pi\gamma l\right)$$
$$= U(\alpha,\beta;0)\exp\left[jk\sqrt{1-(\alpha\lambda)^2-(\beta\lambda)^2}\,l\right]. \quad \text{(A.6)}$$

Equation A.6 can be considered as the phase change introduced by the propagation of an angular spectral component corresponding to (α, β). Here we note that in Equation A.6, $(\alpha\lambda)^2 + (\beta\lambda)^2$ is less than unity, so that the non-propagating term will be not be included. To get the complex field distribution $u(x, y, l)$ at $z = l$ plane, we only need to calculate the inverse Fourier transform of $U(\alpha, \beta; l)$.

$$u(x,y,l) = \int_{-\infty}^{\infty}\int U(\alpha,\beta;l)\exp\left[j2\pi\left(\alpha x+\beta y\right)\right]d\alpha d\beta$$
$$= \int_{-\infty}^{\infty}\int U(\alpha,\beta;0)\exp\left[jk\sqrt{1-(\alpha\lambda)^2-(\beta\lambda)^2}\,l\right]\exp\left[j2\pi\left(\alpha x+\beta y\right)\right]d\alpha d\beta. \quad \text{(A.7)}$$

Figure A.2 depicts this calculation.

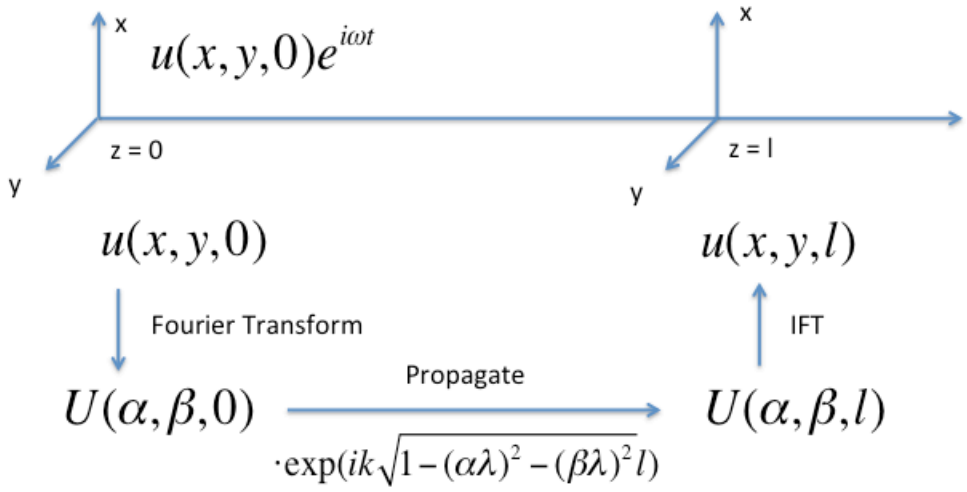

Figure A.2. Illustration of using the angular spectrum in scalar diffraction calculation.

A.2 Fresnel diffraction approximation and the Talbot effect

In the previous section we introduced the method to calculate the complex field distribution along the wave propagation direction. In this section we will apply the angular diffraction theory to explain the Talbot effect of periodic structure of infinite length. For convenience and simplicity, the following discussions are for the one-dimensional case. The deduction for the two-dimensional case can be found in Ref [2].

Let the infinite length of periodic complex field be $u(x, 0)$ at the $z = 0$ plane. Figure A.3 illustrates the Talbot effect for the one-dimensional case.

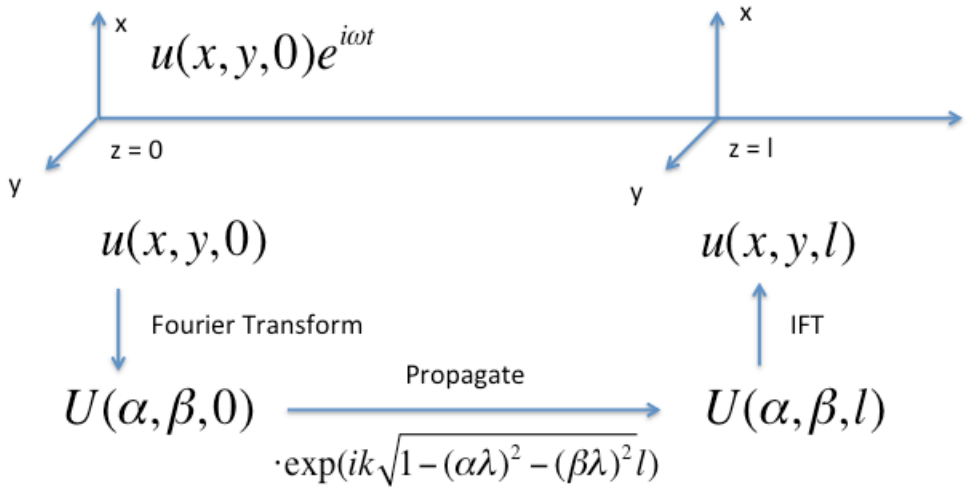

Figure A.3. The Talbot effect of one-dimensional periodic structure

Because the complex field $u(x, 0)$ is periodic, the spatial frequency spectrum $U(\alpha, 0)$ at $z = 0$ plane is discrete. The period of the field is d, so the spatial frequency spectrum is non-zero only at multiples of $1/d$.

In the case of the self imaging effect, the complex field, $u(x, z_T)$, at Talbot distance $z = z_T$ is same as the complex field, $u(x, 0)$, at the $z = 0$ plane. Because the mapping from the spatial domain to the spatial frequency domain is one-to-one, in the frequency domain the complex field $U(x, 0)$ must be equal to $U(x, z_T)$. Equation A.6 relates the complex field at the $z = 0$ plane and complex field at $z =$

z_T together in the spatial frequency domain. The propagation will only affect the phase term, and will not change the magnitude of the spectrum.

For a complex field with a continuous spectrum, it is not possible to have the same complex field after the propagation. However, for the discrete spectrum, as long as the relative phases between the discrete frequency components are the same at the planes $z = 0$ and $z = z_T$, the complex field will be identical.

For the Talbot effect, we need to use the Fresnel approximation in the phase term of the propagation. When the frequency range of the field is much less than $1/\lambda$, the propagation term can be approximated to

$$k\sqrt{1-(\alpha\lambda)^2}\,z_T \approx k\left(1-\frac{(\alpha\lambda)^2}{2}\right)z_T\,, \tag{A.8}$$

With this approximation, the propagation phase is a parabolic function of the spatial frequency spectrum, α. Figure A.4 shows this.

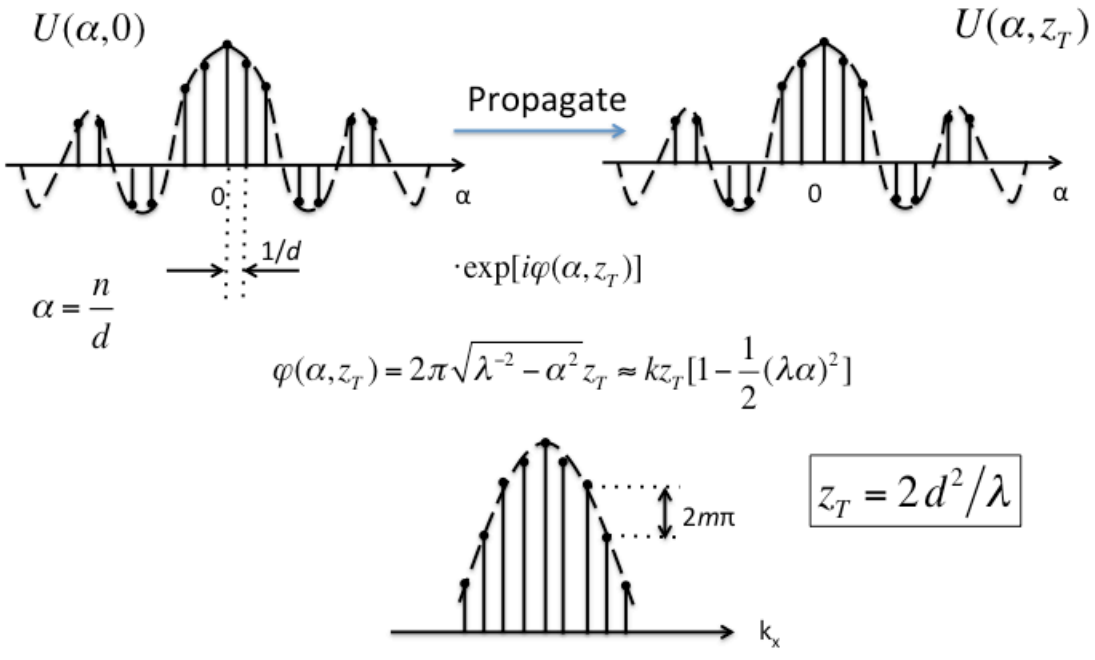

Figure A.4. Fresnel approximation in the Talbot self-imaging theory.

If the phase difference between any spectrum component and the central spectrum component is the multiple of 2π, then the spectrum will be the same as itself at the $z = 0$ plane, and this is the self-imaging effect. To formulate this, we have

$$\frac{2\pi}{\lambda} z_T \left(1 - \frac{(\alpha_n \lambda)^2}{2}\right) \approx 2\pi m(\alpha_n) + \delta \,, \tag{A.9}$$

where α_n is the nth discrete spectrum component, $\alpha_n = n/d$. $m(\alpha_n)$ is an integer, and it is a function of the spatial frequency α_n. δ is the phase of the central spectrum component ($n = 0$). Equation A.9 needs to be valid for all α_n. Let Δ_n be the phase difference between nth spectrum and n-1 spectrum component. Δ_n must be a multiple of 2π.

$$\begin{aligned} \Delta_n &= \frac{2\pi}{\lambda} z_T \left(1 - \frac{(n\lambda)^2}{2d^2}\right) - \frac{2\pi}{\lambda} z_T \left(1 - \frac{((n-1)\lambda)^2}{2d^2}\right) \\ &= 2\pi z_T \left(\frac{(2n-1)\lambda}{2d^2}\right) = 2m\pi \end{aligned} \,, \tag{A.10}$$

where m is an integer. We can see the absolute value of Δ_n is minimum when $n = 0$, and $\Delta_n = (2n\text{-}1)\,\Delta_0$. This implies the minimum z_T that satisfies this condition is

$$\Delta_0 = 2\pi z_T \frac{\lambda}{2d^2} = 2\pi \quad \Rightarrow \quad z_T = \frac{2d^2}{\lambda} \tag{A.11}$$

This is the equation for the Talbot length we first mentioned in Chapter 4.

REFERENCES

1. J. W. Goodman, *Introduction to Fourier optics* (Roberts & Company Publishers, 2005).
2. D. W. Montgome, "Self-imaging objects of infinite aperture," *Journal of the Optical Society of America* 57, 772-778 (1967).